Investigation of the muon-induced secondary electron background in the KATRIN Experiment

Diplomarbeit in Physik

von Henrik Arlinghaus

angefertigt im Institut für Kernphysik

vorgelegt der
Mathematisch-Naturwissenschaftlichen Fakultät
der
Westfälischen Wilhelms-Universität
Münster

Februar 2009

Ich versichere, dass ich die Arbeit selbständig verfasst und keine anderen als die angegebenen Quellen und Hilfsmittel benutzt, sowie Zitate kenntlich gemacht habe.

Ort, Datum Unterschrift

Referent: Prof. Dr. C. Weinheimer
Koreferent: Prof. Dr. J. P. Wessels

CONTENTS

CHAPTER 1

INTRODUCTION

The goal of this thesis was to investigate the origin and distribution of the expected muon-induced electron background in the main spectrometer of the KATRIN Experiment. First, we will give a brief overview of the historical progression of neutrino physics leading up to the KATRIN Experiment, followed by a description of what the KATRIN Experiment is, what its goals are, and its realisation. Finally, an overview of the physics behind the causes of the expected electron background is given.

During the development of the simulations, it became apparent that new experimental data was required in order to accurately model the low-energy muon secondaries; therefore, an experiment was planned and conducted at the electron spectrometer of the former Mainz Neutrino Mass Experiment to resolve these outstanding issues. Unfortunately, the results of these measurements did not agree with measurements done previously to investigate the background in KATRIN. A dedicated

experimental setup was then constructed in Münster to clarify these issues, which ultimately led to results agreeing with our previous measurements in Mainz. The measured angularly dependent secondary electron yield was then used in the simulations of the expected cosmic muon-induced low-energy background of the KATRIN Experiment.

1.1. Neutrinos

The neutrino was originally postulated by W. Pauli on December 4th, 1930[Pau30], when searching for a solution to the beta decay problem: the electrons which were emitted in the beta decay were found to have a continuous energy distribution, and the beta decay violated the conservation of angular momentum. Pauli postulated the emission of a second particle which corrected for the missing angular momentum and carried the remaining energy. In 1934 E. Fermi calculated the mechanics of the three-body beta-decay using the quantum field theory, and named the third particle "neutrino"[Fer34]. The first experimental proof of neutrinos was done by Reines and Cowan[Rei59] in 1956, via an experiment utilizing the inverse beta decay. Because of the extremely small cross-section of this decay, this was only possible by using the intense neutrino flux produced by a nuclear reactor.

Currently, neutrinos have been accepted into the Standard Model of particle physics, which states that neutrinos are massless leptons interacting via the weak interaction. Similar to electrons, there are three generations (often called flavors) of neutrinos, the electron (ν_e), muon (ν_μ), and tau (ν_τ) neutrino.

Measurements such as the Homestake Experiment[Dav94, Dav96] by R. Davis et al. resulted in discrepancies between the solar neutrino flux predicted by the Standard Model and the actually measured flux, with a detected neutrino rate two thirds smaller than expected. While other experiments confirmed the deficite of solar neutrinos, it was not until thirty years afterwards that the results of the SNO (Sudbury Neutrino Observatory) experiment, which was sensitive to the neutrino flavor, were used to explain this phenomenon. The theory of neutrino oscillations, which was originally postulated in 1957, was confirmed: neutrinos oscillate between flavors during their lifetime, resulting in a lower-than-expected count rate of certain flavors and a corresponding excess of others. These oscillations are only possible if each neutrino flavor is a mix of neutrino mass eigenstates, which is only possible for massive neutrinos.

Experiments such as Super-Kamiokande, K2K (KEK to Kamioka), and KamLAND have measured ν-oscillations and determined the corresponding differences of neutrino mass squares between flavors by determining the oscillation length; however, until now no measurement of the absolute neutrino mass has resulted in anything other than an upper limit. Recently, double-β decay experiments have hinted at the neutrino mass; however, these measurements must still be confirmed.

An additional outstanding problem which is directly related to the neutrino masses is the question of the neutrino mass hierarchy, e.g., how the masses of the neutrino flavors are ordered, i.e. whether they follow a quasi-degenerate or a traditional hierarchical scheme.

1.1.1. Measurement of the neutrino mass

The mathematical description of the beta decay by E. Fermi is dependent on the mass of the electron neutrino. Therefore, a precise measurement of the shape of the beta spectrum allows a determination of the neutrino mass.

The decay rate is given by:

$$\frac{d^2N}{dtdE} = R(E)\sqrt{(E_0-E)^2 - m_{\nu_e}^2c^4}\,\Theta\left(E_0 - E - m_{\nu_e}c^2\right) \tag{1.1}$$

with

$$R(E) = \frac{G_F^2}{2\pi^3\hbar^7c^5}\cos^2(\theta_C)\,|M|^2\,F(Z,E)\,p\left(E+m_ec^2\right)(E_0-E)\,. \tag{1.2}$$

Here, E is the kinetic energy of the decay electron, with m_e as the electron mass, p as the momentum of the electron, and E_0 as the endpoint energy (maximum of E) for a zero neutrino mass. $F(Z,E)$ is the Fermi function, and Θ ensures energy conservation. Furthermore, G_F is the Fermi constant, θ_C the Cabibbo angle, and M the nuclear matrix element. Both M as well as $F(Z,E)$ are independent of the neutrino mass; the only dependence lies in the square root term in eqn. 1.1.

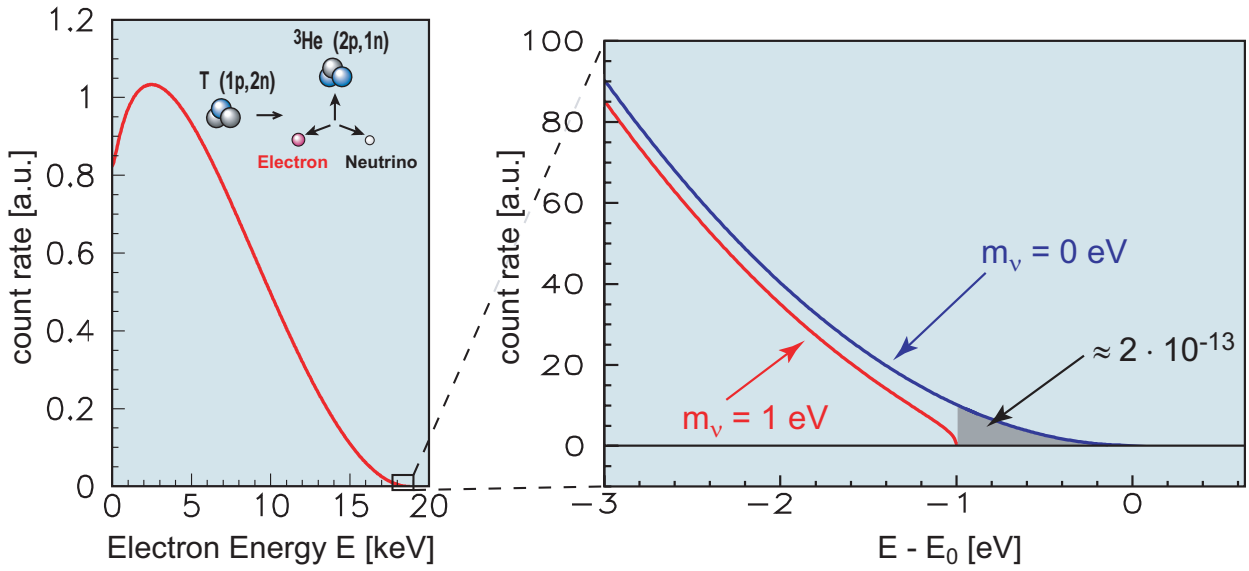

Figure 1.1.: Left: The tritium beta decay spectrum. **Right**: Closeup of the endpoint of the beta spectrum. Two different curves are shown, for neutrinos with a mass of 1 eV and for massless neutrinos, to illustrate the difference.

The dependence of the energy spectrum of the β electrons on the neutrino mass becomes more pronounced close to the endpoint of the spectrum, hence it is desirable to maximize the portion of decays within this endpoint region. Therefore it is ideal to use isotopes with low endpoint energies. The isotopes with the lowest endpoint energies are tritium (^{3}H) and rhenium (^{187}Re). The influence of the neutrino mass in the tritium beta decay is shown in Fig. 1.1.

$$^3H \rightarrow ^3He^+ + e^- + \bar{\nu}_e$$

Tritium has a short half-life of 12.3 y and a simple nuclear and electronic structure allowing the precise calculation of the nuclear matrix elements and molecular effects, as well as allowing the use of gaseous sources, which prevents errors induced by condensed-matter physics effects. Therefore, it is an ideal, often-used candidate for neutrino mass experiments. The latest of these are the Troitz and the Mainz experiments, which set new upper limits on the electron-antineutrino mass of $2.1\,\mathrm{eV/c^2}$[Lob03] and $2.3\,\mathrm{eV/c^2}$[Kra05], respectively. The most important experimental factors affecting the precision of the determined neutrino mass in this type of experiment are the energy resolution affecting the precision of the determinated shape of the beta decay spectrum endpoint, and the count rate in order to measure this in finite time with sufficient statistics. (The halflife of (^{187}Re) is several billion years, which makes usage of this isotope impractical.)

Several alternative methods of measuring the neutrino mass have also been attempted, such as by measuring the neutrinoless double beta decay. Here, the neutrino emitted by a beta decay is absorbed by a second simultaneous beta decay in the same nucleus, resulting in the full decay energy being imparted to the emitted electrons. This would result in a sharp peak at the end of the summed energy spectrum, as the electrons carry the full energy. However, the ββ-decay requires a neutrino as well as an antineutrino: In order for this process to take place, neutrinos would have to be their own antiparticles, i.e. Majorana particles.

Another method which has been attempted by Super-Kamiokande[Lor02] is to measure the duration of a neutrino burst which originated from a supernova event. Neutrinos with different starting energies have differing gamma factors, therefore requiring slightly different amounts of time to arrive; by determining the differences in arrival times and the corresponding energies, the neutrino mass may be determined.

1.2. The KATRIN Experiment

The KATRIN (KArlsruhe TRItium Neutrino) Experiment is an experiment which will measure the neutrino mass with a sensitivity of $0.2\,\mathrm{eV/c^2}$ (90% CL) or, failing this, determine a new upper limit for the mass. The neutrino mass is derived from a measurement of the endpoint region of the tritium decay spectrum. Following similar experiments such as the Mainz Neutrino Mass Experiment[Kra05] and Troitz[Lob03] with a sensitivity of $2\,\mathrm{eV/c^2}$. Thus KATRIN aims for an order of magnitude improvement to the sensitivity of the neutrnino mass compared to the Mainz and Troitz experiments.

The total length of the experimental setup is 70m, with gaseous tritium entering the setup at the source end, and the decay electrons being magnetically guided through the various sections until they reach the detector. An overview of the experimental setup is shown in Fig. 1.2. The experiment itself is being set up at the Forschungszentrum Karlsruhe (FZK), making use of the existing tritium know-how and the infrastructure at the largest civilian tritium laboratory in the world, the Tritiumlabor Karlsruhe (TLK). The major components of the setup fall into two groups, those inside the TLK with the corresponding tritium containment requirements such as double-walled vacuum sections, x-rayed welds, etc., and those which are located outside this hall, namely both

spectrometers and the detector system. A short description these components follows; for details see the Katrin Design Report 2004 [Ang04].

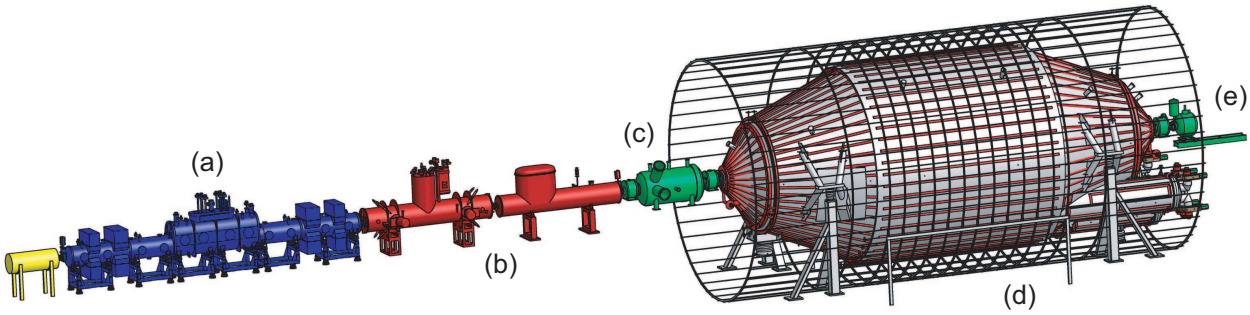

Figure 1.2.: Overview of the KATRIN Experiment. (a) The WGTS section, within which T_2 decays, emitting neutrinos which escape from the experiment, and electrons which are magnetically guided to (b), the transport section. This section consists of the differential and cryo-cooling sections, which work together to remove the remaining undecayed tritium gas from the experiment. The electrons continue on to (c), the prespectrometer, where an initial energy filtering is done, and then on to (d), the main spectrometer, with the final filtering. Electrons not removed by the MAC-E filters are then detected by the detector (e).

1.2.1. Source

The secondary electrons originate in the windowless gaseous tritium source (WGTS) section, within which the tritium decays occur. Here, tritium gas with a central pressure of $3.4 \cdot 10^{-3}$ mbar enters the vacuum at the center of a 10-m-long tube, and subsequently drifts towards both ends resulting in a column density of $\rho d = 5 \cdot 10^{17}$ molecules$/\mathrm{cm}^2$. As the name implies, this is a windowless source: While most of the tritium gas is removed from the vacuum by turbopumps at each end of the section, some will continue to diffuse through the beamline, as there are no windows preventing the gas from exiting this section. Utilizing a gaseous source removes the uncertainties involved in the condensed-matter physics involved in a solid source, such as the one used in the Mainz experiment. The tritium temperature (27K) and pressure in this column must remain constant, as fluctuations here would smear the decay spectrum reducing the total mass sensitivity; achieving the required stability level in a tritium-certified system requires surmounting incredible technical difficulties. The source section itself contains superconducting magnets creating a 3.6T field along the beam axis, which guide the isotropically emitted decay electrons along the pipe, either towards the detector or to the monitoring section in place at the back end of the source; a maximum angle of 50.77° is accepted. Additionally, the entire source section is on a constant electrical potential, thereby ensuring a uniform acceleration of decay electrons, no matter where in the section the decay took place. The removed tritium and helium gas is then recycled and purified by additional hardware located in the TLK section of KATRIN (this hardware is not shown in Fig. 1.2).

1.2.2. Transport section

A further reduction of tritium pressure is mandatory in order to prevent decays from taking place outside the source, which would contaminate the spectra with incorrect energies. The next section is an additional pumping section consisting of two parts; its purpose is to remove any remaining tritium gas from the vacuum. First, in the additional differential pumping section (DPS2), turbopumps are used to reduce the tritium flux to $0.4 \cdot 10^{-7}\,\mathrm{mbar}\cdot\mathrm{l/s}$. Here the beampipe is zigzagged in order to increase the likelihood that the neutral tritium atoms will collide with the walls and are deflected towards the turbopumps. In the second part of the transport section, the cryo-pumping section (CPS), an argon frost coating is applied to the walls of the beamtube via liquid-helium cooling, trapping any remaining tritium. This results in a residual tritium flux of at most $10^{-14}\,\mathrm{mbar}\cdot\mathrm{l/s}$ and a tritium density of $10^{-20}\,\mathrm{mbar}$ in the spectrometer sections. Again, superconducting magnets are used to guide the decay electrons through this section.

1.2.3. Spectrometers

The electrons then enter the two spectrometers, both operating via the MAC-E Filter principle, explained in subsection 1.2.6. The prespectrometer with a length of 3.5 m and diameter of 1.7 m is operated at $100-200\,\mathrm{V}$ below the tritium endpoint energy, resulting in a reduction of the incoming electron rate from 10^{10} electrons per second to 10^{3} electrons, with an energy resolution of 75 eV, thus removing all electrons which are significantly below the tritium endpoint energy. MAC-E type spectrometers are integrating spectrometers allowing all electrons above a given minimal energy to pass. Scanning the cut-off energy enables the generation of integral electron fluxes, from which the tritium spectrum is derived. In addition, the magnetic field strength is increased, thus limiting the accepted angles of the decay electrons via magnetic reflection of large angles, ensuring that the likelihood of inelastic collisions remains low.

The main spectrometer, shown in Fig. 1.3, with a diameter of 10 m, a length of 23 m, and weighing over 200 t, then reduces the electron rate further, down to a few mHz[1] in the vicinity of the tritium endpoint. Due to this low count rate, the electron background must be kept below 10 mHz to remain within the acceptable statistical error. The spectrometer has a surface area of $630\,\mathrm{m}^2$; assuming a cosmic muon background rate of $189\,/\mathrm{m}^2\mathrm{s}$[Bog06], this results in a muon intersection rate to the order of 10^5 muons per second. A shielding electrode is being constructed which will reduce the electron background originating from these muons in the spectrometer vessel, as well as from radioactive decays in the 200 tons of stainless steel. This shielding electrode is in the form of wire electrodes (see next subsection). This results in a very lightweight construction with very little mass, and whose background contribution is minimal.

1.2.4. Wire Electrode

In order to reduce the background, a double-layered wire electrode was designed[Val09] and is being constructed in Münster[Hil10] which will raise the inner tank potential by 200 V in two

[1] The exact rate is strongly dependent on the retarding voltage.

Figure 1.3.: Photo of the KATRIN main spectrometer during transport to FZK.

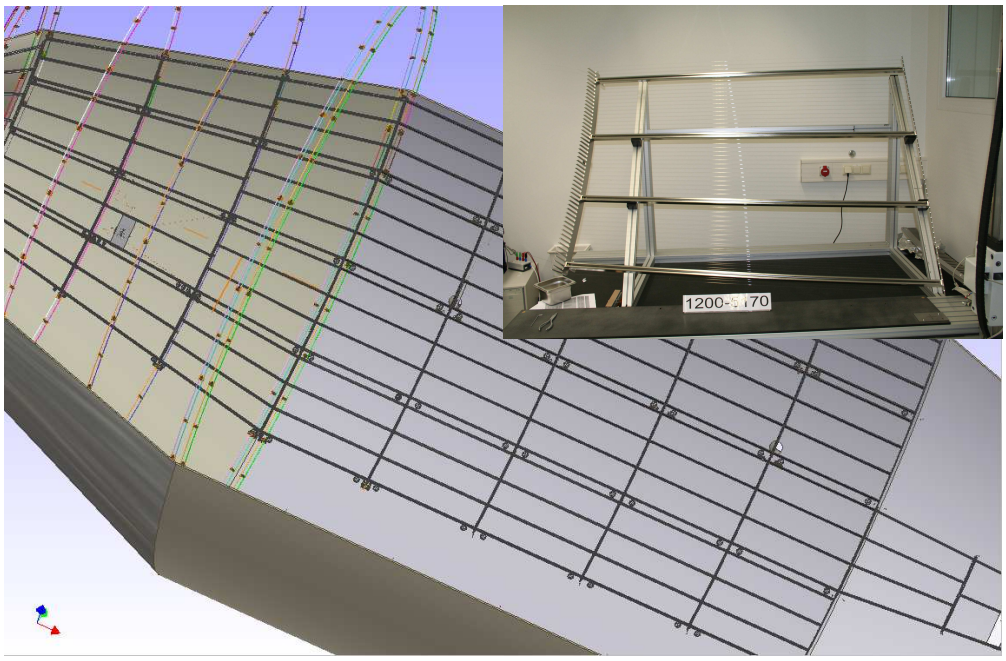

Figure 1.4.: Inset: A completed module on the QA measurement table in the Münster cleanroom. **Full image**: Such modules are tiled inside the main spectrometer, so as to fully cover the surface.

100 V steps, allowing only background electrons with a minimal perpendicular energy of at least 200 eV to enter the flux tube and reach the detector. This electrode consists of three major parts: a rail system mounted to the inside of the spectrometer as a mounting base, wire electrode modules

mounted upon this, and full-metal shielding and grounding electrodes close to each end of the spectrometer, the small conus areas (details of the electromagnetic design process are available in [Val09]). The modules themselves consist of two "combs", bolted together via C profiles, holding the wires. A total of 240 modules is required, which are constructed from 480 combs and ≈22000 wires, with a constant wire layer offset of 70mm. In order to minimize the background contribution of the wires, several stainless steel wires were tested for radioactivity before choosing the manufacturer (see [Geb07, Ben09]). In order to cover the gaps between modules, thin endcaps are currently being designed for the central modules which will cover the teeth of two adjacent combs, smoothing the electric potential in the spectrometer. Figure 1.2.4 shows both a completed module in the cleanroom, and the placement of the modules in the main spectrometer.

1.2.5. Detector

Only electrons with an energy above the main spectrometer's retarding voltage arrive at the detector. As they are leaving the spectrometer with its potential of $\approx -18.6\,\mathrm{kV}$, they are reaccelerated, which allows them to deposit enough energy to be detectable. The detector itself is a circular silicon PIN diode detector, with a radius of 4.5cm which is divided into 148 segments. This pixilation allows the rejection of events in noisy segments as well as of events in segments shown to be unreliable by calibration with an electron gun. It also allows for corrections depending on the local transmission function of each pixel. The detector will be surrounded by massive shielding consisting of alternating layers of lead and copper, as well as an active muon veto, in order to reduce the background.

1.2.6. MAC-E Filter

Both the aforementioned spectrometers operate via the MAC-E (*M*agnetic *A*diabatic *C*ollimination combined with an *E*lectrostatic Filter) Filter principle[Bea80, Pi92a, Lob85]. In such a filter, a strong magnetic field is generated both at the entrance and exit of the spectrometer, resulting in a minimal extent of the flux tube in the central magnet planes, as well as a magnetic field minimum in the center of the spectrometer, as shown in Fig. 1.5. The resulting gradient of the magnetic field strength results in an adiabatical transformation of the cyclotron energy of the electrons to longitudal energy, with a minimum of the cyclotron energy in the central plane of the filter. At the same time, the interior of the entire vessel has a uniform electrical field, with the result that the electrons which enter the spectrometer have to surmount an electrical field gradient, thereby decreasing their longitudinal energy. In the central plane of an ideal MAC-E-Filter, the entire electron's energy is longitudinal, resulting in a sharp cutoff on the electrons' initial energy, independent of the starting angle. However, in an actual MAC-E-Filter, the magnetic field strength is not infinitesimally small in this plane. Therefore, the electrons have residual cyclotron energy which is dependent on the ratio of the central magnetic field to the outer field as follows:

$$\frac{\Delta E}{E} = \frac{B_{\mathrm{min}}}{B_{\mathrm{max}}} \tag{1.3}$$

This defines the transmission width of the filter. In the case of the main spectrometer, a resolution of $0.93\,\mathrm{eV}$ is achieved.

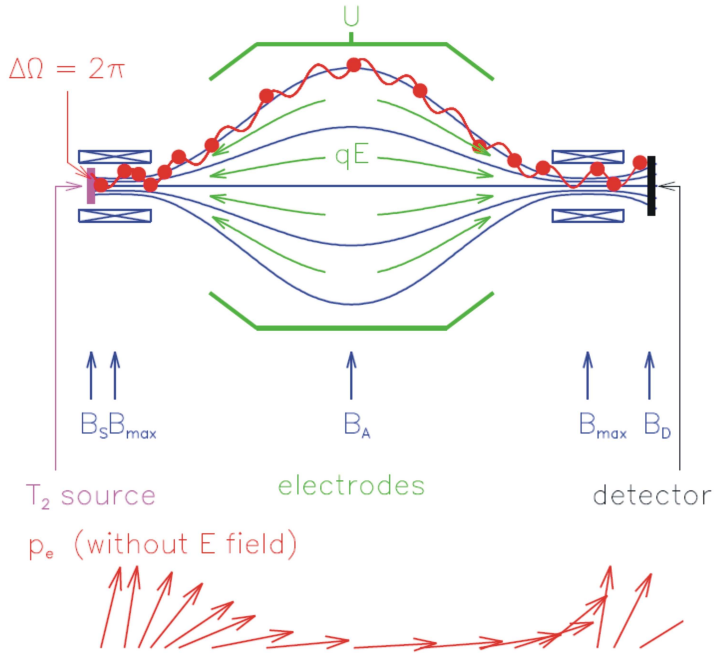

Figure 1.5.: Schematic of the MAC-E filter principle. The path taken by a decay electron is shown, along with the corresponding change in radial energy.

1.2.7. Maximum allowable errors

The allowed systematical and statistical errors in the KATRIN Experiment are $\Delta^2_{\text{stat}} = 0.018\,\text{eV}^2/\text{c}^4$ and $\Delta^2_{\text{sys}} = 0.017\,\text{eV}^2/\text{c}^4$, respectively[Ang04]. This includes the error induced by the electron background since the use of an incorrect factor when correcting for the background electron count rate falsifies the actual count rate and thereby falsifies the resulting neutrino mass. Therefore, a limit on the background count rate of $\Gamma = 10\,\text{mHz}$ for energies near the endpoint energy was defined as the maximum acceptable rate.

1.3. Backgrounds

There are two primary sources of background in this kind of low count rate experiment. These are radioactive decays in the materials comprising the experiment and its surroundings, and interactions between cosmic rays and the experiment (see section 1.4). While careful selection of the materials comprising the experiment and its surroundings as well as the usage of shielding can reduce the impact and count rate of radioactive decays, this can quickly become exceedingly costly and greatly increases the time required to set up the experiment. Cosmic rays, the other source of background, cannot be efficiently shielded against. Low count rate experiments, such as dark matter search experiments, are performned inside deep underground laboratories, which reduces the cosmic ray flux, still without fully eliminating it, and also leads to a new source of background,

namely decays in the rock used as shielding. This option is not available to all experiments, again due to cost, logistical requirements, and experiment size.

1.3.1. Backgrounds in the KATRIN Experiment

In the KATRIN Experiment, both sources of background are present and must be understood and reduced. The previously mentioned wire electrode, the concept of which has been sucessfully tested in the Mainz Neutrino Mass Experiment[Thü02], serves as the primary means of reducing background originating from the walls of the spectrometer induced both by radioactive decay and cosmic rays. Additional background reduction methods to reduce the detection probability of primary background particles are in place around the detector. Thus, the principle sources of background consists in electrons originating in the walls of the spectrometers, which still may pass through the wire electrode in small quantities, depending on the local magnetic field strength and the background electron's energy, as well as those electrons produced during the ionization of the remaining air molecules (at $p \propto 10^{-11}$ mbar).

1.3.2. Effects of background electrons in the spectrometer

Electrons ejected from the walls of the spectrometer are accelerated towards the entrance/exit of the spectrometer due to the electric potential, and guided by the magnetic fields. Depending on their starting location and energy, these electrons either enter the central flux tube, subsequently reaching the detector and causing background events with energies similar to the tritium endpoint, or they enter the prespectrometer, or are trapped in a penning trap (see [Zac09, Hug08] for a detailed description of the penning traps in the main spectrometer). Secondaries with significantly higher energies are easily rejected in the detector due to the larger energy deposition; however, these may strike other components ejecting further secondaries. A large number of trapped electrons can lead to damaging discharges, or falsification of the energy of electrons originating in a tritium beta decay.

1.3.3. Background electrons induced by cosmic rays

One source of secondary electrons is cosmic muons (see section 1.4) passing through the spectrometer vessel twice. These may also intersect the grounding electrode or components of the wire electrode. As muons are minimally ionizing particles, they continuously create secondary electrons in their wake when passing through matter. Depending on their interaction location in the material, their energy, and the density of the material, these secondaries may reach the surface and enter the vacuum. A portion of these may ultimately reach the detector. Therefore, simulations were designed to calculate the muon rate passing through the spectrometer surfaces, as well as the number of secondary electrons ejected.

1.3.4. Background electrons induced by radioactive decay

Another source of electrons is radioactivity caused by decays of atoms in the material of the spectrometer itself, as well as by decays in the hall containing the spectrometers. Stainless steel contains several long-lived radioactive isotopes, the most predominant of which are ^{60}Co, ^{137}Cs, and ^{40}K. As these predominately decay by beta radiation, electrons are produced which may enter the vacuum. In addition, the interaction of gammas produced by the thorium and uranium decay chains present in the concrete of the building via the compton and photo effect with the electrons present in the spectrometer walls leads to further background electrons.

1.4. Cosmic rays

Space is filled with many high-energetic charged particles of solar, galactic, or even intergalactic origin. These particles are primarily protons, comprising 79% of the primary spectrum, with helium comprising 14.7%, while heavier nuclei's percentages are mostly ordered by mass[Yao06]. Antiprotons are also present; however, they are $2 \cdot 10^{-4}$ times less abundant than protons. The lower-energy portion of the incoming cosmic ray flux varies with the location on earth, due to its dependence upon the local geomagnetic field strength, as well as with the solar wind strength, which is dependent on the current solar activity. The energy spectrum of primary cosmic rays is shown in Fig. 1.6, the spectrum is initially proportional to $e^{-2.7}$, with two steps visible, nicknamed "the knee", at roughly $5 \cdot 10^{15}$ eV and "the ankle", at $\approx 5 \cdot 10^{18}$ eV. While cosmic rays with lower energies arrive isotropically, experiments such as the Pierre-Auger Observatory in Chile attempt to measure the origin distribution of ultrarelativistic cosmic rays, and initial results show strong indications for a nonisotropic source distribution at the highest energies.

1.4.1. Air Showers

These cosmic rays collide with atomic nuclei in the upper atmosphere, leading to a shower of secondary particles due to the ultrarelativistic energies of the incident particles. The resulting particles also continue interacting with the atmosphere, resulting in a long chain of collisions. The high energies of the primaries result in cone-shaped shower profiles with a hadronic core, as well as a large number of electromagnetic subshowers with a larger opening angle. Most of the created secondaries are electrons and photons, with the muonic count being an order of magnitude smaller. While the half-life of muons and pions is of the order of μs, they are traveling with relativistic speeds which allows them to penetrate deeply into the atmosphere, e.g. muons have a typical decay length of 15 km. Figure 1.6 shows a small air shower.

1.4.2. Cosmic rays at sea level

The distribution of shower secondaries at ground level is listed in table 1.1, taken from [Bog06]. The electrons and gammas can be blocked by ≈ 15 cm of lead shielding. The muons, however, penetrate such shielding with a negligible energy loss.

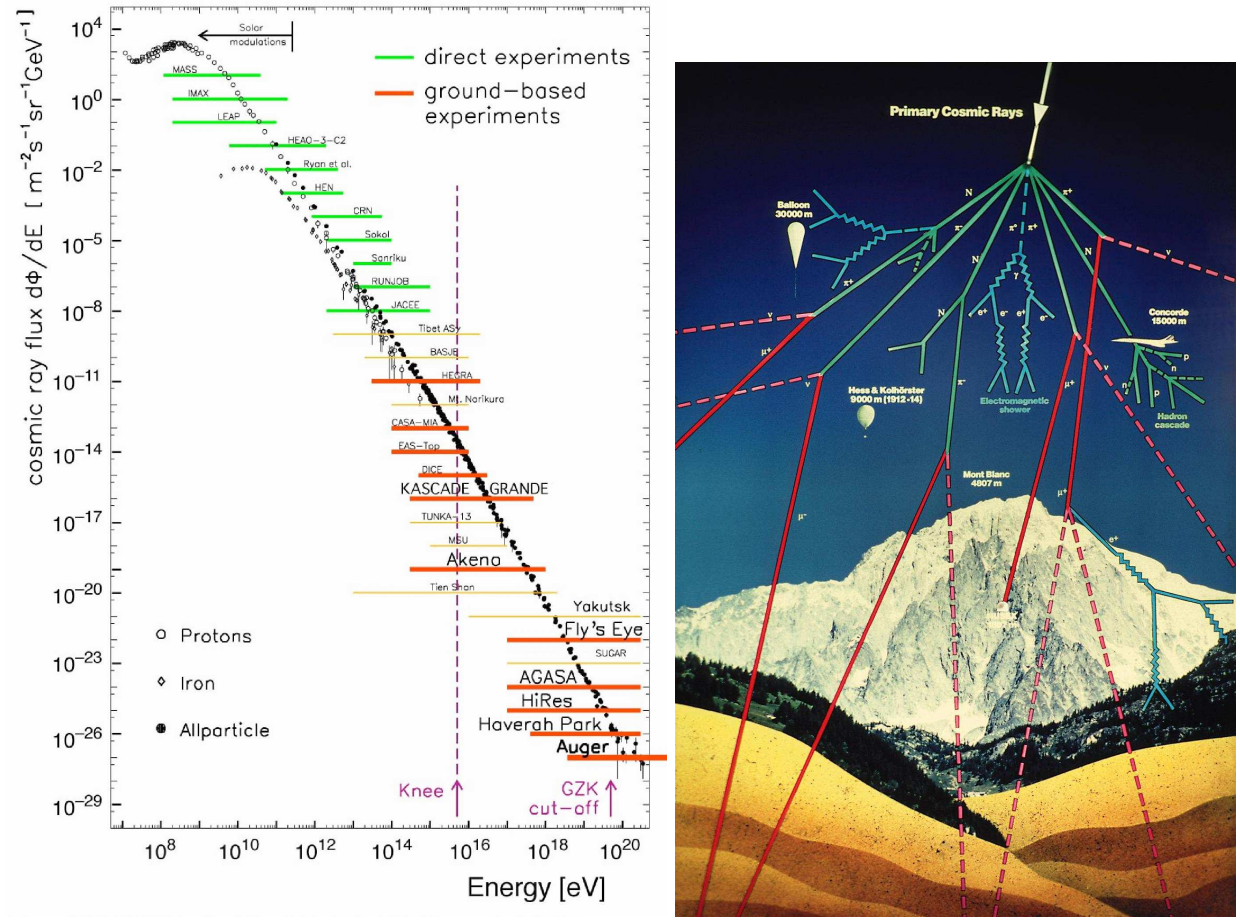

Figure 1.6.: Left: Cosmic ray energy spectrum, along with the upper detection limits of various experiments which are investigating these. Image taken from [Eng06]. **Right**: An example of the interactions present in air showers. (Image by CERN)

While the angular distribution of the incoming cosmic rays is isotropic when hitting the upper atmosphere, the distance between the starting point of a shower and the surface varies greatly depending on their relativ incident angle to the surface normal of the atmosphere, due to the curvature of the earth. Because of the previously mentioned decay length, fewer particles from showers with shallow incident angles reach the surface, when compared to showers with a steep zenith angle, which have the highest percentage of secondaries reaching the surface. A $\cos^2$ angular dependence can be used to describe the atmospheric depth for muons with steep zenith angles; however, for larger angles, more detailed distributions must be used, which correct for the curvature of the atmosphere (see subsection 1.4.3).

Water as well as rock may be used to shield against incoming muons; however, these are needed in large amounts. Therefore, low count rate experiments which require a very low background such as neutrino experiments or dark matter experiments such as SNO, the XENON Dark Matter Search Experiment, and OPERA are conducted in underground laboratories where hundreds or thousands of meters of rock will reduce the muon flux (shielding value typically given as m.w.e. (meters water equivalent)); IceCube[Gol01] follows an alternative method of shielding as it is conducted

Total flux	Muons	Secondary neutrons	Electrons	Protons, pions
$3 \cdot 10^{-2}\,\mathrm{cm}^{-2}\mathrm{s}^{-1}$	63%	21%	15%	$< 1\%$

Table 1.1.: Sea-level cosmic ray flux components

under $\approx 1.5\,\mathrm{km}$ of ice.

1.4.3. Angular dependence of cosmic rays at ground level

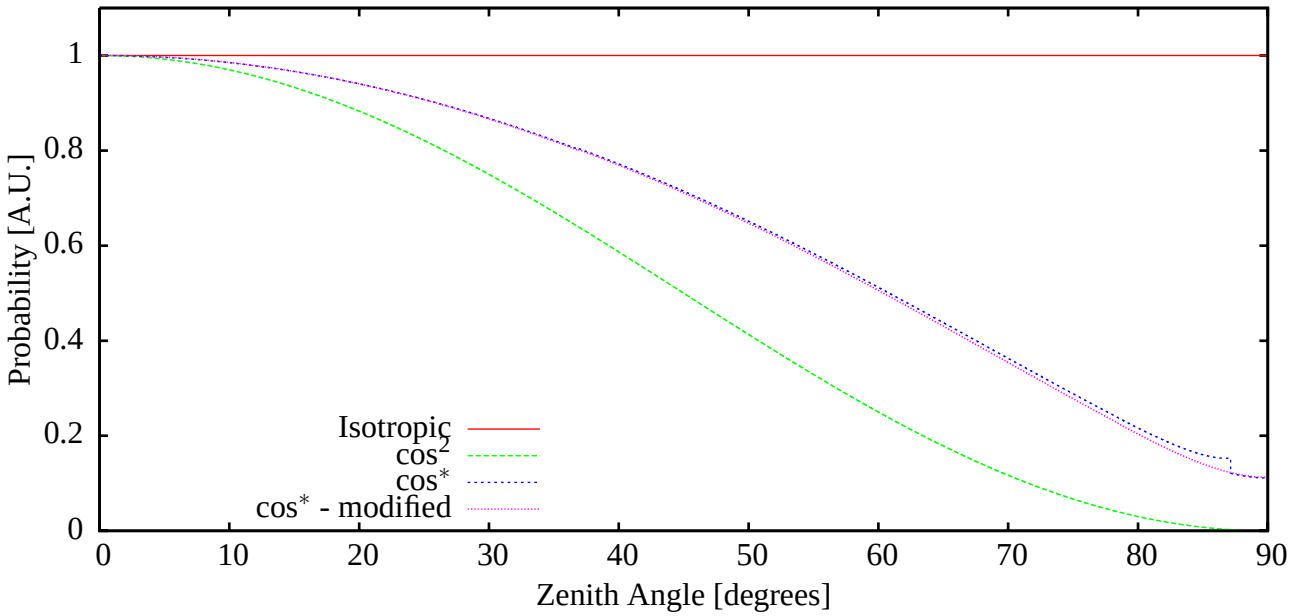

Figure 1.7.: The two most common approximations of the cosmic muon angular spectra, as well as the $\cos^*$ distribution. The discontinuity in the origial $\cos^*$ function is clearly visible near 85°. The corrected function is also shown, with the discontinuity removed. The finite probability for large-angle incident muons is visible. This probability accounts for the curvature of the earth's atmosphere, unlike the $\cos^2$ distribution which approaches zero for shallow incident angles. Muons with an angle above 90° are very unlikely due to shielding by the earth itself and therefore are ignored.

A precise description of the angular cosmic muon spectrum was required for the simulations (see sections 2.3 and 5.1.2), an approximation proposed by S. I. Klimushin et al.[Kli00] was used which contains correctional factors for large zenith angles. A short description of this $\cos^*$ distribution follows:

$$\cos^* \theta = S(\theta) \cdot \cos^{**} \theta \tag{1.4}$$

with

$$S(\theta) = 0.986 + 0.014 \cdot \sec\theta \tag{1.5}$$

being used for $\sec\theta <= 20$

$\cos^{**}\theta$ is a polynomial fit of the form

$$\sum_{i=0}^{4} c_i \cdot \cos^i \theta \tag{1.6}$$

with the coefficients depending on the value of $\cos\theta$, listed in table 1.2.

$\cos\theta$	c_0	c_1	c_2	c_3	c_4	Max error [%]
0 - 0.002	0.11137	0	0	0	0	0.004
0.002 - 0.2	0.11148	-0.03427	5.2053	-14.197	16.138	0.3
0.2 - 0.8	0.06714	0.71578	0.42377	-0.19634	-0.021145	0.7

Table 1.2.: Coefficients for the $\cos^*$ muon incident distribution. The error refers to the discrepancy between this solution and an analytical solution also defined in [Kli00].

The angular distribution shown in Fig. 1.7 exhibits a discontinuity which was presumably caused by an incorrect factor in equation 1.4. This was corrected:

$$S(\theta) = 0.986 + 0.05 \cdot 0.014 \cdot sec\theta \tag{1.7}$$

The resulting distribution is also shown in Fig. 1.7.

1.5. Monte Carlo Methods

Not all physical problems can be solved analytically or numerically. Monte Carlo methods may be utilized to approximate solutions to complex problems; these use random-number generators which reflect the probability of different effects occurring, and arrive at a result via the summation of many initial random events.

Originally named “Monte-Carlo“ by Los Alamos National Laboratory physicists during the 1940s, with the advent of powerful computing resources these methods have proven useful in many branches of physics. An example of this is the Geant4 toolkit[Ago03, All06] developed by a CERN-based collaboration for use in particle physics applications.

1.5.1. Example: Monte Carlo Calculation

As an example, we will show how to create an isotropic point distribution in a cylinder with an inner radius of R_i and an outer radius of R_o, e.g. radioactive decays in the volume of a cylinder oriented along the Z axis, via two alternative approaches.

The simpler method is the Von Neumann method. Here, random points are generated in a box enclosing the cylinder, and then a test is conducted to check whether the point is within the cylinder. While this approach “wastes“ some computation time in the check and possible subsequent regeneration, for solid cylinders (with $R_\mathrm{i} = 0$) which fill 78.5% of the box volume the relatively simple

required by the V.N. method may result in this being the faster implementation[2] (with random numbers r_0, r_1, and $r_2 \in [0..1[$).

$$X = -R_o + r_0 \cdot (2 \cdot R_o) \tag{1.8}$$
$$Y = -R_o + r_1 \cdot (2 \cdot R_o) \tag{1.9}$$
$$Z = r_2 \cdot (Z_{max} - Z_{min}) + Z_{min} \tag{1.10}$$

The first two steps must be repeated until the condition $X^2 + Y^2 \leq R_o^2$ is fulfilled.

However, once we begin searching for decays in hollow cylinders, such as a cylinder with a wall thickness of 2 cm and a diameter of 10 m, a very large number of points must be generated in order to find an acceptable one, with the additional condition: $X^2 + Y^2 \geq R_i^2$

Here the second approach becomes more practical. By calculating the probability density function (PDF) of a cylinder with inner radius R_i and outer radius R_o and inverting this function, we arrive at a distribution function which then is used to generate events which are evenly distributed throughout the volume (with random numbers r_0, r_1 and $r_2 \in [0..1[$).

$$\alpha = r_0 \cdot 2\pi \tag{1.11}$$
$$R = R_{max} \cdot \sqrt{\left(\frac{R_{min}}{R_{max}}\right)^2 + r_1 \cdot \left(1 - \left(\frac{R_{min}}{R_{max}}\right)^2\right)} \tag{1.12}$$
$$X = sin(\alpha) \cdot R \tag{1.13}$$
$$Y = cos(\alpha) \cdot R \tag{1.14}$$
$$Z = r_2 \cdot (Z_{max} - Z_{min}) + Z_{min} \tag{1.15}$$

Here, every randomly generated point is automatically inside the volume and therefore requires no further testing, which results in this more complex code only having to be executed one time.

These methods may also be combined by approximating the PDF and using this to generate values for the V.N. method. Using these methods for more advanced probabilities, such as those required to describe the angular and energetic distribution of cosmic muons, one can create simulations which accurately[3] recreate physical phenomena.

1.6. Electromagnetic simulation tools

Several programs were used to calculate the electric charge densities of different geometries. These were developed by F. Glück. (Forschungszentrum Karlsruhe) (See [Glü05a, Glü06a, Glü09a]) and maintained by S. Vöcking (Universität Münster, see [Vöc07]). These programs are:

[2] This depends on the CPU architecture, and the complexity of the utilized random number generator.
[3] Assuming accurate input models and sufficiently large statistics

- **Magfield2**: Magfield2 calculates the magnetic fields of a given set of magnetic coils, with fixed dimensions and currents, allowing the calculation of the field strength at any point, with Legendre polynomials used for most points to simplify the calculations. These coils must be orientated along a single axis.
- **Magfield3**: This is an updated version of Magfield2 allowing tilted coils as well, and coils which are not centered on the axis.
- **ELCD3.2**: This determines the electric potentials of conic electrodes, allowing the determination of the electrostatic fields of rotationally symmetrical geometries. The entire geometry may be mirrored.
- **ELCD3.3**: This determines the electric potentials of a nonaxially symmetric geometry. Unlike in ELCD3.2, here the geometry is described by a multitude of rectangular electrodes and solid cylindrical electrodes.
- **Eltraj**: This program tracks particles through a given geometry, using both Magfield and ELCD routines for the determination of the trajectory.

Both ELCD3.2 and ELCD3.3 store the generated fieldmap or coefficients in a datafile. The generation of this file is very CPU- and memory-intensive, with memory usage rising with the second power and CPU time with the third power of the number of elements. Therefore, a balance was struck between the detail of the geometries and the CPU time needed to determine the Coulomb matrix. In addition, when determining the field strength near the surface of an electrode, elliptical integrals are used, which are CPU-intensive as well. Further details of these programs and of the geometric approximations undertaken during the design of the electrode system due to the memory limitations may be found in [Val09, Hug08].

1.7. Thesis overview

This thesis is structured as follows:

The second chapter contains a brief introduction to Geant4, a particle physics simulation framework, via the use of an simple simulation as an example; then a description of the simulation of the KATRIN main spectrometer follows, as well as the results of the simulations conducted with this software.

The third chapter describes tools used to analyze both the data resulting from these simulations, as well as the data recorded by a new DAQ system used in several experiments conducted both in Münster as well as in Mainz. In the process, a short overview is given of modern methods of analyzing signals by describing the algorithms utilized for the analysis of the data taken during measurements in Mainz.

The next chapter explains the design and construction of a high-voltage vacuum chamber which was used to measure the emission rate of secondary electrons ejected from stainless steel by cosmic muons.

The fifth chapter then describes the analysis of the recorded data and presents the results of these measurements.

Finally, we review the results of this thesis and give an outlook on possible future topics of investigation which would refine these results.

CHAPTER 2

GEANT4

Geant4 (GEometry ANd Tracking)[Ago03, All06] is a Monte Carlo (MC)-simulation framework developed by a CERN-led collaboration of particle physicists for the simulation of the passage of particles through matter, with a full description of possible physical interactions. First proposed in 1994, the initial aim of the Geant4 project was to enable the simulation of the then planned next generation detectors, and cumulated in an initial release in December 1998. The toolkit is now being used for many different applications in particle, nuclear, and accelerator physics, from experiments with very high energy scales such as TeV colliders down to low-energy processes on the order of a few hundred or thousand eV. This toolkit can be included in user-developed programs, and the provided physics, tracking, geometry, and other modules can be utilized and modified; or, if required, additional modules can be written. Previous versions up to Geant3 were

written in Fortran, however, starting with Geant4 the framework was completely rewritten in C++, with support for the inclusion of Fortran code.

The Geant4 framework was used to develop the SIKatrin simulation, a full-fledged background simulation program for KATRIN's main spectrometer, allowing the simulation of background electrons produced by radioactive decays or by cosmic muons in the main spectrometer vessel, subsequently tracking these, and the determination of the electrons' spacial distributions during any phase of their existence as well as their energy distributions.

In the following section, the basics of this framework will be described, using a small simulation which was written to determine a detector's acceptance factor.

2.1. Simulation of ^{83m}Krypton in an enclosed volume

During the course of verification measurements using an ^{83}Rb source at Münster by M. Zboril[Zbo10] and M. Rasulbaev[Ras10], a small experiment was set up in order to determine the count rate of the conversion electrons produced during the decay of ^{83m}Kr, a short lived ($t/2 = 1.83\,\mathrm{h}$) decay product of ^{83}Rb, in a vacuum system. To accomplish this the rubidium source was attached to a small CF40[1] vacuum setup, containing a silicon pin diode. While the count rate could be measured and the branching ratios of krypton were known, the solid angle was not known; in order to determine this a small Geant4 simulation was written. It was assumed that the krypton gas was distributed homogeneously in the volume.

2.1.1. Geometry

One of the most important aspects of this simulation was a simple yet accurate representation of the experimental geometry. The experiment itself consisted of a four-fold CF40 cross-piece with two closed sides, where one was closed by the valve and a second by a blind flange, the detector was attached to the third side, and the last opening was connected to the capillary of the source (see Fig. 2.1 to view the resulting geometry). The detector was a silicon PIN diode attached to a BNC feedthrough flange. The legs of the diode were not included in the simulation as they were directly soldered to the feedthrough and would not affect the total volume significantly.

However, before the geometry which was used in the simulation could be created, the materials of these components must be defined. In Geant4, one can define various elements, isotopes, and compound materials consisting of these elements. Stainless steel was used for the vacuum components, and silicon and polystyrene for the detector (See listing 2.1 for the implementation). Additionally, a material must be defined for the vacuum contained within the setup, with the appropriate density.

Listing 2.1: Creating stainless steel as a Geant4 material, using component elements.

```
1        //      Create the elements
2 [...]
3        a = 14.01*g/mole;
4        G4Element* elN  =       new G4Element("Nitrogen", "N",  z=7.,  a);
```

[1] CF40 is equivalent to CF35 and refers to the vacuum components having an inner diameter of 35mm

```
5         a = 16.00*g/mole;
6         G4Element* elO  =       new G4Element("Oxygen",   "O",  z=8.,  a);
7
8         //      Create the material
9         density = 1.29e-03*g/cm3;
10        G4Material* Air = new G4Material("Air", density, nel=2);
11        Air->AddElement(elN, .7);
12        Air->AddElement(elO, .3);
13
14        //      Density is air at 1 bar. devide by 10^(n+3) for pressure in millibar.
15        G4Material* Vac =       new G4Material("Vacuum", z= 1., a= 1*g/mole, density / 100000000.);     //      10^-5 millibar
16
17        density = 1.032*g/cm3;
18        G4Material* Polystyrene = new G4Material(name="Polystyrene", density, nel=2);
19        Polystyrene->AddElement(elC, natoms=19);
20        Polystyrene->AddElement(elH, natoms=21);
21 [...]
22
23        G4double d;  // density
24        d = 8.02*g/cm3 ;
25
26        G4Material* matsteel = new G4Material("Stainless_steel",d,5);
27        matsteel -> AddElement(elMn, 0.02);
28        matsteel -> AddElement(elSi, 0.01);
29        matsteel -> AddElement(elCr, 0.19);
30        matsteel -> AddElement(elNi, 0.10);
31        matsteel -> AddElement(elFe, 0.68);
```

After defining the various materials required in the simulation, the volumes used to describe the actual geometry could be defined. In order to implement the geometry of an experiment, a basic understanding of Geant4's geometry subsystem is needed. In Geant4, the user can define different volumes, which are instances of classes derived from a generic volume class. Geant4 provides rudimentary shapes, such as tubes, boxes, and spheres, as well as more advanced shapes such as a twisted prism. An important principle in the design of Geant4 geometries is the concept of daughter volumes, i.e. volumes which are completely enclosed by another volume, e.g. the volume containing vacuum is located inside the volume describing the vacuum chamber. Utilizing daughter volumes vs. limiting the inner extent of the chamber volume simplifies volume placement, as well as the calculations for particle locations and the volume boundaries. For example, there are two methods of placing a cube inside a larger one, either two cubes could be created, the smaller placed as a daughter volume of the larger cube, or six rectangular prisms may be used to construct a hollow cube around the separately defined inner cube.

The most important volume in any Geant4 simulation is the "world" volume, which acts as a parent for all other volumes, and defines the extent of the simulated system. The actual experimental setup is subsequently placed inside this volume.

Additionally, there are Boolean-logic-like classes which combine volumes, using operations such as AND or OR. The **G4UnionSolid** class was utilized to combine two overlapping volumes into one. This functionality is very helpful, as overlapping volumes in the geometry will lead to errors in the simulation, and the construction of more complicated shapes such as a cross-piece is close to impossible without this functionality.

Listing 2.2: Creating the vacuum chamber and detector volumes.

```
1         G4Tubs  *VertPipe       =       new G4Tubs("VertTube", 0*m, .04*m/2, 180.*mm/2, 0.*deg, 360.*deg);
2         G4Tubs  *HoriPipe       =       new G4Tubs("HoriTube", 0*m, .04*m/2, 135.*mm/2, 0.*deg, 360.*deg);
3
4         G4VSolid*       Cross   =       new G4UnionSolid("Cross_Steel", HoriPipe, VertPipe, detRot, G4ThreeVector(0,0,0));
5
6         Cross_log               =       new G4LogicalVolume(Cross, matsteel, "Cross_Steel",0,0,0);
7         Cross_phys              =       new G4PVPlacement(0, 0, Cross_log, "Cross_Steel", experimentalHall_log, 0, 0);
8
9
10        G4Tubs  *VertPipeAir    =       new G4Tubs("VertTube", 0*m, 34.6*mm/2, 125*mm/2, 0.*deg, 360.*deg);
11        G4Tubs  *HoriPipeAir    =       new G4Tubs("HoriTube", 0*m, 34.6*mm/2, 125*mm/2, 0.*deg, 360.*deg);
12
13        G4VSolid*       CrossAir=       new G4UnionSolid("Cross_Air", VertPipeAir, HoriPipeAir, detRot, G4ThreeVector(0,0,0));
14        CrossAir_log            =       new G4LogicalVolume(CrossAir, Vac, "Cross_Air",0,0,0);
15        CrossAir_phys           =       new G4PVPlacement(0, 0, CrossAir_log, "Cross_Air", Cross_log, 0, 0);
```

```
16          CrossAir_log->SetVisAttributes(green);
17
18          G4Tubs *VertSmPipeAir                       = new G4Tubs("VertTube_Small", 0*m, 26.*mm/2, 24*mm/2, 0.*deg, 360.*
                deg);
19          G4LogicalVolume         *VertSmPipe_log     = new G4LogicalVolume(VertSmPipeAir, Vac, "Vert_Small_Air",0,0,0);
20          G4VPhysicalVolume       *VertSmPipe_phys    = new G4PVPlacement(detRot, G4ThreeVector(0,-125*mm/2-24*mm/2,0),
                VertSmPipe_log, "Vert_Small_Air", Cross_log, 0, 0);
21          VertSmPipe_log->SetVisAttributes(blue);
22
23
24          G4Box   *DetectorBack                       = new G4Box("DetectorBack", 11.*mm/2., 1.5 * mm, 11.*mm/2.);
25          G4LogicalVolume         *detectorback_log   = new G4LogicalVolume(DetectorBack, matSi, "DetectorBack", 0, 0, 0);
26          G4VPhysicalVolume       *detectorback_phys  = new G4PVPlacement(0, G4ThreeVector(0.0*mm, 31.5 * mm, 0*mm),
                detectorback_log, "DetectorBack", CrossAir_log, 0, 0);
27
28          G4Box   *Detector       =   new G4Box("Detector", 9.*mm/2., 0.5 * mm/2, 9.*mm/2.);
29          detector_log            =   new G4LogicalVolume(Detector, matSi, "Detector", 0, 0, 0);
30          detector_phys           =   new G4PVPlacement(0, G4ThreeVector(0.0*mm, -1.25 * mm, 0*mm), detector_log, "Detector",
                detectorback_log, 0, 0);
```

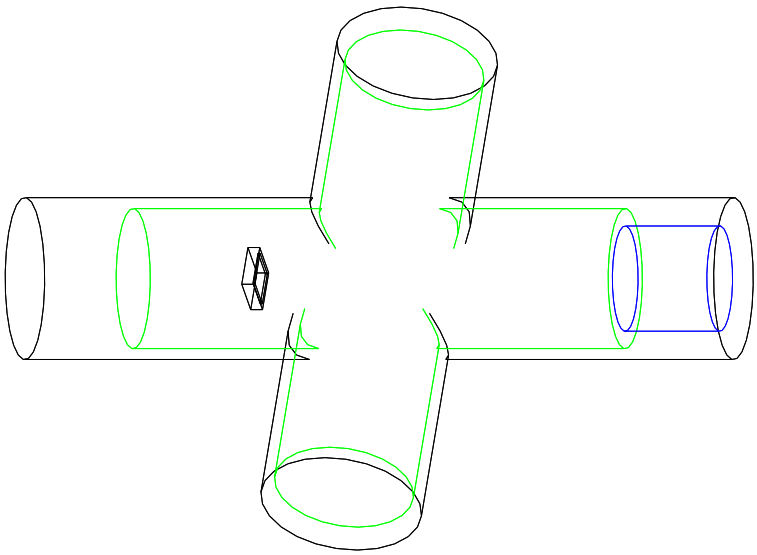

Figure 2.1.: The geometry for the Krypton83m simulation. The interior of the green and blue volumes is filled with vacuum, and the detector is visible floating at the left.

2.1.2. Physics processes

In every simulation, the relevant physics processes must be chosen and activated. Geant4 provides many models of individual processes which can be included, and aggregate models for energy ranges which can be utilized. It is up to the user to choose which model to use, and if necessary adapt and extend this model.

In this case, the Radioactive Decay Model (RDM) was utilized, with the low-energy options activated. The RDM package contains all processes relevant to radioactive decay: the decays themselves as well as the Compton effect, photo-effect, and other processes. With these enabled the unstable isotopes created as events with the General Particle Source (GPS) will immediately decay according to their branching ratios.

2.1.3. Event generation

The next step after selecting the physics and constructing the geometric description is to create events. To achieve this, a class must be derived from the virtual **G4VUserPrimaryGeneratorAction** class. Then the **GeneratePrimaries()** function must be implemented, which is called once at the beginning of every event. As can be seen in listing 2.3, random points are generated in the vacuum via the Von Neumann Method (see section 1.5) in order to generate the starting location of a decay event. Then a random direction is selected, and an event is generated. The particle type was previously defined in the constructor (not shown).

Listing 2.3: Event generator which creates 32 keV particles throughout the volume

```
void SIPrimaryGeneratorAction::GeneratePrimaries(G4Event* anEvent)
{
        if (anEvent->GetEventID() % 20000 == 0)
                G4cout << "Event number: " << anEvent->GetEventID() << G4endl;

        particleGun->SetParticleEnergy(32.*keV);
        G4double X, Y, Z;

        bool    Inside  =       false;
        do
        {

                X = G4UniformRand() * 180 * mm - 90 * mm;
                Y = G4UniformRand() * 180 * mm - 90 * mm;
                Z = G4UniformRand() * 180 * mm - 90 * mm;

                if (X*X+Y*Y < 34.6/2 * 34.6/2 * mm * mm && Z >= -62.5 * mm && Z <= 62.5 * mm)   //      horizontal cylinder
                        Inside  =       true;

                if (X*X+Z*Z < 34.6/2 * 34.6/2 * mm * mm && Y >= -62.5 * mm && Y <= 62.5 * mm)   //      vertical cylinder
                        Inside  =       true;

                if (X*X+Z*Z < 26/2. * 26/2. * mm * mm && Y <= -62.5 * mm && Y >= -86.5 * mm)    //      additional vertical
                     cylinder
                        Inside  =       true;
                if (X >= -4.5 * mm && X <= 4.5 * mm && Z >= -4.5 * mm && Z <= 4.5 * mm && Y >= 29.5 * mm && Y <= 30.5 * mm)     //
                           and not in the detector
                        Inside  =       false;
        }
        while (!Inside);

        particleGun->SetParticlePosition(G4ThreeVector(X, Y, Z));

        G4double direction      =       (G4UniformRand()) * 360 * deg;
        G4double Zdirection     =       std::acos(1 - 2 * G4UniformRand()) * rad;

        G4ThreeVector v(        std::cos(direction / rad) * std::sin(Zdirection / rad),
                                        std::sin(direction / rad) * std::sin(Zdirection / rad),
                                        std::cos(Zdirection / rad)      );

        particleGun->SetParticleMomentumDirection(v);
        particleGun->GeneratePrimaryVertex(anEvent);
}
```

In this simulation, only a single primary particle (or “vertex“) is generated per event. Using repeated calls to **particleGun->GeneratePrimaryVertex()** would result in the generation of several decays per event. This allows the generation of a random number of decays per event. Generating multiple peaks per event would also result in multiple electron peaks appearing in the simulated energy spectrum. The number of vertices per event may be adapted to describe the time resolution of the simulated detector.

2.1.4. Event Detection

Apart from generating events, the software also requires code to analyze what happens during these events, such as recording the energy deposition in a detector, or determining the energy of a particle at any point along its track, both at the boundaries between volumes and during the transversal of a

volume. For this, the default Geant4 toolkit provides several abstract classes which can be extended by the user and then inserted into the tracking and event management routines. For example, the **G4UserSteppingAction** class contains a virtual function called at the end of each calculation step, which is overridden in the derived class with a function that records the pertinent data. In the simulation, this class is instantiated and passed to the Geant4 tracking routines. Afterwards, every time a tracking step is completed, this function is called with the data of the current step. Similar abstract classes exist for entire tracks; these contain functions called when starting and ending the simulation of a track.

For the simulation of detectors, volumes can be defined as "sensitive volumes". Doing this links the volume to an instance of a class derived from **G4VSensitiveDetector**, which contains functions which are run at the beginning and end of every event, as well as each time a physics process returns a "hit", simulating energy deposition in this volume. It is also possible to link an instance of a **G4VSensitiveDetector** class to multiple volumes. Thus, when simulating a PET system and searching for coincidences, or simulating multiple detectors with no interdependencies, an instance of this class may be used for all detectors, or instances of different classes derived from **G4VSensitiveDetector** may be used for different detectors. An example of this is the simulation of veto detectors, which would record time intervals during which they are active, while the main detectors record the arrival time and energy of particles.

As the intent of the ^{83}Kr simulation is the calculation of the solid angle of the detector, the only information required is the total energy deposition in the detector per event, and additionally the incident angle for a possible backscattering correction. However, neither the precise interaction types nor the exact interaction locations of individual energy depositions caused by multiple physical interactions of the same electron are needed. The derived class generates both a histogram containing a binned energy spectrum, and a listing of all events in an output file for further analysis. At the beginning of each event, the total energy deposition is set to zero and then incremented during each energy deposition "hit". At the end of the event the total energy deposition is used to increase a bin in the histogram, as well as output the data in the list file. After the simulation is finished, the contents of the histogram are also stored.

In order to store the incident angle, the **G4UserSteppingAction** class is subclassed. The derived class checks whether the track crosses from the vacuum volume into the detector volume during the current step, and, if this is the case, records the incident angle.

2.1.5. Event interpretation

In order to understand the results which are generated by these simulations and to compare these with results from real-world experiments, the generated spectra may be adjusted in order to account for various possible effects. In the demonstration simulation, the most important difference is that the energy resolution is infinite, which may result in spectra which appear to be incorrect. However, either the histogram or the event-by-event energy deposition log may be multiplied with a known energy resolution function to convert these spectra into estimated real-world spectra. When simulating a full ^{83}Kr spectrum this broadens the peaks, thereby reducing the number of perceived peaks. Figure 2.2 shows this broadening effect in the spectrum resulting from simulating

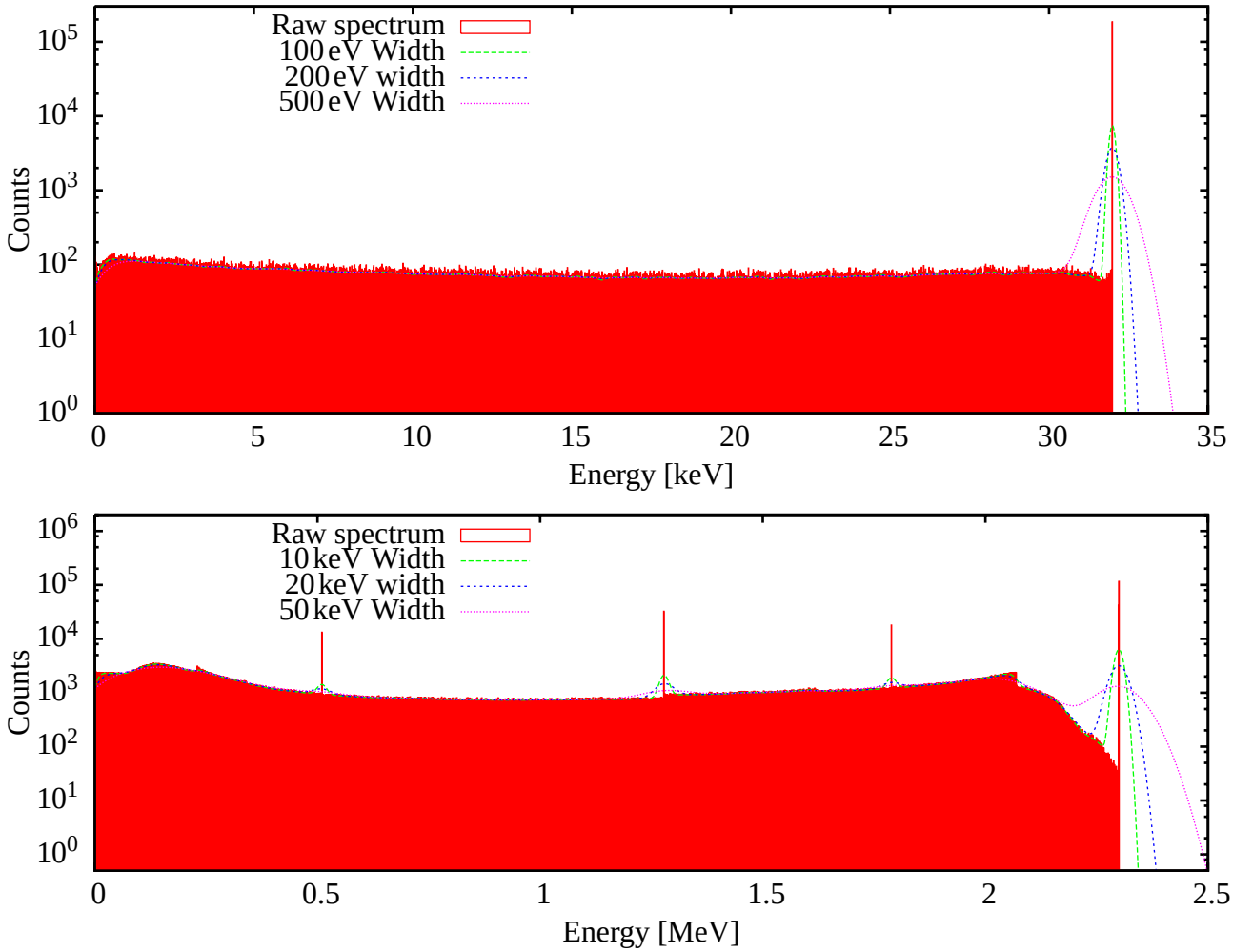

Figure 2.2.: Top: The resulting energy distribution measured when using 32keV electrons as primary particles in the ^{83}Kr simulation, along with three broadened distributions for different detector resolutions. **Bottom**: The resulting energy distribution when simulating a 2.3 MeV gamma source with a shielded germanium detector, along with similar broadened curves.

only electron events, as well as in the gamma energy spectrum produced by another simulation of a high-energy gamma source.

2.2. Advanced Geant4

2.2.1. Geometry import

Starting with version 4.9.1, Geant4 natively supports the import of GDML files. Previous to this, additional libraries had to be included. GDML itself is an XML extension designed to exchange geometric information between different applications.

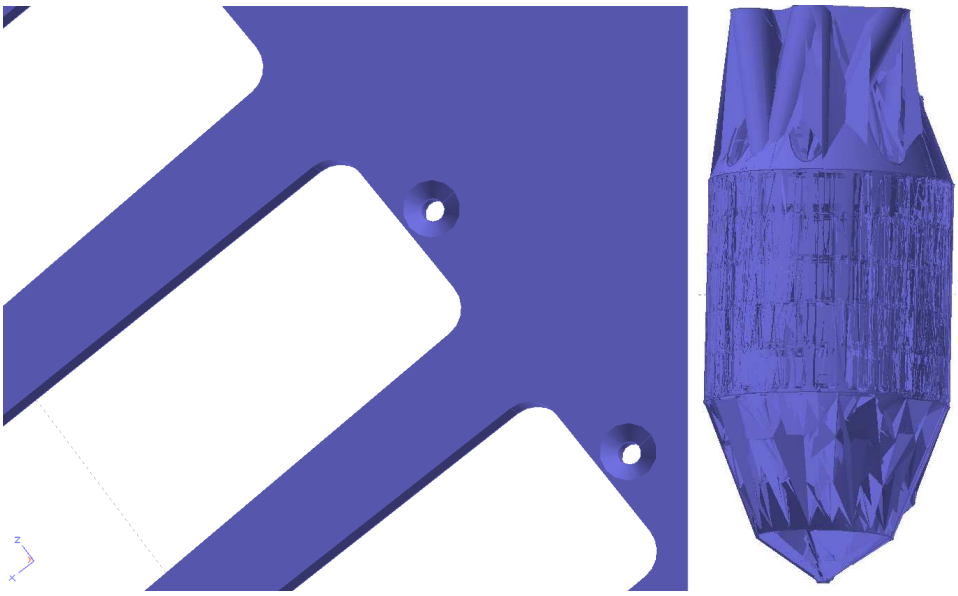

Figure 2.3.: Left: The results of converting a comb from CAD to .gdml format. Visible is the very high detail level, which translates to a very large memory requirement, and results in a very accurate representation. **Right**: The inported main spectrometer vessel, which unfortunantly was unsuccessfull.

We attempted to use the GDML format to import the KATRIN geometry. The only program available which could export to the GDML geometry format, FastRAD by TRAD[2], was unable to read anything but .STEP (AP203, AP214) files. This required us to first export the Inventor CAD files to .STEP format, load these files into FastRAD, and then export the loaded geometry as a set of GDML files; during this export, the geometry data is discretized into triangular surfaces. Finally, when loading the GDML files into Geant4, these are representated as tessellated solids (**G4TessellatedSolid**). The direct conversion of .STEP files to GDML while keeping the true shapes is currently not possible. This is most likely due to the different design approaches in the representation of geometry data: CAD files often utilize extruded solids which are insufficiently supported in Geant4.[3]

The detailed discretization leads to a large memory requirement, as a simple cylinder require many triangles in order to be approximated well, instead of only the height, inner radius, and outer radius. In addition this leads to a slight loss in geometric precision. While converting a subsection of the inner electrode system as a test, using high precision, resulted in a memory requirement of over 2GB[4].

The primary reason why direct conversion was not used was the fact that the conversion of the main spectrometer vessel failed spectacularly as is shown in Fig. 2.3, leading us to doubt the accuracy of other converted geometries. As the discretization generates a large amount of surfaces,

[2]TRAD: Tests and RADiation. http://www.fastrad.net

[3]Geant4 currently only supports an extruded polygon, while CAD programs allow the extrusion of circles and other shapes. Also, Geant4 cannot limit extruded solids by their intersection with another solid.

[4]In the future it may be possible to reduce this extremely large memory footprint by optimizing the use of repeated volumes by the GDML module of Geant4, however currently Geant4 only supports repeated volumes as CSG solids, while the tessellated solids required for GDML import are BREP volumes.

these exceed the surface count limit of the electromagnetic tracking code, as the memory usage is proportional to the square of the volume count, and computation time to the cube.

The optimal solution to the issue of geometric description is a unified apporach for the generation of the various types of geometric descriptions; creating a program which uses configurable parameters to generate either Geant4 volumes via the use of non-discretized GDML, and a corresponding ELCD3.3 formatted output file for the electromagnetic tracking. This would ensure the simulation uses a consistent geometric model and allow easy version management. Currently, the tool developed by S. Voecking[Vöc07] and updated by M. Zacher[Zac09], MainSpec, is used to generate the ELCD3.3 geometries with approximations, which are then imported into Geant resulting in a loss of precision; an alternative method is creating the geometry directly in Geant4. Such a unified tool has recently been discussed during the MC-BASI phone conferences.

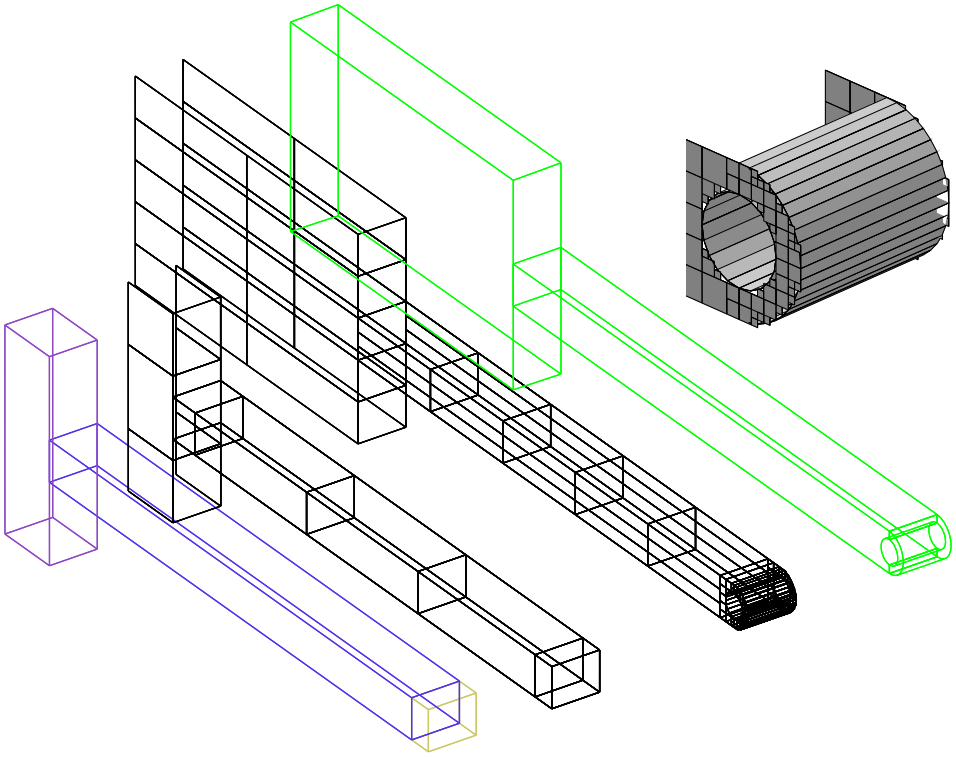

Figure 2.4.: Far Left: Basic tooth model constructed with Geant4 primitives. **Left**: Basic tooth model constructed with rectangular electrodes. The low number of surfaces enables a rapid calculation of the electric potential. **Right**: The advanced tooth model constructed out of rectangular electrodes (ELCD3.3 description). The high discretization required for the tooth head is visible. **Far right**: The new tooth design in solid form, containing an opening for the wire, as well as a rounded head. **Inset**: Close-up view of the head of the more detailed tooth model.

A more detailed tooth model was required for simulations of the electrode endcap design by F. Glück. This was used as a testcase, with a C++ Tooth class written which has configurable parameters for the radius of the comb and the required discretization if generating ELCD3.3 output, as well as containing a function which uses the same internal geometric information in order to create

a solid Geant4 volume accurately portraying the teeth (see Fig. 2.4 for a comparison of the old and new tooth models.

2.2.2. Low-energy shortcomings

Geant4 unfortunately has a lower limit of 250 eV for all low-energy processes[5], under which secondaries are not created; this results in an inadequate representation of the lowest energies of the background, which was the primary goal of the planned simulations. While it was possible to override this limit by modifying the cuts below which particles are aborted, reviewing the physics process code showed that many physical process implementations use binned input data for this low-energy region, this would result in an incorrect result at these energies. In addition, this would not magically add support for low-energy phenomena which can be ignored when one works with MeV and TeV energies, such as phonons and plasmons, (quasi-) crystal structure effects, localized work functions and the influence of the work function in general, and so on.

Therefore, a measurement of the low-energy spectrum of secondary electrons emitted from a stainless steel surface due to the impact of cosmic muons was attempted in Mainz, intending to use this data to implement a custom physics process which would generate secondary electrons on the surface of the simulated spectrometer at the exit points of muons passing through the spectrometer components. Due to unforeseen circumstances[6], these measurements did not result in a low-energy spectrum, but rather resulted in the need for further experiments. One such experiment was then conducted in Münster (see chapters 4 and 5 for details); it resulted in an accurate representation of the angularly dependent yield of low-energy secondary electrons; however this experiment was not able to determine a precise energy distribution for these electrons, only an upper limit of some hundred eV was determined for these electrons.[7]

2.3. Simulation of the KATRIN main spectrometer

2.3.1. Geometry

The SIKatrin simulation includes different approaches to defining the experimental geometry, either via importing and parsing ELCD and Magfield input files, or via the direct definition of the geometry, as well as a combination of both these methods. Additionally, stub code is in place for a future return to GDML import. Conventions used in previous geometrical descriptions were maintained, resulting in the Z-axis corresponding to the beamline, the X-axis corresponding to the width, and the Y-axis corresponding to the height.

The ELCD option uses a custom parser which can load ELCD3.2, ELCD3.3, and MagField2 as well as MagField3 files.

[5] The newly released G4DNA processes are now an exception. These, however, are not applicable since an ideal spectrometer would not contain biological material requiring the simulation of interactions between particles and DNA, and if it did, the precise energy deposited in such materials would not be relevant.

[6] The actual electron emission rate $Y_{\mu-\mathrm{SE}}$ not matching expectations.

[7] Limited by the statistics and the detector resolution.

ELCD3.2 files, which describe rotationally symmetrical geometries, store a collection of line segments equivalent to a 2d cut through the 3d object. However, these lines describe the full inner surface of the spectrometer, ignoring the outer surface, which results in infinitely thin volumes. In order to partially correct for this, the collection of line segments is scanned for enclosed shapes by linking the endpoints of each wire segment with all other wire segments sharing this endpoint, and then recursively searching for loops in the resulting structure. If any loops are located, these are assumed to be enclosed shapes, and equivalent polycones are added to the geometry. For the remaining surfaces very thin conic sections are used and the structure remains infinitely thin.

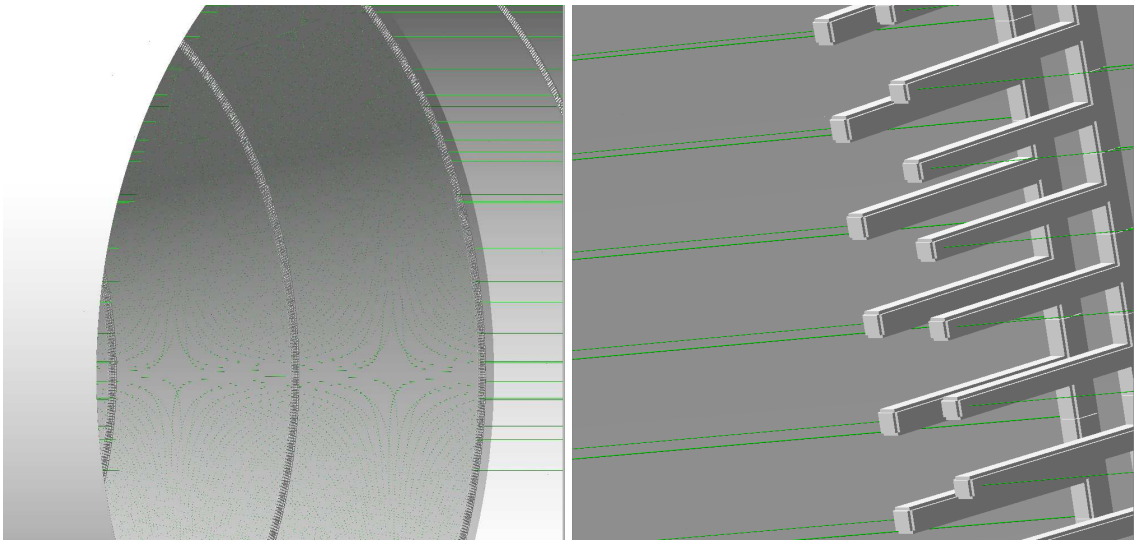

Figure 2.5.: Left: View of half the Katrin spectrometer, including inner electrode systems, created via parsing of elcd datafiles. **Right**: Closeup view of the teeth. The 2D rectangles were given a large thickness in order to illustrate the issues with overlaps which are encountered when creating three-dimensional shapes from a two-dimensional description; in actual simulations the rectangles were of a much smaller, but still finite, thickness.

ELCD3.3 files are not analyzed for structures, as during their generation the hollow cones representing the main spectrometer and inner ring electrodes are approximated with many rectangular electrodes, therefore, reconstructing the original shapes is close to impossible. Massive cylinders orientated along the Z-axis however are not discretized as long as they are solid, these massive cylinders and rectangular surfaces are directly inserted into the simulation geometry. Figure 2.5 shows the spectrometer along with the wire electrode system.

Both types of MagField files can only contain massive cylinders with a fixed inner and outer radius describing the location of the magnets, these shapes can be directly constructed in Geant4 using instances of the **G4Tubs** class.

The CAD-RAILS and CAD-NORAILS option uses preprogrammed functions and sizes in order to directly create the main spectrometer vessel, with the values taken from the original CAD designs. Unlike in the ELCD geometries, the three large pump ports are included;, with CAD-RAILS specified, the rail system used to mount the inner electrode can also be created. Figure 2.6 shows the constructed main spectrometer.

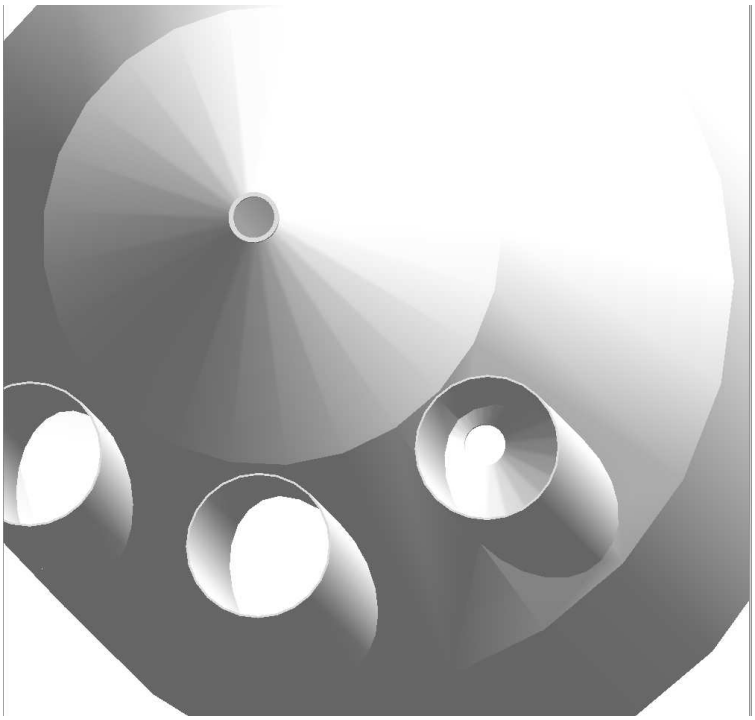

Figure 2.6.: A view of the hardcoded SIKatrin main spectrometer, the entrance of the spectrometer is visible in the bottom right pump port. The actual shape is round, the angular appearence stems from the OpenGL viewer.

Lastly, MIXED-RAILS and MIXED-NORAILS are available, which create the spectrometer vessel using the previously described CAD option and also load ELCD files. The electrode surfaces which describe the spectrometer must be removed from the loaded ELCD files in order to prevent volume overlaps which might lead to incorrect results. See section 2.4 for a simulation run with this geometry option, simulating the number of cosmic muon hits on various spectrometer components.

2.3.2. Event generators

The SIKatrin simulation includes two different event generators. The first one is designed to generate cosmic muons. Muons with incident angles generated according to the angular spectrum described in section 1.4.3 are created together with starting locations which are distributed homogeneously on a $1\,\mathrm{km}^2$ plane above the spectrometer. An initial test is done to determine where a muon with a specific incident angle and location would intersect the plane below the spectrometer; using the starting and ending X and Z values, it is determined whether this muon passes through a 20 m by 20 m by 70 m cube around the spectrometer[8]. If the muon does not enter this box, the event is rejected, the event counter increased, and a new muon is generated. If, however, the muon enters this volume, an energy and muon type ($\mu+$ or $\mu-$) are selected according to the distribution measured by [Kre99]. Alternatively, "geantinos" may be used as the incoming particle; these have no

[8]This large size allows the future inclusion of the prespectrometer as well as the full beamline

associated physics processes and thereby do not interact, enabling very fast computation times for simulations solely utilizing UserStepping- and UserTracking-based routines for data generation.

Due to the rejection of a large number of events and the low maximum of the internal Geant4 event counter, the internal counter is not updated with the value of the muon generator's internal counter as otherwise the simulation runs would end very quickly. In order to determine the true muon count, the muon generator's internal counter is outputted every 100K events and also stored in a file at the end of a run.

The second generator was designed as a general-purpose event generator which can handle all types of radioactive sources required for the simulation of backgrounds emitted from the tank materials. Therefore, this class utilizes a General Particle Source (GPS) in order to be able to either generate secondary particles directly (e.g. electrons, gammas), or simulate a full decay scheme of an unstable isotope using the relevant decay channels. This generator can either generate the decays on the surface of the physical volumes[9], or in the actual spatial volumes of the physical volume.

In addition, the generator can select a subgroup of the created physical volumes, within which or upon which the events are then placed. For this, either a material or an isotope is selected. Then, the event generator searches the entire geometry (or optionally all daughter physical volumes of a given physical volume) for physical volumes composed of this material or containing the given isotope. Using the found physical volumes, a linked list is generated which stores the spacial volume[10] of each individual physical volume, as well as the total spacial volume of all physical volumes found so far, thereby allowing a quick location of the physical volume concerned when generating a decay location. By storing the final list in an array with each element N storing the cumulative total spatial volumes of the elements $1...N$, and generating a random number between zero and the total spacial volume V_s, the element with the smallest total volume greater than the generated volume can be found in $O = ln(N)$ time, enabling quick event localization even when using very complex geometries. Then a random point is generated either within the physical volume or on its surface.

Alternatively, the event generator may load a binned energy spectrum and then generate particles with this energy distribution. This is useful in situations where the electron energy spectrum at the surface of a material was experimentally determined, e.g. the planned result of measurements in Mainz in the case of muons, for energy ranges where Geant4 physics are not applicable, or in order to save CPU time by first determining the energy spectrum at the surface of a given material through a given process in a separate smaller simulation, then using this to start a simulation with the full KATRIN geometry.

2.3.3. Electromagnetic tracking

There are also two alternative methods for electromagnetic tracking, either using a modified version of eltraj, the tracking program which uses F. Glücks's electromagnetic field routines, or using

[9] Physical volumes refers to the shapes created when generating the actual geometry, e.g. a box, while spatial volume is the inner extent of these volumes, e.g. $10\,\mathrm{cm}^3$

[10] Or surface area if generating decays on the surface

the Geant4 port and refinement of this code, KatrinField, done by T. Corona[Cor09], an initial version of which has recently been completed. KatrinField also adds support for triangles, as well as distributed calculations. The inclusion of triangles allows future simulations to fully divide all cones into surfaces, preventing gaps between sections.

The first tracking method of involves several custom physics processes and stepping classes. This also involves running several instances of SIKatrin in parallel performing different tasks, as well as the external tracking program, therefore a MySQL database is used to exchange the data. A custom **UserSteppingAction** removes electrons from the main GEANT4 simulation (Instance one) as they enter the vacuum, storing position, direction, energy, etc. in the database after having offset this particle from the surface by some few hundred nanometers, defining the initial distance to a volume D; subsequently, this instance of SIKatrin starts simulating the next event. The electromagnetic tracking application reads particles stored from the database, and tracks these until a maximum of D distance has been covered from the starting location, then updating the position, energy and direction in the database, as well as setting the minimum distance to zero. The second instance of the SIKatrin simulation updates the minimum distance between the stored electrons and the nearest surface. These two steps are alternated until the electron again reaches a defined minimum distance to the surface. A third instance of SIKatrin loads the electrons approaching the surface, simulating the resulting collision with the surface and propagation within the solid. If the electron reenters the vacuum or secondary electrons enter the vacuum, these are updated respectively added to the database, restarting the tracking cycle. Figure 2.7 shows a flowchart of this process. This architecture easily scales until becoming bottlenecked by the performance of the database.

With the completion of a preliminary version of KatrinField, this code was included in the simulation. This allows a single instance of SIKatrin to fully track events, requiring no database interactions. This was used in the simulation of the transmission function of the Münster Muon Experiment, which is described in detail in chapters 4 and 5. This implementation is fully scaling as well.

2.3.4. Tracked Events

The simulation can optionally store all events with track and step information in a MySQL database, for later analysis. In the future, a minimal Δ-distance should be used in order to reduce the amount of incoming data, only storing the information every few steps.

The stored energies and locations of electrons entering the vacuum may be used to either generate secondary electron energy spectra or spatial distributions (see Fig. 2.10 for an example). While only test runs were conducted with electromagnetic tracking and the full geometry, the data stored during such runs can be used to generate a density map of the electron distribution in the actual spectrometer, or a density map of the positions where electrons hit the spectrometer surfaces after traversing the vacuum.

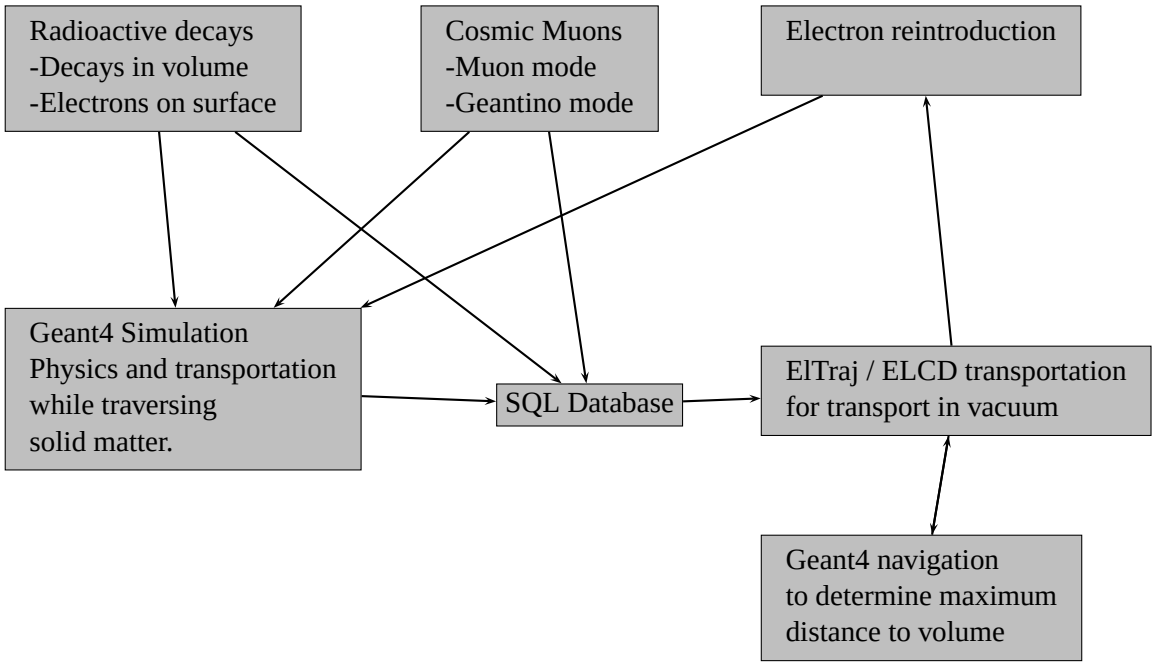

Figure 2.7.: The dataflow required to track secondary electrons with the modified eltraj version. The three Geant4 event generators are at the top. Two of these generate primary events and store the starting conditions in the SQL-database. The secondary electrons are tracked by the Geant4 simulation until they enter vacuum, at which point they are stored in the SQL database. An instance of the eltraj program then tracks these electrons through the vacuum, until they exit the vacuum. These are then simulated by the Electron reintroduction event generator, and the cycle is repeated.

2.4. Simulation of the cosmic muon background

As mentioned previously, one of the primary expected background sources in KATRIN is the secondary electron background caused by the passage of cosmic muons through the main spectrometer. The SIKatrin simulation was used to determine the number and locations of cosmic muon hits on various components of the main spectrometer as well as on the shielding electrode, and to determine the expected secondary electron rate from this information.

In order to achieve reasonable statistics for the spatial distribution of the low-energy secondary electrons, the geantino mode of the cosmic event generator was used. More energetic electrons were simulated via the usage of Geant4 physics; additionally, two energy spectra were generated by a simulation of bombarding solid stainless steel plates (thickness 20 mm and 0.2 mm) with muons to determine the influence of the electrode thickness.

The MIXED-NORAILS geometry was used for the simulations, employing the electrode configuration of 2009-01-09. All muon intersections with spectrometer volumes were recorded; the stored information included the volume name, the intersection location, the muon momentum direction, and the angle between muon and surface normal. Table 2.1 shows the resulting number of hits on the different components in the simulated geometry and the corresponding low-energy electron count using the measured electron yield $Y_{\mu-\mathrm{SE}}(\beta)$ (see chapter 5 for details).

A simulation using full electromagnetic tracking was not feasible since tracking a single electron takes several minutes and a very large number of events is required for acceptable statistics. For this reason, the number of electrons entering the inner spectrometer was estimated. In addition, the fact that the precise energy distribution of low-energy secondaries was unknown restricted the precision of the determined background rates for electrons originating from behind the inner wire layer. However, the calculated initial low-energy secondary electron count is accurate within the margin of error of the experimental results used as input.

The hitcount on the spectrometer vessel was reduced by a factor of 2, as a hit was recorded every time a muon entered or exited the main spectrometer volume. This included the outer surfaces which do not affect the background count rate. For example, a muon with an incidence angle of 0° would first hit the outside of the main spectrometer, then, when leaving the 32 mm thick wall, record a second hit, and after traversing the ten meters of vacuum record a third and fourth hit while passing through the bottom wall of the spectrometer.

2.4.1. Corrections

The pump ports were included in the geometric description of the spectrometer. However, we also calculated the different intersection rates, removing all events which only intersect the pump ports. As the pump port openings (later to be covered by mesh electrodes) are located behind the wire electrode and contain a constant electric field, we believe that electrons created by intersections in this area will not affect the actual background count rate. In addition, those hits which do not pass through the central vacuum area would distort the probability of a muon which hits the tank also hitting a portion of the electrode system.

Component	Hits	Rate [Hz]	Eff. Area [m^2]	LE-e^-	LE-e^- [Hz]
Main Spectrometer	65981253	101414	536.6	1291611	1985
Pump Ports	7760166	11927.5	63.11	147805	227
Wires	3684299	5662.81	29.96	71157	109
Endcaps	530998	816.150	4.318	10211	16
Combs	5601062	8608.9	45.55	118484	182
Full Metal Electrodes	679430	1044	5.525	13156	20
Total	84237208	129474	685.	1652424	2540
Total w.o. Pump Ports	76477042	117546	622	1504619	2313

Table 2.1.: The simulated frequency of muon intersections with various components of KATRIN, along with the corresponding secondary electron count rate (with a factor two correction for the spectrometer vessel, pump ports, and combs). A total of $\approx 1.23 \cdot 10^{11}$ muons were simulated, the negligible statistical errors are not shown. The errors of the low-energy electron yield and resulting frequencies are identical to the error in the determined electron yield, $0.98 \pm .14\%$

As the current ELCD3.3 datafile format does not allow for an explicit naming of components when creating the geometry, the simulation is unable to distinguish between the rectangles making up the comb structure, and those rectangles which are used to describe the full-metal anti-penning and ground electrodes. Therefore, the intersection locations were used to discriminate between components. This was necessary because the simulation counts a muon passing through a rectangular electrode as two hits; the hollow comb structure therefore leads to a comb hitcount twice as high as the actual hit rate. The muons passing through the full-metal electrodes are also counted twice; however, in this case, both hits are physically relevant. Future runs should split the imported ELCD geometry into two or more files in order to allow easy separation of electrode components, or extend the ELCD file format to include explicit component names.

A last issue which we could not correct was the fact that the used ELCD3.3 description of the comb structure does not properly describe the comb base (due to memory and CPU limitations, see [Val09] for details on the comb model). As can be seen in fig. 2.4, the back of each tooth is open; in addition, the extent of the tooth base is shortened.

However, for the low-energy background, the muon intersections here can be safely ignored. Any electrons ejected from the sides of the combs would have to have a lateral energy of at least 100 eV in order to pass through the wire electrode, and as the maximum energy of the low-energy background electrons being simulated is on the order of a few hundred eV, with an isotropic secondary electron emission, this is extremely unlikely.

In addition, any electron ejected from the outward-facing comb surface cannot be directed towards the center of the spectrometer. In order to simulate intersections here, the MainSpec program generating the wire electrode geometry must be adapted to use the advanced tooth model with a full-sized base, which is shown in fig. 2.4, which results in a more accurate comb structure and introduces difficulties in the electromagnetic tracking support.

Approximately half the electrons ejected from the wires of the electrode system[11], should be

[11] An exact percentage needs to correct for the curvature of the wire layer. Additionally, the intersecting magnetic field

ejected towards the walls of the spectrometer, while a local electric potential also accelerates these towards the walls. This leads to an upper limit of 50% of the electrons ejected from the wires being able to contribute to the background. The situation is different for the electrons emitted from the various full-metal electrodes, which is due to the varying fieldstrengths between the electrodes as well as the higher local magnetic field at the ends of the spectrometer vessel. Therefore, no correction factor will be applied to the number of electrons originating from these full-metal electrodes. However, the number of secondaries ejected from the combs is reduced by a factor of two as well because of the isotropic angular distribution: half of these secondaries are ejected directly towards the spectrometer vessel, and therefore will be discounted. Last, the endcaps also require a correctional factor; these are U-shaped metal sheets covering pairs of adjacent combs; therefore, all electrons originating from the inner surfaces of these structures must travel towards the spectrometer walls.

These corrections are based on the assumption that the energies of the secondary electrons have an upper limit of some hundred eV, resulting in an conservative upper limit for the background. However, the energy distribution of the muon-induced secondary electrons most likely is similar to the energy distribution of electron-induced secondaries, which peaks at 16 eV, with almost all secondaries having energies below 25 eV. In this case, a drastically lower upper limit follows, resulting from a drastically reduced contribution of secondaries from the comb structure (below 5% instead of 50%), with a portion of the remaining electrons removed by the endcaps. Also, the electrons ejected from the outer wire layer would be unable to cross the potential barrier created by the inner wire layer, reducing the electron count originating from the wires by 60%. Furthermore, all electrons ejected from the back of the inner wire layer are accelerated to the spectrometer vessel, leading to an additional reduction factor of 50%. This leads to a total reduction of electrons originating from the wires by 80%.

2.4.2. Results

The geantino run generated a total of $N_\mu \approx 1.23 \cdot 10^{11}$ primary muons on the square kilometer plane A_{plane} above the experimental setup, resulting in $N_{\text{Hits}} = \approx 36 \cdot 10^6$ muons hitting any portion of the spectrometer at least once. Table 2.1 shows the number of hits and corresponding rates before corrections were applied, split by spectrometer component; the incident angular spectra as well as the resulting number of electrons is shown in Fig. 2.8. Using the expected cosmic muon rate of $R = 189/(\text{m}^2\text{s})$ (taken from [Bog06]), we can calculate the total time elapsed during the simulation run:

$$t_{\text{run}} = \frac{N_\mu}{A_{\text{plane}} \cdot R} \tag{2.1}$$

$$\approx \frac{1.23 \cdot 10^{11}}{10^6\,\text{m}^2 \cdot 189/\text{m}^2\text{s}} = 650\,\text{s} \tag{2.2}$$

With this total time, we can then use the number of unique muon hits on the entire spectrometer or any other subcomponent in order to calculate a muon hit frequency:

lines may also contribute to a change of the correctional factor, as the retarding field biases the ejected electrons towards the outsides of the spectrometer, with the magnetic field line spacing reduced in this direction guiding the electrons through the wire electrode.

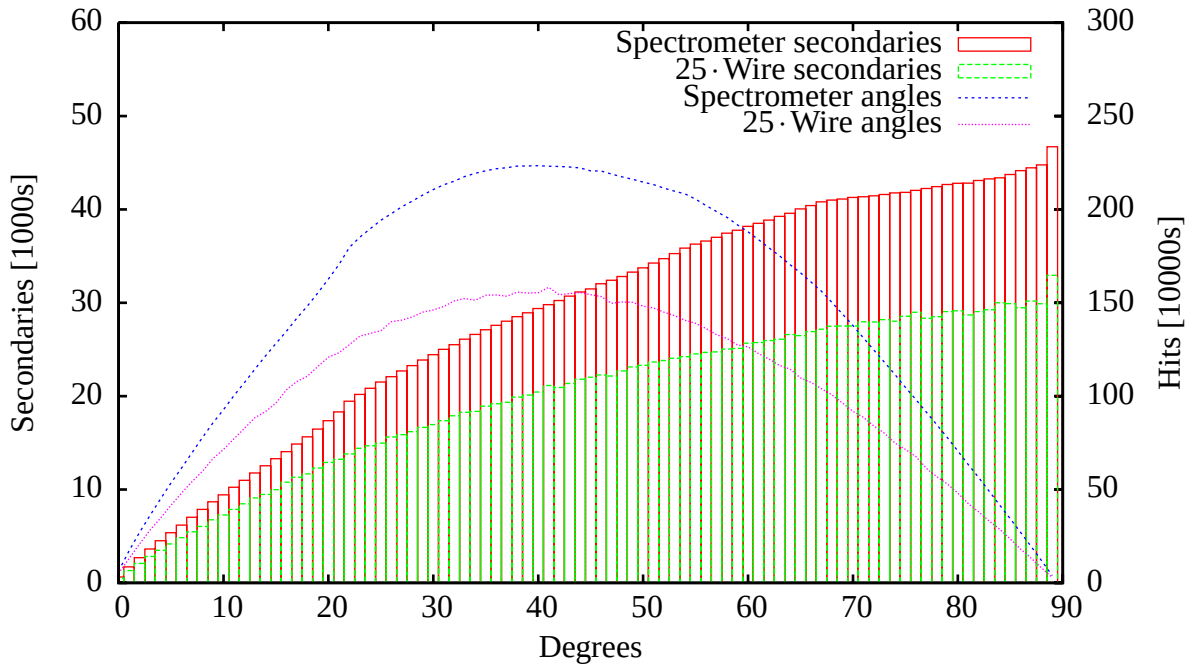

Figure 2.8.: The distribution of intersection angles between primary muons and the spectrometer as well as the wires of the electrode system, along with the corresponding count of secondary electrons produced by these muons. Even though very few muons have very large incident angles, these still contribute substantially to the total electron count rate.

$$f = \frac{N_{\text{Hits}}}{t_{\text{run}}} \tag{2.3}$$

or at the effective spectrometer surface visible to the muon flux:

$$A_{\text{Spectrometer}} = \frac{N_{\text{Hits}}}{t_{\text{run}} \cdot R} = A_{\text{plane}} \cdot \frac{N_{\text{Hits}}}{N_{\mu}} \tag{2.4}$$

This last factor is independent of the incoming muon rate R.

Likewise, we can use the hitcount on any component in order to calculate the number of secondary electrons originating from this component. In order to do this, we need to determine the secondary electron yield of every recorded hit using $Y_{\mu-\text{SE}}(\beta)$ (see section 5.3), and sum these, which results in the corresponding count rate.

$$N_{e^-} = \sum_{n=0}^{N} \bar{Y}_{\mu-\text{SE}-\text{Abs}} \cdot \frac{1}{\cos(\beta_n)} \tag{2.5}$$

The corrected expected low-energy secondary electron count rates emitted from all subcomponents are listed in table 2.2. The incident angle spectra of all components are similar, an example of which is shown in Fig. 2.8.

While we cannot determine the full shielding efficiency of the wire electrode without a fully tracked run, assuming all low-energy electrons emitted from the spectrometer vessel are blocked, as well as half the electrons ejected from the wire layers[12], results in an electron rate of 55 Hz from the wires of the electrode, which is 35 times smaller than the rate of the spectrometer vessel. The contribution factor by the combs is 182 Hz, assuming all electrons emitted from the comb area enter the main vacuum.[13] While endcaps are in place to reduce the contribution of background originating from the combs, without tracking the reduction cannot be quantified and therefore is not applied.

This results in a total low-energy background electron rate reduction factor of 12 in the main spectrometer, i.e., 12 times as many electrons originate from the spectrometer vessel which would enter the vacuum without the electrode system as originate from the electrode system which is in place to deflect these electrons. Full results are listed in table 2.2. The acceptable allowed background is 10 mHz at the detector; assuming the reduction factor of the electromagnetic fields is similar to Mainz (10^5), the background contribution of these electrons would be ≈ 1.7 mHz, which is well beneath the upper limit.

Component	Hits (corrected)	Rate [Hz]	Effective Area [m^2]	LE-e^-	LE-e^- [Hz]
Main Spectrometer	0	0	0	0	0
Pump Ports	0	0	0	0	0
Wires	1842149.5	2830	15.0	35580	55
Endcaps	265499	408	2.16	5106	7.9
Combs	2800530.75	4304	22.8	59240	91.1
Full Metal Electrodes	679430	1040	5.53	13160	20
Total	5587609	8588	45.4	113100	174

Table 2.2.: Upper limits for the number of low-energy secondary electrons which may contribute to the background, split by component, after applying the corrections for the case of an upper limit in energy of the secondaries of 200 eV. These corrections include the assumption that all background which originates from the spectrometer vessel is blocked by the wire electrode, and a factor 2 reduction for the electrons originating from the combs, endcaps, and wires. An error of $\pm 5\%$ is assumed due to the estimates used for the reduction factors.

A less conservative approach which assumes that the secondary electrons have energies below 25 eV, which is most likely the case, leads to a much lower background rate, namely, a total background electron rate of 60 ± 30 Hz, resulting in a wire electrode shielding factor of $33 \pm 50\%$. With the same electromagnetic reduction factor applied, the rate expected at the detector due to this background component is 0.6 ± 0.3 mHz. The full results, again split by component, are shown in table 2.3.

A second simulation run was conducted on the IKP cluster using the high-energy Geant4 physics in order to quantify the high-energy secondary electron yield. As with the low-energy simulation,

[12] Most likely, the majority of electrons ejected from the outer layer are reflected by the 100V potential difference, however, without an exact energy spectrum, this factor will have to be disregarded.

[13] This cannot be precisely determined due to the unknown electron energy spectrum. We assumed, that 100% of all electrons ejected enter the vacuum. Most likely, the electron energy spectrum peaks near some few eV; in this case, the true factor would be closer to 1%.

Component	Hits (corrected)	Rate [Hz]	Effective Area [m^2]	LE-e^-	LE-e^- [Hz]
Wires	736860	1133	6.0	14230	22
Endcaps	265500	408.1	2.2	5106	7.9
Combs	280050	430.4	2.3	5924	9.1
Full Metal Electrodes	679430	1044	5.5	13160	20
Total	1961900	3015	16	38420	59

Table 2.3.: Upper limits for the number of low-energy secondary electrons which may contribute to the background, under the assumption that the energy spectrum of these electrons is similar to that of the electron-induced secondaries. Again, the rates are split by component, with the more stringent corrections applied. The wire count rate is reduced by 80% and the comb count rate by 95%. However, the additional factor of 50% derived from the isotropic distribution of the perpendicular angular momentum component of the electrons ejected from the combs, which had originally been applied, is no longer valid. The resulting rates have a large error of 50% due to the uncertainties present in the estimates used.

the secondaries are listed by the component from which they originate. However, unlike the previous simulation, gammas are also produced by interactions in tertiary processes. The total energy spectrum is shown in Fig. 2.9 normalized to the rate per eV, along with the spectra of the wires. The usage of ultra-thin combs and full-metal electrodes resulted in a nonexistent count rate for these components, which are not shown for this reason. The statistics of these runs are not optimal because of the large amount of CPU-time needed; these results required $\approx$ 25000 CPU-hours. These exhibit a high gamma background count rate.

Component	HE-e^-	HE-e^- [Hz]	HE-γ	HE-γ [Hz]
Main Spectrometer	368200	4610	2577000	32300
Pump Ports	41420	519	553400	6930
Wires	2156	27.0	342	4.28
Totals	411700	5160	3131000	39200

Table 2.4.: The number of high-energy secondary electrons which may contribute to the background, split by component, after applying corrections. Due to the nature of the simulation no secondaries were produced in the ultrathin combs and full metal electrodes.

2.4.3. Outlook

These simulations have shown that Geant4, even without full low-energy support, can be used to simulate backgrounds for the KATRIN Experiment. The next step consists of fully tracked simulations, which would eliminate errors induced by the estimations used earlier and may even highlight potential trouble spots that current analysis methods cannot predict. In addition, a measurement of the precise low-energy electron spectrum would allow calculations of the background caused by the cosmic muons with higher precision, and a more thorough understanding of the background reduction offered by the wire electrode system. A future unified-geometry approach could increase the precision with which the geometry of the spectrometer is simulated, reducing errors induced

here, as well as allow for a more accurate distribution of radioactive decays and the generation of high energy secondaries from muons in the background simulations. The tools to create density maps of electrons have been tested, an example of the incident muon density distribution is shown in Fig. 2.10.

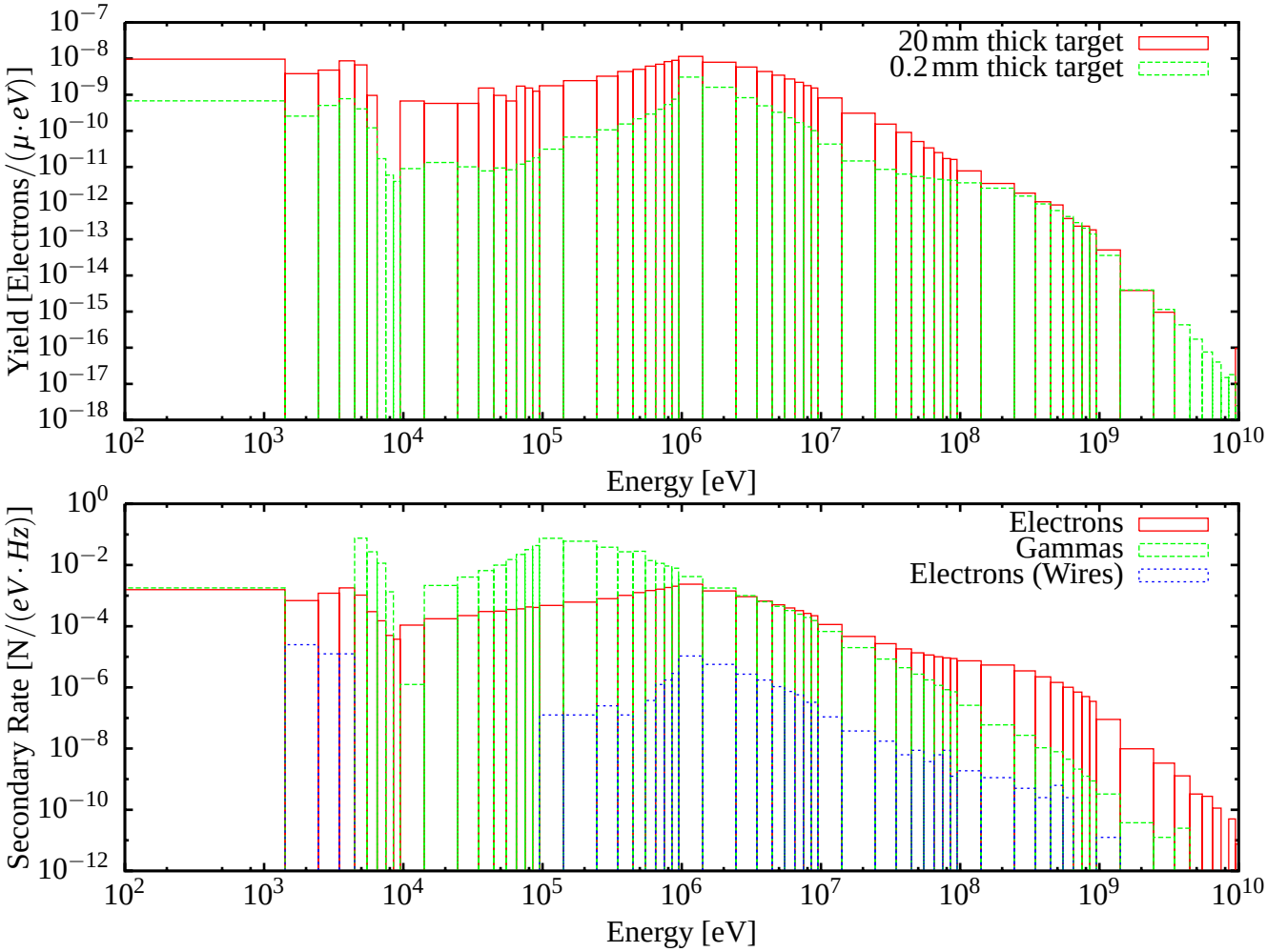

Figure 2.9.: Top: The number of high-energy secondaries is shown for muons passing through 20 mm and 0.2 mm thick stainless steel plates. The rate is normalized to secondary yield per muon per eV by dividing by the variable bin width. The thicker target generates substantially more secondaries at most energies, while the very-high-energy yield of both targets is similar. The most likely explanation for this is that the count rates at very-high energies are limited solely by the number of incident muons with these very-high-energies. These muons may decay into an electron, an anti-electron neutrino, and a muon neutrino or a corresponding set of antiparticles with equal likelihood (no dependence on target thickness). The number of gamma secondaries, not shown, is roughly 100-times higher for the 20 mm plate, corresponding to the 100-fold increase in plate thickness, with most of the gammas exiting the plate. However, the higher number of gammas induced in the thicker plate leads to a higher number of interactions with the electrons present in the stainless steel, creating more tertiary electrons. These additional electrons account for the higher secondary count rate of the thicker plate at other energies. The last bin contains all remaining events.**Bottom**: The actual rate of secondaries in the high-energy run of the SIKatrin simulation. The given rate uses an incident muon rate of 189 $/m^2$. The gaps in the secondary distribution of the wires of the inner electrode system are caused by the very low statistics available.

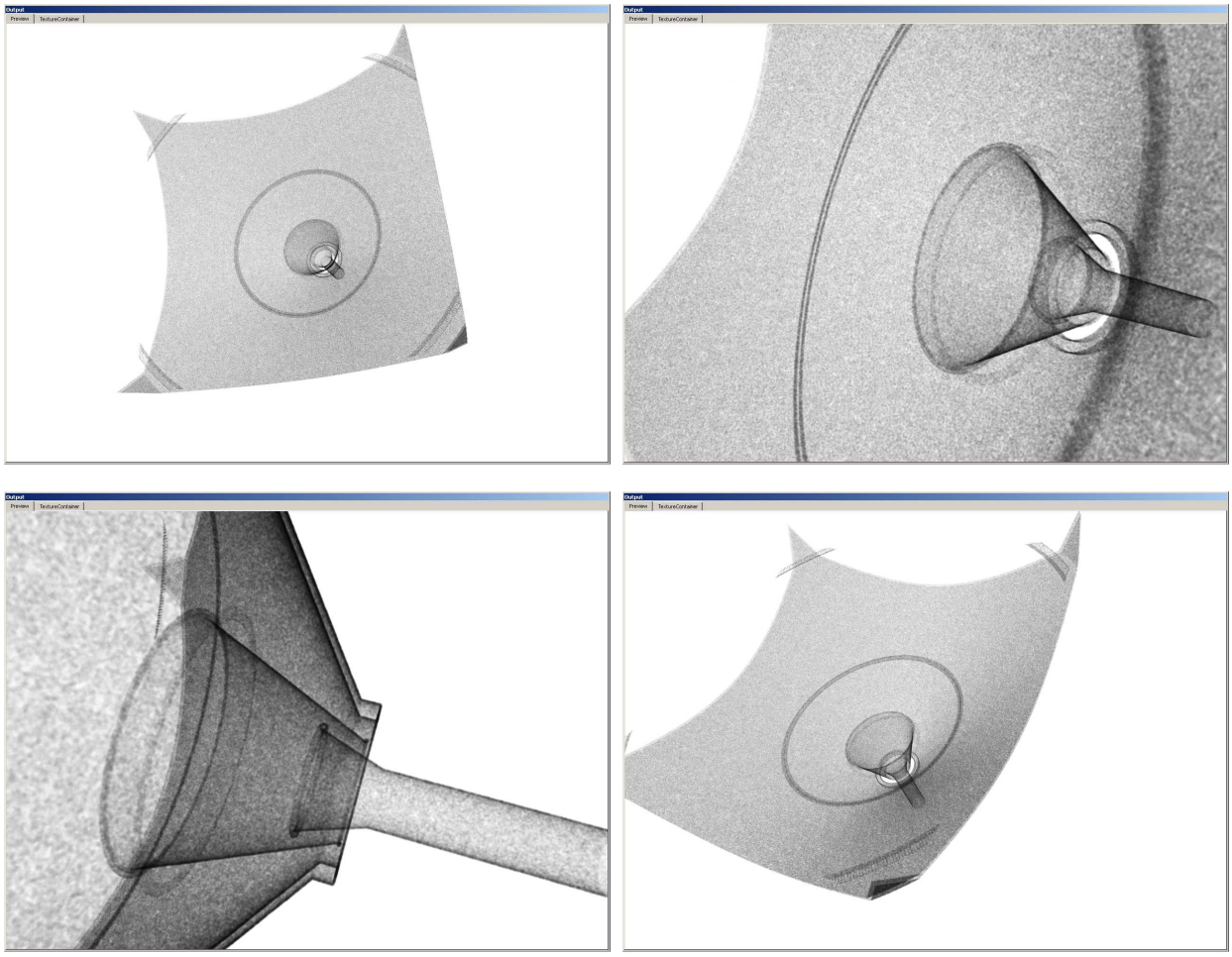

Figure 2.10.: Four views of the density map of the incident low-energy muon hits are shown; this map was generated using a mesh spacing of 2 mm and a sphere size of 3 mm to determine the local density. These images were created with VOREEN, the VOlume REndering ENgine. In the future, similar images may be generated which show the number of electrons which manage to pass by the inner electrode system, which exit the spectrometer, or the density of background electrons in the vacuum.

CHAPTER 3

DATA ANALYSIS

In order to faciliate data analysis, various software was written to aid in the analysis of the data recorded during the course of this thesis, as well as other experiments conducted by [Val09] and [Str09]. The details of these programs will be explained in the following chapter.

3.1. Data analysis - Geant4

In order to enable rapid analysis of the three-dimensional properties of data generated in the Geant4 simulations, a custom oct-bucket-tree implementation has been written which efficiently stores this data.

Binary trees are a basic data structure using nodes which contain one value (or several for bucket-based trees) as well as a pointer each to the left and right nodes; the left node contains a value which is smaller than the current node, and the right pointer would point to a node with a higher value. As more elements are added to the tree, the tree is expanded, redistributing nodes to rebalance as needed. The advantage of using such a data structure as opposed to an array is the increased access speed. Searching for a particular node can now be done in logarithmic time, vs. linear time required to traverse an array (see Fig. 3.1 for an example).

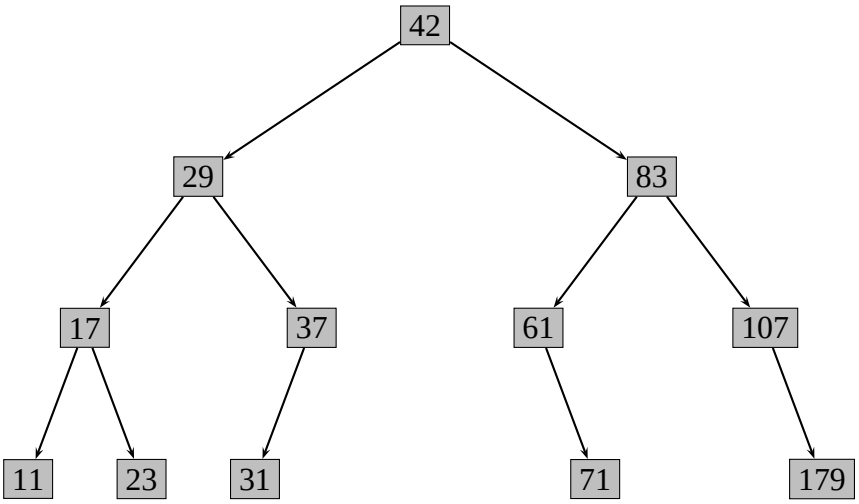

Figure 3.1.: An equalized 12-element binary tree, each node containing an integer value. A search for a node, for example the node containing 23, starts at the root node (42), and since 23 is less than 42 the search algorithm proceeds down the left branch, comparing 23 to 29, continuing down the left branch, comparing it to 17. Here, it takes the right branch, arriveing at 23 after 3 comparisons.

While a binary tree is able to store a one-dimensional dataset, the datasets with which we work are three-dimensional, requiring a more complex data structure. Therefore we opted to use a three-dimensional tree structure (Oct Tree), which allows elements to be sorted by top-forward-left, top-forward-right, ..., bottom-back-right. In addition, in order to reduce the memory overhead inherent in the nodes, as the memory required for an empty node is several times larger than the memory required to store an element, each node would store many values, dynamically lengthening its array until a maximum is reached, whereupon the elements are split out into new subnodes, which are created as required. When removing elements, the subnodes are recombined into a single master node as soon as the total element count in all subnodes reaches a lower threshold.

This allows us to pinpoint any given element or point in space in $O = \ln(N)$ time, vs $O = N$ for an unsorted array. In addition, all datapoints close to the searchpoint are contained within the found

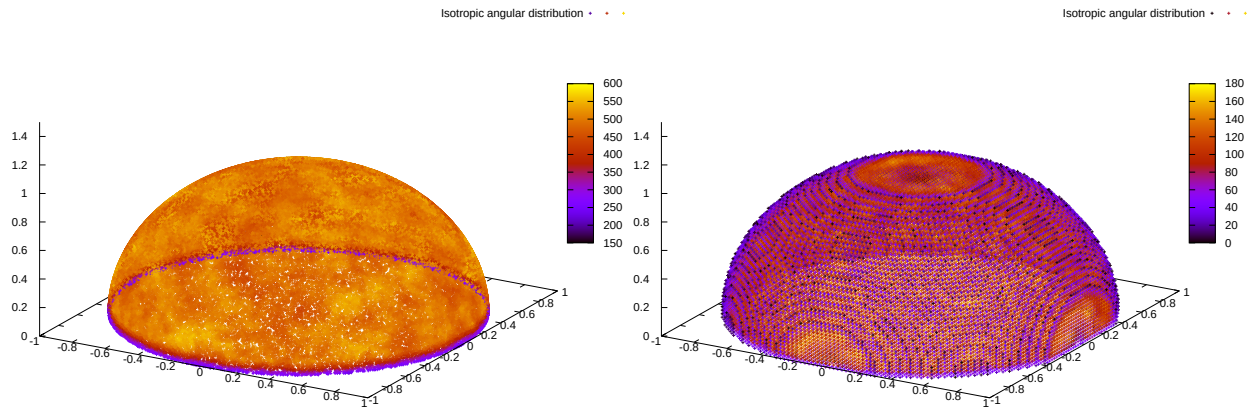

Figure 3.2.: Two example density maps using the same input data, 100k points generated by isotropic emission on a half-sphere. **Left**: The color of the data points reflects the number of data points in close vincinity (0.1 units), reflecting at the same time the gradual shift in densities and the sharp gradient when approaching the bottom of the sphere. **Right**: The densities of each point in a grid was calculated; each point of the grid is assigned the number of datapoints within a sphere of 0.02 units, with a spacing of 0.01 unit. This leads to a dense inner sphere covered with spheres with smaller densities. The higher density inner sphere is visible at each axis as the grid did not extend beyond the initial [-1:1] distribution.

node's subtree, again saving time when calculating the number of nearby points. This enables the quick calculation of electron density maps, where either the number of electrons near each electron is calculated, or a lattice is overlayed onto the total volume and the density of each point is calculated. Figure 3.2 shows the results of both of these methods when applied to an isotropic distribution with 10^5 sourcepoints, distributed onto a half-sphere.

Using this code, the calculation of the density of 2^{33} sourcepoints (a $2048 \cdot 2048 \cdot 2048$ lattice), with $2 \cdot 10^8$ datapoints loaded, was accomplished in about 80 minutes[1]. For larger lattices with much longer calculation times, the calculation can be parallelized with multiple threads, resulting in a roughly linear speed-up factor.

Currently, this program is only used to calculate the density distribution of secondary electrons entering the vacuum of the spectrometer vessel, however, in the future, it could be possible to use the tracking data generated while electrons are traversing the vacuum in combination with their energy to calculate the electron's velocity via $E = 1/2 m_e v_e^2$. Using an x/y/z map with electron weights assigned by velocity should allow the calculation of a density map of background electrons in the entire inner spectrometer.

In addition, the universal ASCII datafile analysis tools described in section 3.4 were used for the analysis of the results of the Geant4 simulations.

[1]The computer used contains two Intel E5420 processors, 16GB Ram, and runs a 64bit OS

3.2. Signal analysis

An analysis method was required to analyze the data recorded during experiments conducted at the Mainz Neutrino Mass Experiment as well as the data recorded during experiments conducted in Münster using a new Flash ADC-based data acquisition system. Since the Flash ADC system had only recently been purchased, finished analysis software did not exist, wherefore we decided to design our own. As the DAQ system was utilized in several different experiments, we decided to implement various generic analysis methods, which can then be easily adapted for each experiment.

3.2.1. Digital Signals

Detector signals are usually analyzed in one of two ways: either online using analog electronics, or by digitizing the signal and applying analysis algorithms via software or dedicated digital hardware[Kno99]. In order to digitize a signal, the voltage of the signal is repeatedly measured by an analog digital converter (ADC); the digitized values are outputted to further hardware for postsampling analysis or storage. We utilized this latter method, as we wanted to be able to utilize multiple analysis schemes optimizing the timing, energy resolution, or event detection as required by the goal of the individual experiments.

3.2.2. Flash ADC

The data acquisition system was based around the *Struck* SIS3301 and SIS3320 Flash ADCs. These Flash ADC units continuously record the signal waveform of up to eight channels in a ringbuffer. The units support hardware trigger conditions; when these are activated, the ring buffer contents are stored until read by a PC, while at the same time a new ring buffer is started in order to continue taking data. These signals were then written to an output file for later analysis and will be referred to as “waveforms“. The SIS3320 which was used in the Münster measurements has a resolution of 12 bits and a maximum sampling frequency of 200 MHz. This translates to a maximum data rate of 400 MB / channel / second, while the optical link between crate and DAQ-PC is limited to 1 Gbit (125 MB) / second, minus protocol overhead, necessitating the utilization of the hardware trigger, as opposed to continuously recording data and searching for trigger signals in the analysis.

3.2.3. Digital Filtering

All analog signals (and digitized versions thereof) have some level of noise induced by various natural and artificial causes. This noise complicates the detection of the desired signals, compared to detecting signals in perfectly noisefree waveforms. Therefore, the logical first step of any analysis algorithm is to reduce this noise, thereby increasing the signal-to-noise ratio, which allows for an easier and more exact analysis of the waveforms. Here, a digital filter was employed for this purpose.

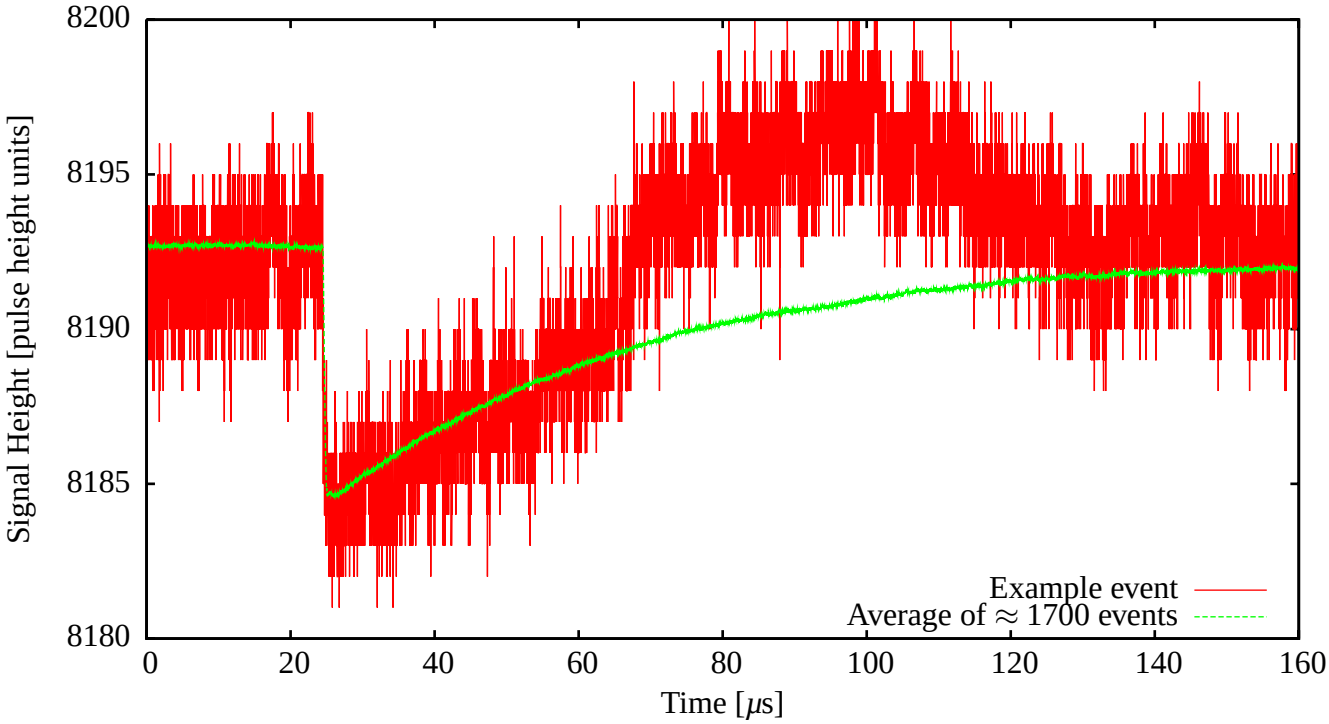

Figure 3.3.: An example event in Mainz along with the average of ≈ 1700 single-electron events. The example event exhibits some low frequency oscillations which are not present in the averaged event, as well as high frequency oscillations. The contribution due to the resolution of the Flash ADC is also visible.

Any digital filter is constrained by the finite sampling rate, which is defined by the utilized hardware. This limits the maximum frequency reconstructable from the waveforms to half the sampling frequency, as originally postulated by the Nyquist theorem.

Two classes of digital filtering algorithms exist, recursive ones such as high-pass and low-pass filters, and nonrecursive filters such as the moving average. As the name implies, nonrecursive filters directly convert a number of input values into an output value, while recursive filters also utilize previous output values. The following equation describes both classes of digital filters (for nonrecursive filters $M = 0$):

$$f(i) = y_{\mathrm{i}} = \sum_{n=0}^{N} c_{\mathrm{n}} \cdot x_{\mathrm{i\text{-}N+n}} + \sum_{m=0}^{M} d_{\mathrm{m}} \cdot y_{\mathrm{i\text{-}(M+1)+m}} \tag{3.1}$$

Here, $f(i)$ would be the filtered value, using N input values x_{i} as well as the M previously filtered values y_{i}. The coefficients c_{n} and d_{m} vary depending on the type of filter being applied; for example a running average would have all $c_{\mathrm{n}} = 1$ and $M = 0$.

3.2.4. Analysis of the Mainz data

In Mainz, the Flash ADC-based DAQ system was used to record the preamplifier signals of the silicon PIN diode in order to enable a very high energy and, more importantly, timing resolution;

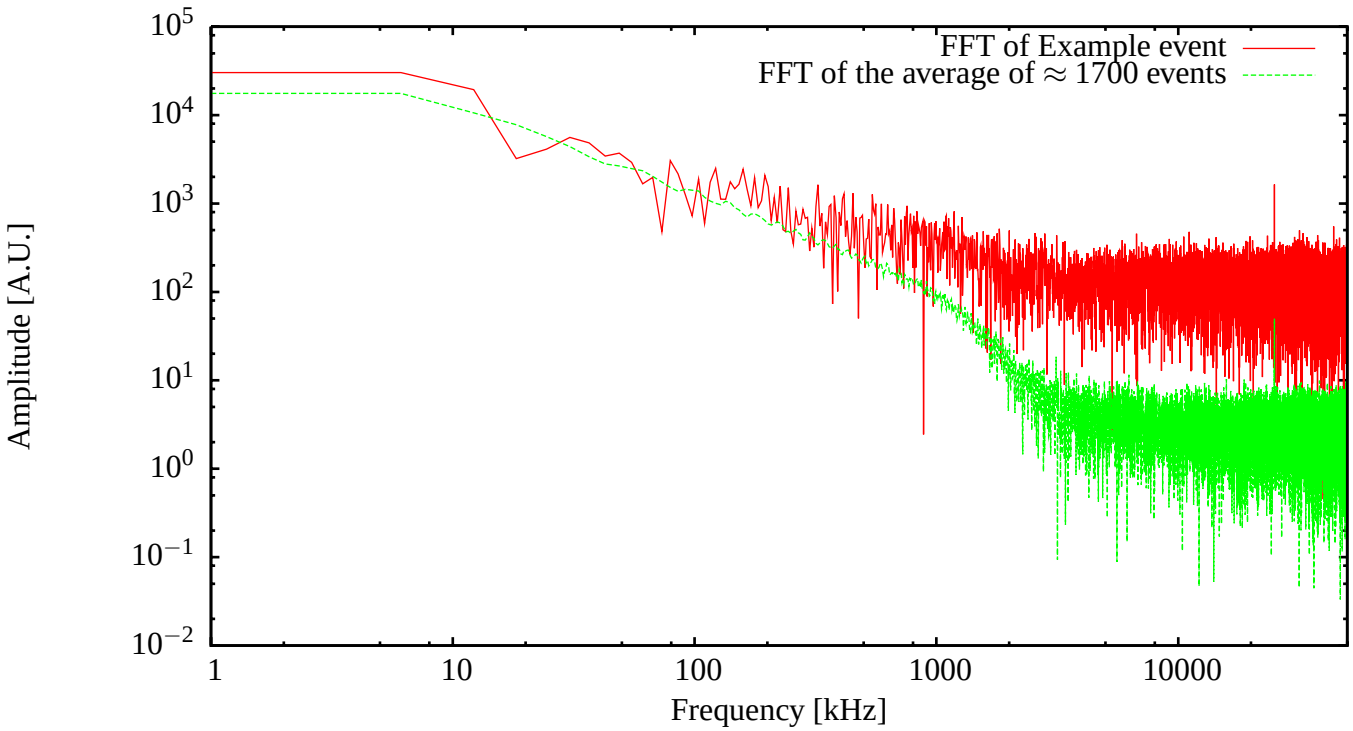

Figure 3.4.: The fourier transformation of both a sample event and the averaged "ideal" event, previously shown in Fig. 3.3. Noise dominates above 1MHz, below this value the two transformations differ, as the event peak dominates these frequencies.

an example single-electron event along with an idealized event constructed by averaging many events (for details see [Str09]) is shown in Fig. 3.3. First, we needed to reduce the noisiness of these recorded waveforms. For this we utilized a bandpass filter to remove low-frequency noise which gradually shifted the signal baseline, as well to remove the very-high-frequency noise which interfered in the separation of multiple closely spaced events. The boundary frequencies of the filter were determined by generating the fourier transformations of a noise sample and an averaged event (see Fig. 3.4). After selecting starting values for the filter frequencies, we then filtered several sample events with slight variations of these frequencies. By modifying the border frequencies, we could eliminate several noise components and manipulate the smoothness as well as the steepness of the resulting signals. As we needed to be able to identify events which followed in quick succession, we used a high upper frequency, which resulted in a steep signal. Lastly, we analyzed the data of a sample measurement with different filter frequencies in order to determine how the resulting energy resolution changed with the filter frequencies, and finally settled on a lower frequency of 1 kHz which would smooth our baseline by removing slow variations, which were a large contribution to the loss of energy resolution. We set an upper frequency of 1 MHz. Higher upper frequncy cutoffs led to such an increase in noise that event identification became problematic; it also led to a reduced energy resolution in the resulting spectrum. One reason why the energy resolution was so dependent on our frequencies was because modifying these frequencies would induce upswings before the actual signals, the strength of which varied widely and which then falsified the resulting differential spectrum. In order to illustrate these effects, the resulting waveform of a multiple electron event, filtered with different frequency combinations, is shown in Fig. 3.5.

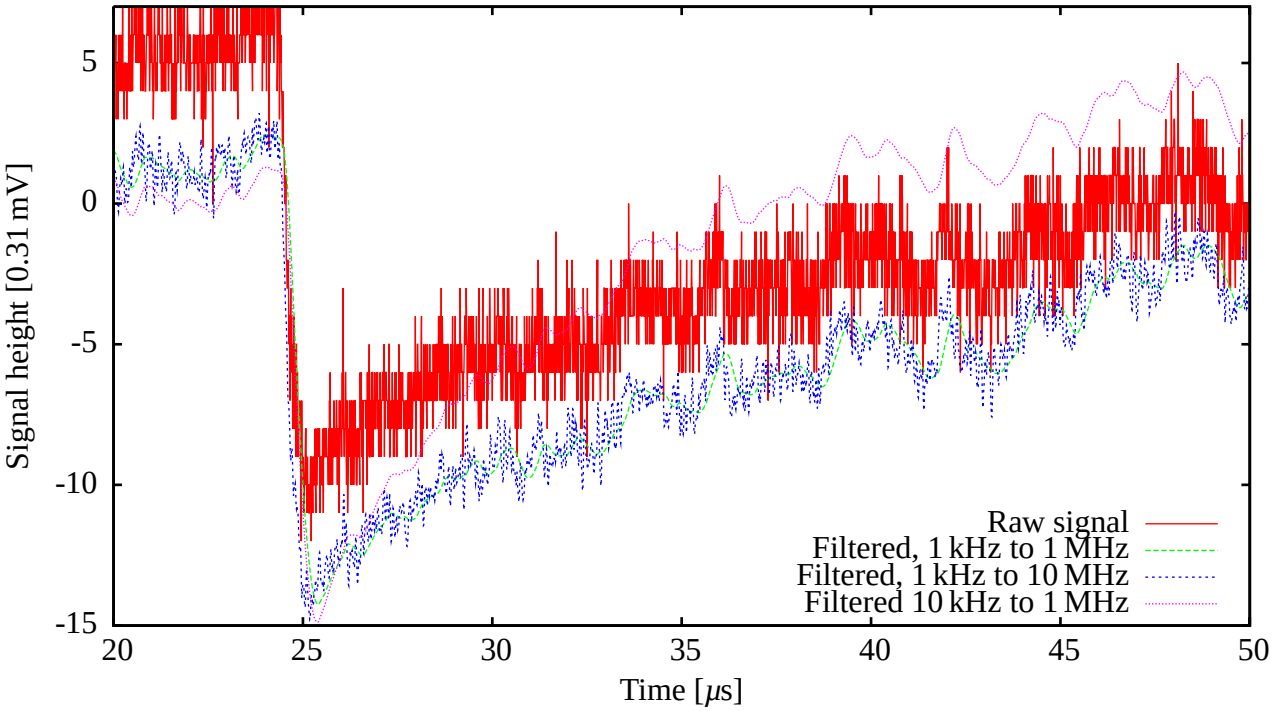

Figure 3.5.: Sample Mainz event filtered with various sets of cut-off frequencies. The reduction in noise is very noticible, as well as the dependence of the noise reduction on the choice of frequencies, with a large amount of noise still visible when using an upper filter cutoff of 10 MHz.

After filtering the waveforms, these are differentiated and a ROOT[Bru97]-based peaksearch algorithm developed by [Str09] is applied for event identification.

3.3. AnalyzeV8

A program for the analysis of the raw data produced by our DAQ system (.eve files) was written, which is currently in the eighth iteration (AnalyzeV8). The program allows the user to define a chain of analysis steps which will then be applied to each event in the dataset. As each event may contain the recorded waveforms of multiple channels, each analysis step can be applied to any subset of channels.

This program was used to analyze the data recorded during measurements in Mainz by Kathrin Valerius [Val09] and Sebastian Streubel[Str09], as well as for the analysis of the muon measurements conducted in Münster (described in chapter 4 and 5), and is intended for an easy analysis of all future experiments conducted with the Flash ADC system.

The program needs to be given the name of a rawdata file or set of files as the first parameter, as well as the number of channels for the older SIS3301 formatted files. For newer versions of the Flash ADC readout software, the channel count should be automatically detected.

3.3.1. Capabilities

The various analytical operations which can be utilized to manipulate the stored waveforms will be described in the following subsections. In addition to these, several other functions are available, such as storing the events in a text file or removing a specific waveform or even all waveforms of a channel. These latter functions will not be elaborated upon. The resulting analysis chain can be saved to a file for quick reuse in the analysis of further measurements.

Furthermore, the analysis can also be limited to specific events or event ranges: alternatively, specific events or event ranges can be excluded.

3.3.2. Rebinning

The various waveforms can be rebinned by any factor, which effectively decreases the sampling frequency. This averages all values of each bin, thereby reducing the Flash ADC's intrinsic noise, which would remain the same if the actual sampling frequency was reduced by an identical factor.

$$f'(x) = \frac{1}{N} \sum_{i=0}^{N} f(N \cdot x + i) \tag{3.2}$$

3.3.3. Running Average

It is possible to calculate a running average of any waveform loaded or generated by previously applied steps. The edges of the waveform are folded back onto themselves when calculating this average, i.e. $f(-x) = f(x)$; a possible alternative running average implementation was dismissed as it would have resulted in a waveform shortened by the smoothing width. The passed width N should be an odd number. This is also the only implemented digital filter with a calculation time independent of the smoothing width. Figure 3.6 shows the results of a running average on various functions.

$$f(x) = \frac{1}{N} \sum_{i=-\frac{N-1}{2}}^{\frac{N-1}{2}} f(x+i) \tag{3.3}$$

3.3.4. Weighted Average

Another averaging algorithm available is a weighted average utilizing the following weight function:

$$w(i) = \frac{1}{|i/2| + 1} \tag{3.4}$$

This results in the following averaging function:

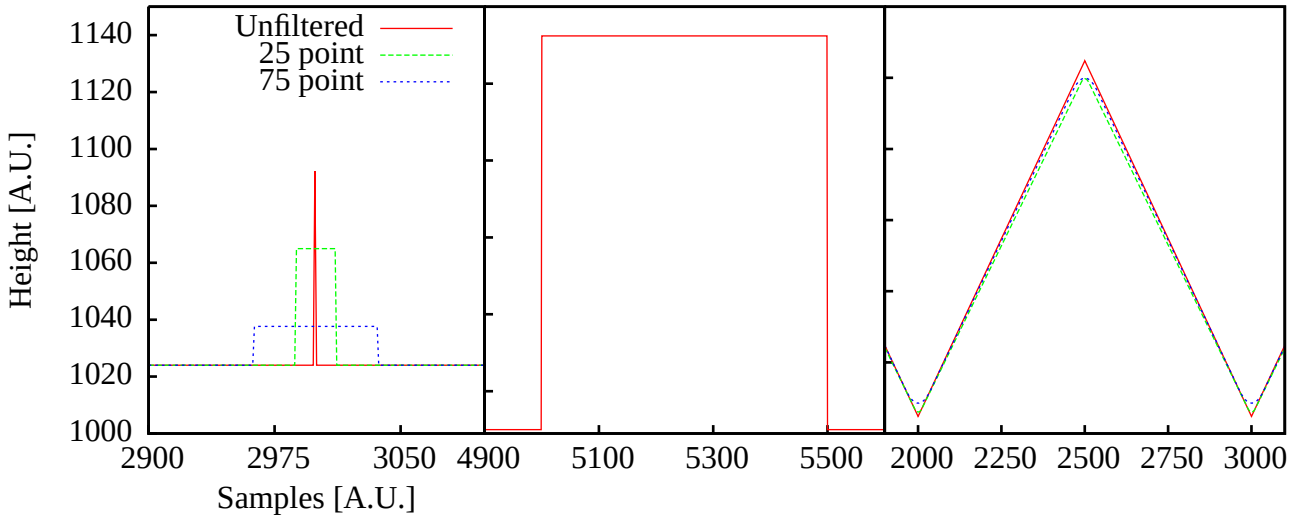

Figure 3.6.: The effects of a running average on a delta peak, square wave, and triangular wave. The original pulse height of the delta peak has been renormalized. The smoothing of the delta peak results in a rectangular pulse, while the smoothing of the rectangular pulse results in a linear increase and decrease along the edges.

$$f(x) = \frac{1}{N} \sum_{i=-\frac{N-1}{2}}^{\frac{N-1}{2}} w(i) f(x+i) \tag{3.5}$$

The weighting results in a bias, therefore edges such as those in a square wave are not affected as harshly as with a running average, and sudden changes no longer result in steps, as can be seen when comparing the effects on a weighted average on a delta peak (see Fig. 3.7) vs a running average (see Fig. 3.6).

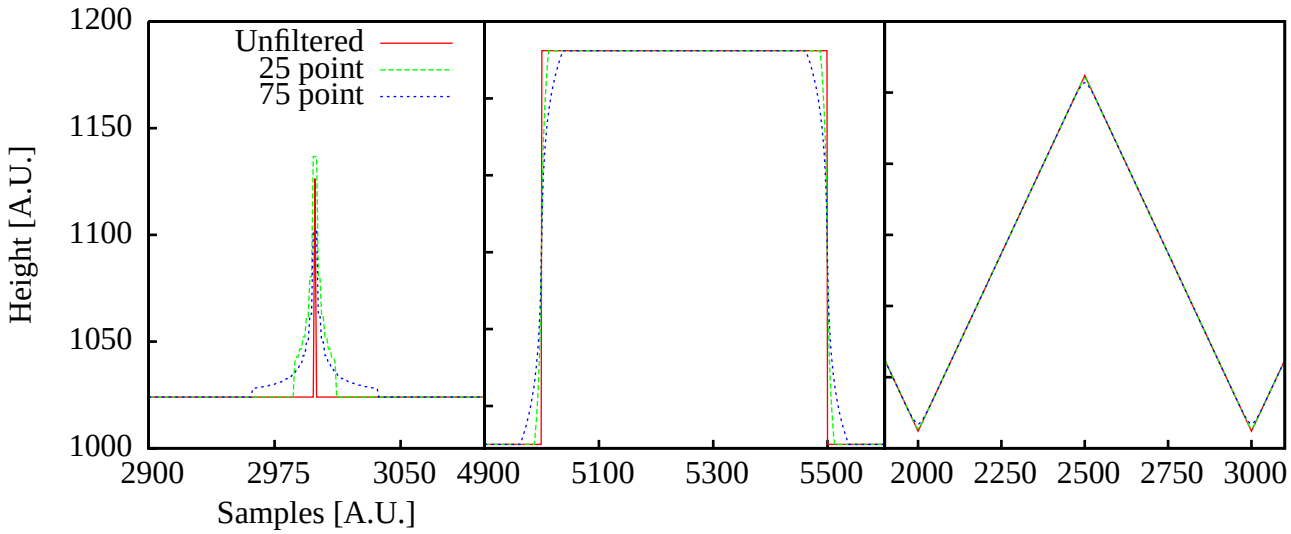

Figure 3.7.: The effects of a weighted running average on a delta peak, square wave, and triangular wave. The original pulse height of the delta peak has been renormalized. The resulting functions gradually transition to the new height, with no abrupt changes visible, also resulting in a smoother differential.

3.3.5. Bandpass Filtering

Additionally, a bandpass filter was included in AnalyzeV8. This function implements a Butterworth band-pass (BWBP) filter [Exstrom] for the coefficient calculation. The lower and upper frequencies as well as the sampling frequency must be provided, along with the order of the filter, in order to calculate these coefficients. However, filters higher than second order often diverge to infinity due to numerical instabilities when utilizing the long double type (80 bits). An arbitrary precision filter is accessible via a compiler flag: however, this runs many times more slowly, and may also diverge. Figure 3.8 shows the effects of filtering on the sum of three sine waves.

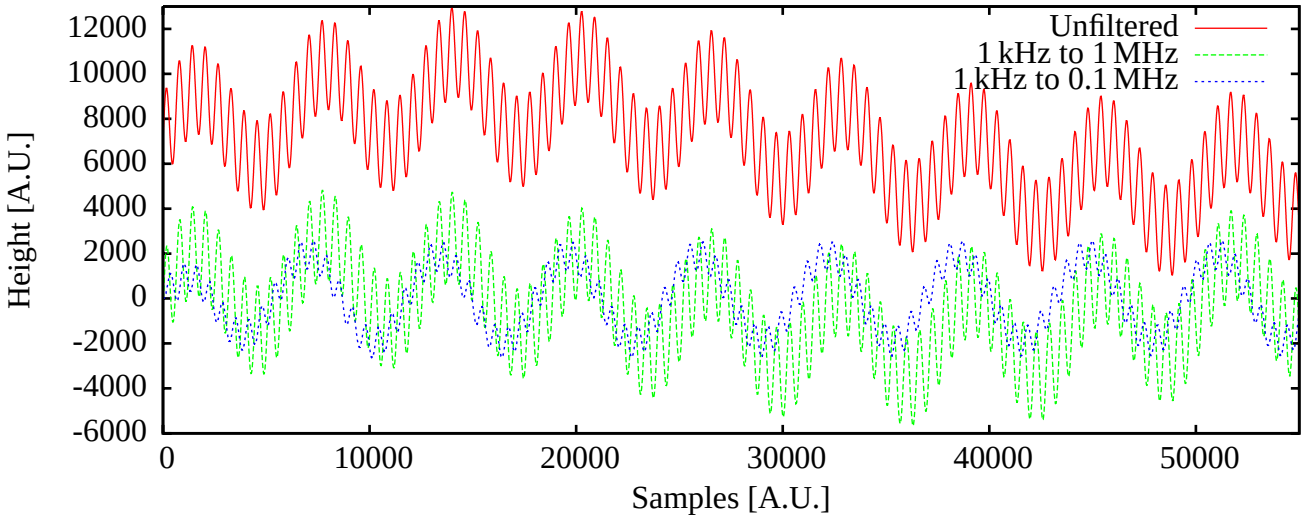

Figure 3.8.: The effects of a digital filter on a sum of three sine waves of varying frequencies. With a sufficiently low upper frequency, the sine wave with the lowest frequency can be fully eliminated from the recorded waveform, as is demonstrated with the filter frequencies of 1 kHz to 0.1 MHz, using 100 MHz as the sampling frequency.

The BWBP coefficient calculation class instance could easily be replaced with a low-pass or high-pass filter implementation, if required.

3.3.6. Differentiation

It is also possible to generate the differential of a waveform with variable widths. Using a width of one is the classic differential of a function, as shown in Fig. 3.9, while increasing the width allows us to detect steps with limited resolution. This last method was utilized while searching for peaks in noise while commissioning the vacuum chamber, using the minimum width of an event flank for the step width and the minimum height as the trigger conditions. The hardware trigger of some Flash ADCs works in a similar fashion, searching for minimal differences between two aggregated values.

$$f'(x,N) = f(x) - f(x-N) \tag{3.6}$$

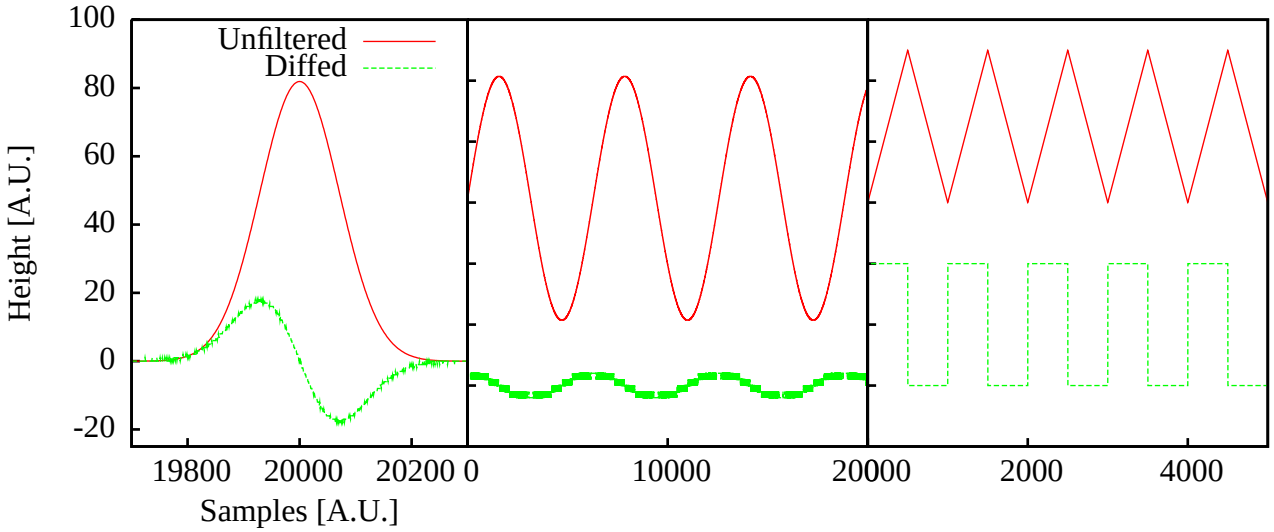

Figure 3.9.: Results of the differentiation of a gauss, sine, and triangle wave. The original waveforms are rescaled. As the input files generated by the Flash ADCs utilize unsigned shorts, as opposed to floating point numbers, the input ideal waveforms contain some artifacts due to rounding, which propagated to the differentiated waveforms.

3.3.7. Peak search

In order to locate peaks in the data recorded during our measurements, a peak-search algorithm was implemented. This algorithm optionally subtracts a fixed offset (O) from the waveform which can be used in order to compensate for a non-zero baseline. Then the algorithm iterates through the individual points of the waveform, checking for sign changes and in this way locating points where $sgn(f(x_n) - O)! = sgn(f(x_{n-1}) - O)$. While doing this, it also sums the values of every point since the last crossing of the offset line, as well as stores the maximum height found. The event index as well as the event starting time are saved, along with the peak data, which includes the start, stop, and maximum point indexes of the current located peak. This typically results in a very high number of located peaks, as the background noise usually causes many crossings of the baseline. The resulting files may then be filtered in order to remove this noise, for example by removing all peaks under a certain minimal height. The additional programs which were created for this purpose are described in section 3.4. An example of a located peak is shown in fig. 3.10.

The output files contain the data of a located peak per line, formatted as: [Event Index] [Event Time] [Peak start] [Peak start(2)[2]] [Peak maximum] [Peak end] [Peak Height] [Peak Area] [FWHM[3]].

3.3.8. Example usage

Listing 3.1 shows the output of AnalyzeV8 when setting up the analysis chain as used in Mainz. This chain first smoothed the data using a second-order BWBP filter with cut-off frequencies of 1 kHz to 1 MHz, subsequently differentiated the resulting waveform, and saved the events to text

[2] Deprecated
[3] Calcuation of FWHM was disabled at the time of this writting.

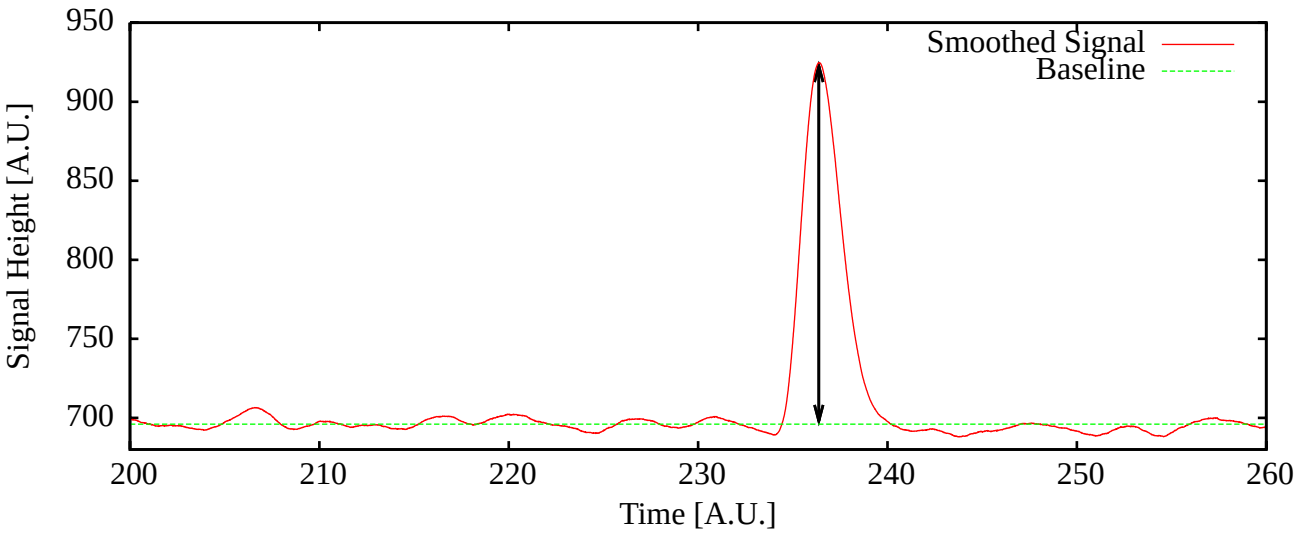

Figure 3.10.: Example of a located signal in a waveform, along with the reference baseline. Other located peaks are not marked as such.

files. The events were then removed from memory as they were no longer needed significantly reducing total memory usage.

Listing 3.1: Setting up the analysis chain to analyze Mainz data using AnalyzeV8.

```
 > ./AnalyzeV8 ExampleFilename 5
##       Preparing to load file: ExampleFilename
##       Number of channels set to: 5

============================================================
Choose an action to add to the action list.
        1:      Smoothing with weighted average
        2:      Smoothing with normal average
        3:      Digital smoothing
        16:     Rebin spectrum
        32:     Remove event if nothing interesting is found. (NOT IMPLEMENTED)
        48:     Save event to file
        64:     Create differential spectrum
        80:     Delete event.
        96:     Analyse digital smoothed spectum for events.
        97:     Analyse differential spectrum of digital smoothed spectum for events.
        98:     Analyze analog waveform for unipolar peaks.
        99:     Analyze analog waveform for bipolar peaks.(NOT IMPLEMENTED)

        0:      Done setting up analysis chain.
        1000:   Delete current chain
        1001:   Show current chain
        1002:   Edit event filtering

        2001:   Save current chain
        2002:   Load analysis chain

============================================================

Enter action to add to analysis chain: 3
Enter channel # (#1->1, #2->2, #3->4, #4->8): 1
Enter sampling frequency: 100000000
Enter lower frequency: 1000
Enter upper frequency: 1000000
Enter filter order: 2
Enter name of spectrum to use as input data: Raw
Enter name for resulting spectrum: Digital

============================================================
Choose an action to add to the action list.
(...)
============================================================

Enter action to add to analysis chain: 64
Enter channel # (#1->1, #2->2, #3->4, #4->8): 1
Enter number of bins to summerize while diffing: 1
Enter name of spectrum to use as input data: Digital
Enter name for resulting spectrum: Diffed

============================================================
Choose an action to add to the action list.
(...)
============================================================

Enter action to add to analysis chain: 48
Enter base filename: Results
Only dump events which are deamed interesting? (y/n)n

============================================================
Choose an action to add to the action list.
(...)
============================================================


Enter action to add to analysis chain: 80

============================================================
Choose an action to add to the action list.
(...)
============================================================


Enter action to add to analysis chain: 0
##       Preparing to load file: ExampleFilename
##       Number of channels set to: 5
Bufsize is: 1048576, version is: 256 0x00000100
Running action node    2 on event  0
```

The analysis of the muon data recorded in Münster was done with a 25 point running average, and a subsequent application of the peaksearch algorithm.

3.3.9. Possible future improvements

While many improvements were made to AnalyzeV8 during the refinement of our data analysis scheme, the modularity of the analysis methods may be further improved by utilizing an abstract base class for waveform manipulation functions and subclassing this class for every desired method.

Additionally, for use in real-time data analysis where the analysis chain is too CPU-intensive for the PC recording the data, the unfinished network functionality can be completed, to interactively send the recorded waveforms to any number of client analysis systems, which will then return the results for utilization in the real-time display.

3.4. Miscellaneous Programs

Several small applications were written for an easy manipulation of the output created by AnalyzeV8 as well as the output of some simulations. Some of these programs could have been integrated into AnalyzeV8; however, this was not done as changing minor settings in this step of the analysis process would require rerunning AnalyzeV8 and restarting the entire analysis chain, involving the loading of many gigabytes of raw data files and rerunning lengthy algorithms, while rerunning postprocessing analysis on the outputted files can be done very quickly.

3.4.1. FilterByValue

FilterByValue reads any ASCII datafile with multiple columes, and removes lines where the value of the set colume does not meet the set minimum or maximum value criteria. This was used to filter the resulting file outputted by a peaksearch done with AnalysisV8, e.g., to remove noise peaks or a the pulser peak.

Usage is: Filter [infile] [outfile] [column] [value] [0: min; 1: max]

3.4.2. BinScatter

BinScatter creates a binned spectrum of an input file, for example an energy spectrum or a time spectrum. The output spectrum is of the format: [Lower binedge] [Upper binedge] [Value].

Usage is: Binner [infile] [outfile] [number columes] [column to bin] [min value] [max value] [bin size]

3.4.3. Rebin

Rebin takes a binned input spectrum and rebins it. Factor is the number of bins which are summed for each output bin.

Usage is: Rebin [infile] [outfile] [factor]

3.4.4. CalcRadius

Written in order to analyze the output files of radially symmetrical simulations, this program takes a file containing X and Y columns, and appends an R column to the end of each line.

Usage is: CalcRadius [infile] [outfile] [X column] [Y column]

3.4.5. GenTransmission

This program generates a binned transmission function of an input file which contains columns for whether an event was transmitted, and the differentiator of this event, e.g. the starting radius, or starting energy.

Usage is: GenTransmission [infile] [outfile] [column with transmission] [col with value] [min value] [max value] [bin size]

CHAPTER 4

DESIGN AND SETUP OF THE MÜNSTER MUON EXPERIMENT.

In order to obtain a better understanding of the causes of the expected electron background in the main spectrometer of the KATRIN Experiment, an experiment was conducted to measure the low-energy secondary electrons ejected from stainless steel by cosmic muons. The resulting e^- yield was then utilized in our simulations. This chapter describes the design and set up of a high voltage vacuum test-stand which was then utilized for this and other experiments.

4.1. Motivation

In order to accurately simulate the electron background expected in the KATRIN Experiment, precise knowledge of the low-energy secondary electron yield induced by cosmic muons as well as the energy spectrum of these electrons is essential. Therefore, we attempted the spectroscopy of the low-energy secondary electrons created by cosmic muons using the spectrometer of the Mainz Neutrino Mass Experiment. Data taken by [Sch04] during background studies suggested a secondary rate on the order of $1\,e^-$ per incident muon[1]. These measurements had utilized large muon paddles above and below the electron spectrometer of the Mainz Neutrino Mass Experiment; therefore being sensitive to secondary electrons ejected over a large portion of the inner surface of the spectrometer. This also resulted in the detected muons passing through two surfaces, once at the top of the spectrometer, and again when exiting it.

The muon-induced secondary electron spectroscopy measurements presented in the following chapters used the same spectrometer at Mainz, along with an isolator vacuum tube with a blind flange on one end. The blind flange was attached to a HV supply to function as the source of muon-induced secondary electrons. In addition, two small muon paddles (active size: 100 mm x 70 mm) were set up in parallel behind this flange which detect incoming muons. A Flash ADC recorded the preamplifier signals of the silicon PIN diode whenever both muon paddles triggered. Figure 4.2 shows a schematic overview of the Mainz setup, and Fig. 4.1 shows photos of the setup.

While these measurements had a high background electron count rate due to discharges from the electrode, this background is uniformly distributed in time. The expected muon-electron coincidence events occur shortly after the muon trigger, which is used as the zero point in the electron arrival time spectrum. Therefore all secondary electrons created by the detected incoming muons are expected to be detected in a window shortly after the muon coincidence signal occurs, leading to a peak in the electron arrival time spectrum shortly after the muon coincidence time. However, after analyzing the recorded data, no excess coincidences were found.

This led us to conclude that the secondary electron yield is significantly lower than our initial expectations; therefore we decided to determine the cumulative low-energy electron yield experimentally using a dedicated setup at the University of Münster, forgoing a determination of the energy spectrum. While the cumulative nature of the resulting yield factor allows the determination of the number of secondary electrons created in the KATRIN main spectrometer (see section 2.4), without knowledge of the energy distribution it is not possible to determine the effectiveness of the inner electrode system.

For this, an experiment was designed and set up in Münster using the same isolator flange and electrode in order to either verify the low secondary electron count rate or to determine the cause of the low count rate. Additionally, a decision was made to vary the positions of the muon paddles

[1] A muon coincidence rate of 27.2 ± 0.2 Hz was measured in the utilized muon paddles, as well as a detected muon-electron coincidence rate of 30.65 ± 0.43 mHz. Correcting for the estimated background reduction factor due to the electromagnetic field configuration results in secondary electron yield of about $1\,e^-$ per muon.

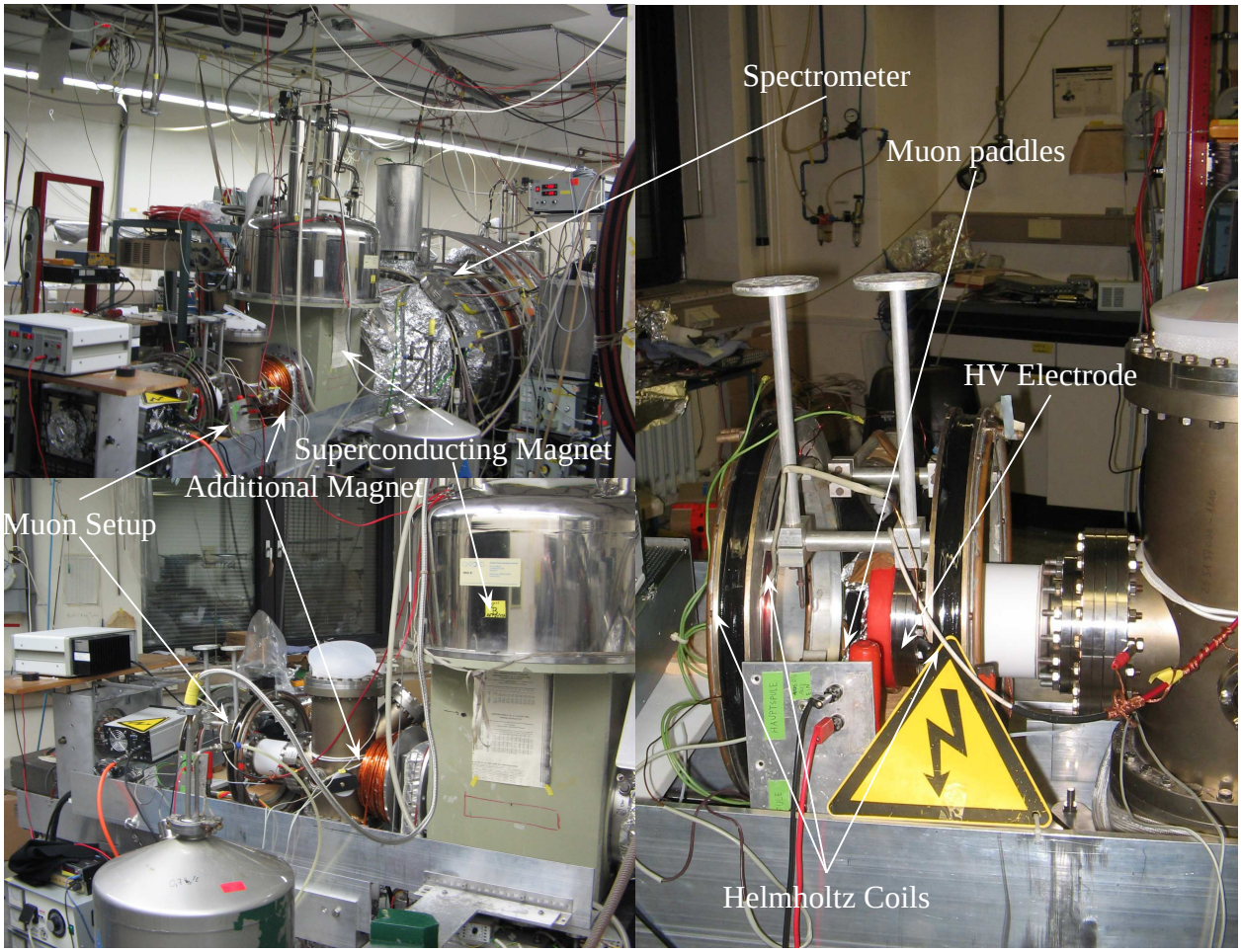

Figure 4.1.: The setup used during the measurements in Mainz. **Top left**: The Mainz Neutrino Mass Experiment as viewed from the left side of the laboratory (source side). **Bottom left**: An overview of the Helmholtz coils surrounding the muon paddles and source electrode, as well as the additional magnet. **Right**: Closeup view of the muon setup with the isolator, muon paddles and electrode visible.

in order to determine whether the secondary electron rate is dependent on the incident angle of the primary muon.

4.2. Münster vacuum test chamber

The first step was to design and build a suitable vacuum setup in Münster. This setup was planned as a long-term setup for various smaller experiments, with the muon measurements conducted first; in the meantime the electron emission rate of wires in the conus modules of the wire electrode was measured by [Zac09], and a second measurement of emission rates is in planning.

The experimental setup utilizes a CF100 flange on a high negative voltage as an electron source. Muons passing through the electrode eject low-energy secondary electrons, which are accelerated towards the detector, thus ensuring the energy deposition in the detector is sufficiently large to detect single electron events. This electrode is isolated from the rest of the setup by an isolator

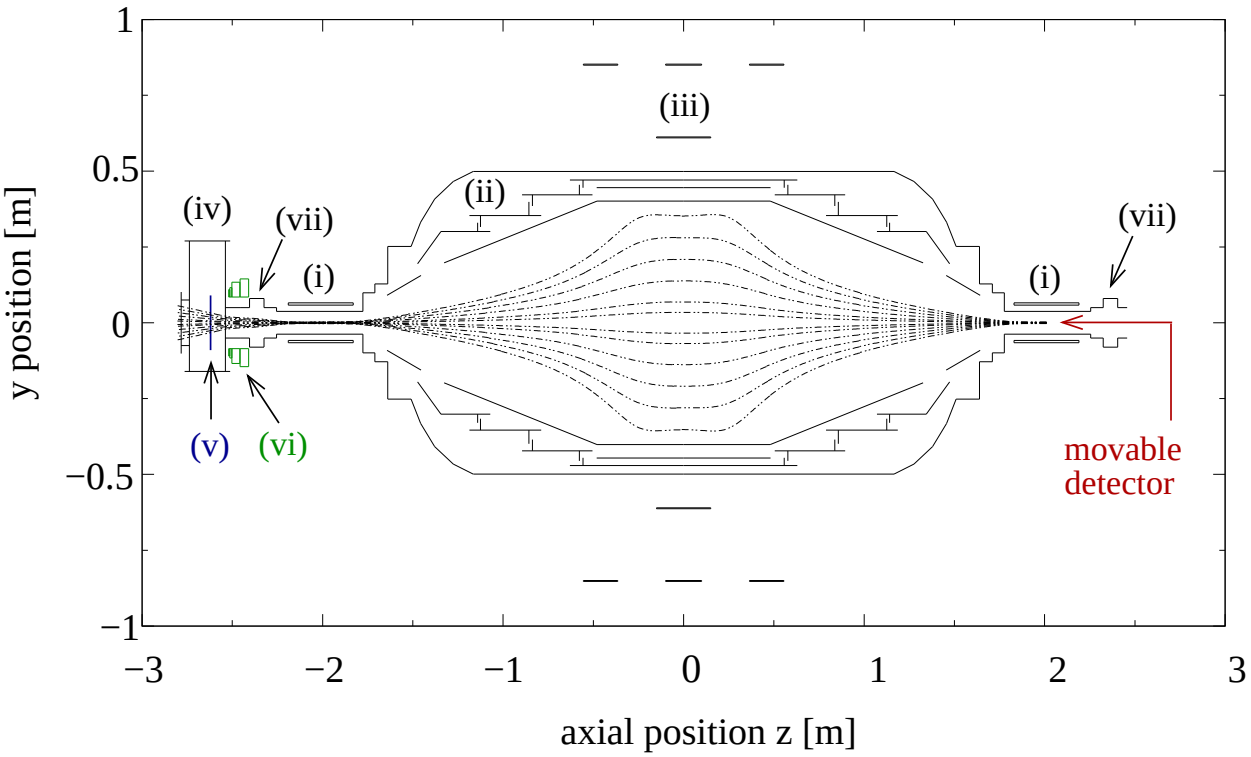

Figure 4.2.: Setup used at the Mainz Neutrino Mass Experiment to detect secondary electrons ejected by cosmic muons: (i) superconducting coils, (ii) electrode system consisting of vacuum tank at ground potential, solid and wire inner electrode systems, (iii) field-shaping air coils, (iv) vacuum chamber to which the isolator flange was attached, (v) the backplate electrode used during later muon runs, (vi) water-cooled additional coil for local enhancement of the magnetic field near the electron ejection site, (vii) valves. The detector is situated on a movable sleigh close to the solenoid on the right-hand side. Magnetic field lines (settings corresponding to a resolving power of $E/\Delta E \approx 2 \cdot 10^4$) are indicated as dashed curves. The muon paddles are not shown.
This figure is taken from [Val09], where further details of the spectrometer setup may be found.

tube. In order to determine whether a detected electron was caused by a cosmic muon, muon paddles were placed close to this electrode, and data acquisition was triggered by the detected muon coincidence events. A square silicon PIN diode detector was used to detect the electrons ejected from the electrode, with the magnetic field guiding these to the detector, ensuring electrons originating from a large area of the electrode arrive at the detector. The final design is shown in Fig. 4.3.

The primary goal of the setup design is maximizing the count rate of the secondary electrons. As data is only being recorded during muon coincidence events, this count rate is primarily determined by the number of detected muon coincidences and the probability that such a coincidence leads to detectable secondary electrons. The muon coincidence rate is determined by the size and position of the muon paddles; this rate is directly related to the distance between the two paddles and the angle between them, as the cosmic muon flux is strongly angularly dependent (see section 1.4.3 for details). However, placing the paddles close together in order to maximize the coincidence rate would result in a very high number of false positives, i.e. triggers which are caused by muons

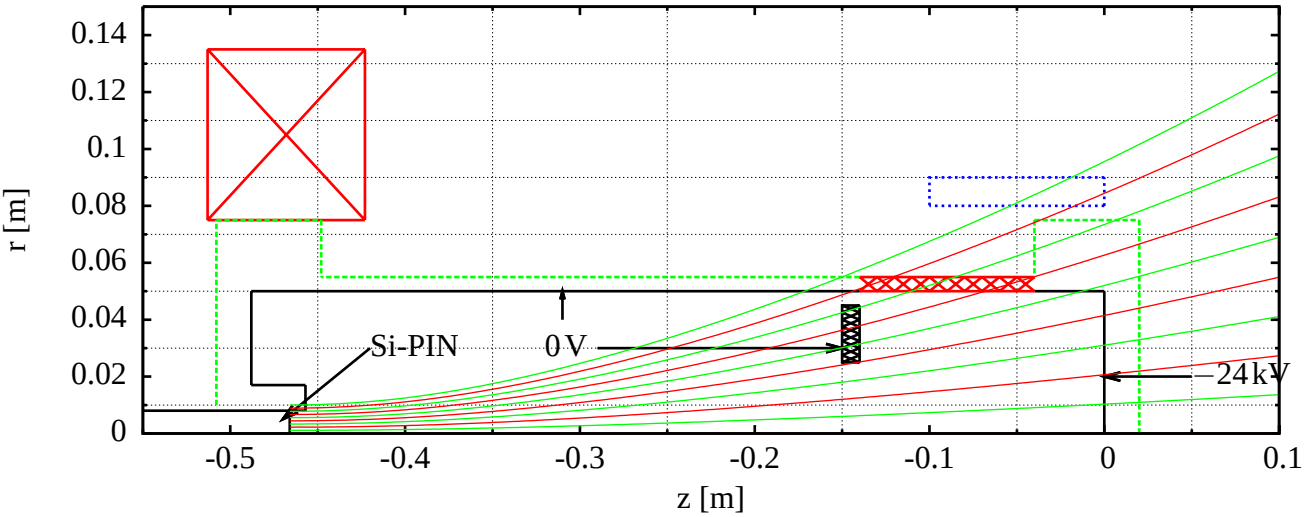

Figure 4.3.: Schematic overview of the vacuum chamber. The green outline shows the outer surface of the vacuum chamber, disregarding the additional openings of the crosspiece. The inner surfaces are shown in black, with the detector housing on the left. The additional surfaces around the detector are parts of the initial detector housing; this detector was later replaced with a housingless detector. The grounding electrode, which smooths the electric field inside of the isolator, is visible near $z = -0.15\,\mathrm{m}$. The extent of the ceramic isolator is shown on the right, in red. The magnetic coil is visible on the left, in red, with the magnetic field lines shown in red and green. One of the muon paddles is visible above the HV-electrode, in blue.

which do not pass through the HV-electrode, resulting in an increased signal-to-background ratio. As a very low coincidence signal could not be ruled out in the Mainz experiment due to the high background electron rate, minimizing the electron background was of high priority. Therefore, a balance must be struck between maximizing the probability of an electrode hit, which increases with the distance between the detectors, and maximizing the trigger rate, which decreases with this distance.

A second independent method of increasing the likelihood of detecting secondary electrons is to increase the surface area of the electrode visible to the detector. Assuming that each point on the electrode surface may be reached with equal likelihood by a coincidence muon[2], the secondary electron count rate is linearly dependent on the visible area.

Ideally, the flightpath of electrons leaving the electrode consists of a linear acceleration, a subsequent focussing, and a further linear path to the detector. Additionally, this flightpath would impart as little cyclotron energy to the electrons as possible, ensuring that some electrons ejected near the edge of the visible area are not cut off due to them flying past the detector when on the outer portion of their cyclotron track, as well as preventing magnetic reflection of the electrons before reaching the detector. A large magnetic coil was available, which produces a maximum field of 0.1 T, along with a set of helmholtz coils which can generate a 50 G field, which we intended to use in order to approximate this flightpath.

It was decided to use a ring electrode flush with the inner end of the isolator (shown in Fig. 4.4) to define the ground of the electric field of the HV-electrode. The total length of the flightpath

[2]The actual distribution is dependent on the muon paddle configuration

was determined by the length of the available vacuum chamber and isolator, with the possibility of adding an additional 300-mm-long CF100 tube. Several test setups were designed, and calculations of the magnetic field lines as well as basic tracking simulations using the eltraj program (see section 1.6 for details of eltraj) were run, in order to refine these designs. While initially it was attempted to have the magnetic field at the HV-electrode parallel to the axis (as shown in Fig. 4.5), we noted an increase in the cyclotron radius with these designs[3]. In order to reduce the cyclotron motion, the magnetic field needs to diverge at the electrode, thus aligning itself with the electric field lines, minimizing the cyclotron energy of the electron. This resulted in the final design shown in Fig. 4.3.

Figure 4.4.: Top left: The ring electrode which grounds the electric field and ensures a smooth field, before mounting in the isolator flange. **Top right**: View of the interior of the vacuum chamber cross piece. The detector is visible in the back. **Bottom left**: View of the vacuum chamber along the z-axis with the isolator tube attached. The electrode is visible in the isolator section. **Bottom right**: View of the isolator with the PVC endcap mounted, the red line denotes the inner extent of the electrode. Also visible are the HV-capacitors for the voltage smoothing.

Initially, the setup was planned with the main beam tube oriented vertically with the isolator and HV-electrode at the top, and the detector at the bottom of the setup, in order to take advantage of the increased incident muon count rate at steep zenith angles. However, this turned out to be very impractical because it would require the turbopump to be attached horizontally, as well as limiting

[3]For an explanation of this effect see [Hei09].

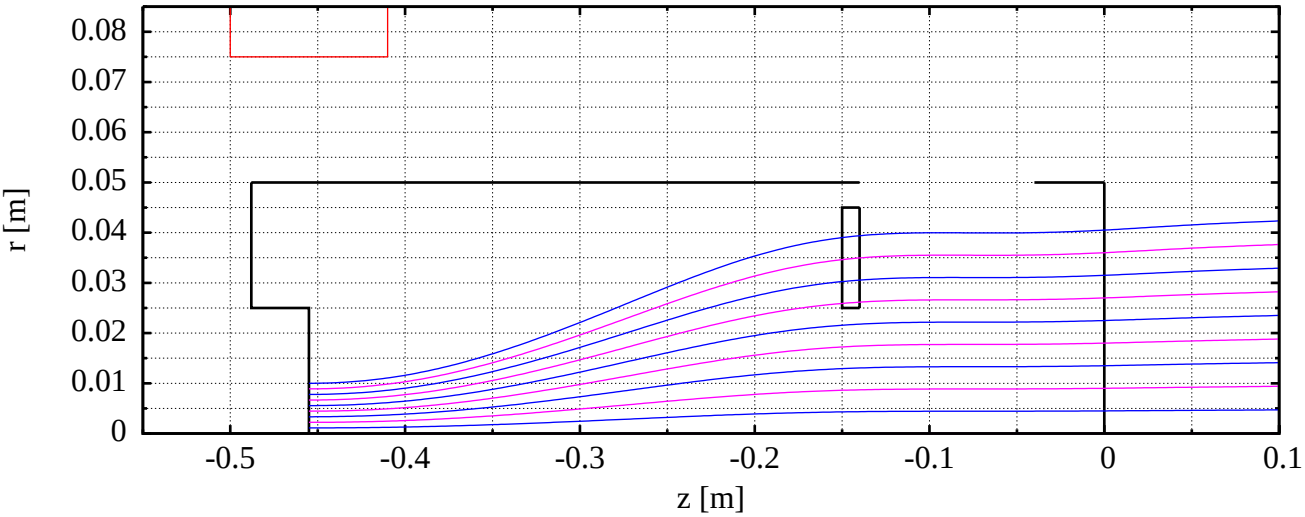

Figure 4.5.: Magnetic field lines while attempting to create an axial field at the HV-electrode. Here, one of the Helmholtz coils was run with reversed polarity in order to depress the local magnetic field at the electrode, thereby flattening the sum of the magnetic fields. The detector has a minimum extent of 4.5mm, and a maximum extent of 6.4mm along the diagonal. (The detector is flush with the end of the vacuum chamber)

access to the detector area, and the mechanical supports would be much more complex. Also, it was decided that the pre-spectrometer portion of the setup which had been used in Mainz should be approximated as closely as possible, in order to reduce the chance of unexpected geometrical effects causing changes in the results; this was another argument against a vertical setup.As a consequence, the setup was orientated horizontally, resulting in a significantly diminished count rate due to the angular dependence of the cosmic muon spectrum (see section 1.4.3), requiring a rotation of the initial design by 90°.

The CF150 flange upon which the turbopump was mounted was extended with an additional tube, as the magnetic field strength directly at the flange exceeded the safety limits of the turbopump.

A *Leybold* PTR90 vacuum gauge was attached to the last CF100 flange of the vacuum chamber. This was connected to a serial ADC; readout was accomplished via a small C program run on the DAQ-PC. During testing it became apparent that the vacuum gauge should not remain powered while the high voltage was applied to the electrode, as a significant number of electrons emitted by the gauge were reaching the detector and obscuring the desired signals. In consequence continuous monitoring of the vacuum chamber pressure is not possible; however, occasional measurements yielded a constant pressure between $9 \cdot 10^{-9}$ mbar and $2 \cdot 10^{-8}$ mbar.

The experimental setup during construction is shown in Fig. 4.4, while the finished experimental setup is shown in Fig. 4.6. During the course of the experiment, modifications were made, and the final setup is shown in Fig. 4.7.

4.2.1. Data Acquisition

The basic high-voltage vacuum test setup utilizes a quadratic silicon PIN diode (*Hamamatsu* S3590-06) mounted on a CF40 flange with a BNC feedthrough as a detector. Directly attached

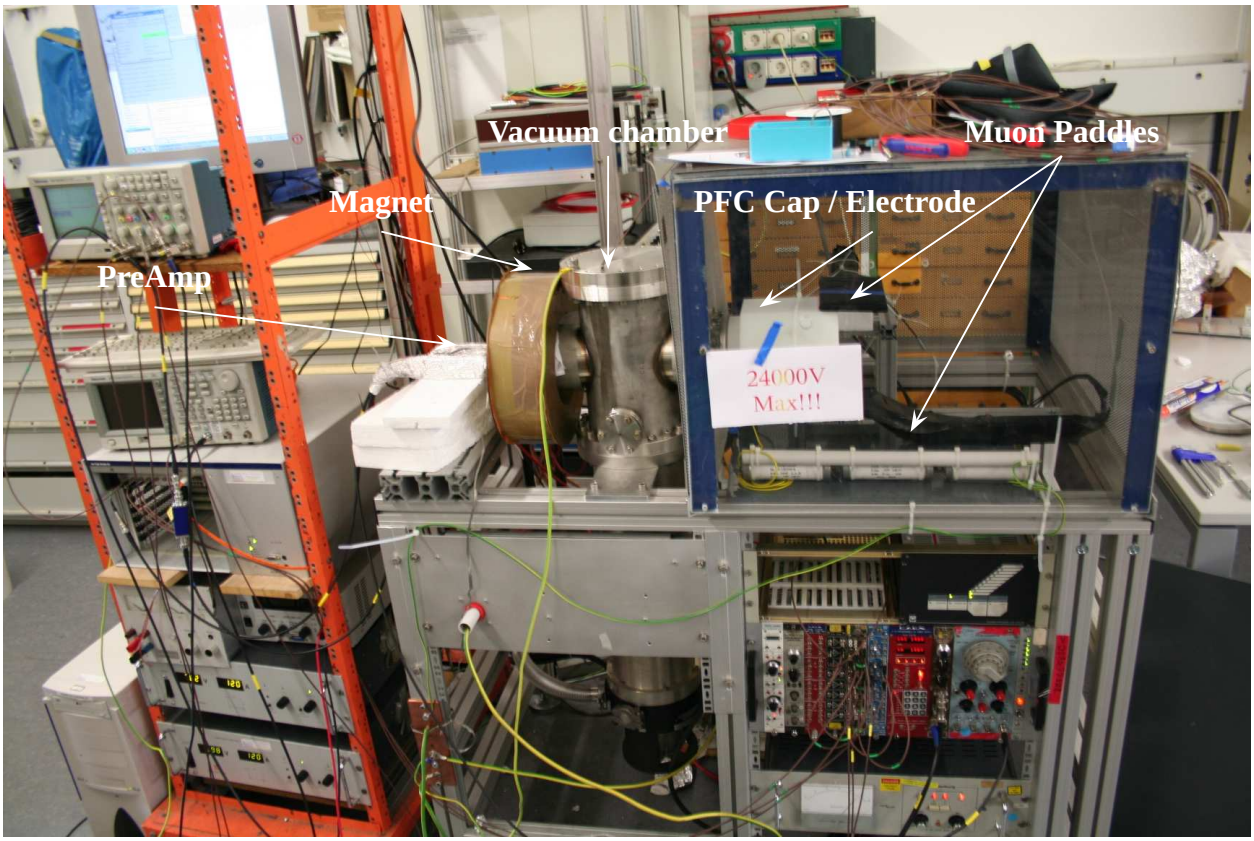

Figure 4.6.: View of the finished setup, as used in the first runs. Visible at the left is the rack with the VME crate containing the Flash ADC, the high-voltage cage within which the active portion of the experiment was contained is located at the right. Beneath this is the crate with the detector electronics.

to this detector is a CoolFET preamplifier (*AmpTEC* A250CF), which itself is connected to a spectroscopy amplifier (*EG&G* 576 Spectroscopy Amplifier). A *BNC* PB-4 pulse generator was used during the energy calibration. The detector is powered by an *ISEG* NHQ224M voltage supply. The data acquisition system utilizes a *Struck* SIS3320 Flash ADC, which can record data on up to eight channels simultaneously with a sampling rate of 200 MHz. The entire detector subsystem is powered by an *Liebert* Powersure PS7 uninteruptable power supply, which also serves to smooth the input voltage.

For the muon experiment, an additional high-voltage supply (*CAEN* N470) provides power to the photomultipliers of the muon paddles. The photomultiplier signals are amplified by an *ESN Electronic* FTA 810L eight-channel amplifier and discriminated by an *ORTEC* 934 Quad CFD (Constant Fraction Discriminator). The discriminated signals are fed into a *LeCroy* 622 Quad Coincidence logic unit, set to output a signal when both photomultipliers detect an event.

The timing signal provided by the preamplifier, the signal provided by the main amplifier after amplifying the energy output of the preamp, the discriminated signals of both muon paddles, as well as the trigger signal created by the logic unit are recorded by the Flash ADC. Unfortunately, the unamplified photomultiplier signals proved to be too short to be reliably recorded. A schematic of the entire detector system is shown in Fig. 4.8.

Figure 4.7.: View of the setup, as used in the last four runs. The cloth covering in place over the high-voltage cage which ensures no light enters the vacuum chamber was not removed for this photo.

4.2.2. High Voltage

A high voltage power supply (*Brandenburg* alpha series; $0 - 30\,\mathrm{kV}$) provides the high-voltage for the electrode. As the electrode-detector system acts in a similar way as a plate capacitor, the voltage ripple of the HV-supply directly induces noise in the detector; attaching HV-capacitors smoothes this ripple, reducing the amount of induced noise. This effect was much more pronounced in the setup for the steep cone wire emission tests (see [Zac09]) because of the reduced distance between electrode and detector.

4.2.3. Air Coils

Lastly, the magnetic coil is powered by two *Delta Elektronica* power supplies (Type SM15-200D) connected in series and run in master-slave configuration. A temperature sensor is attached to the magnetic coil and set to shut off the power supplies if the temperature exceeds $63^\circ\,\mathrm{C}$.

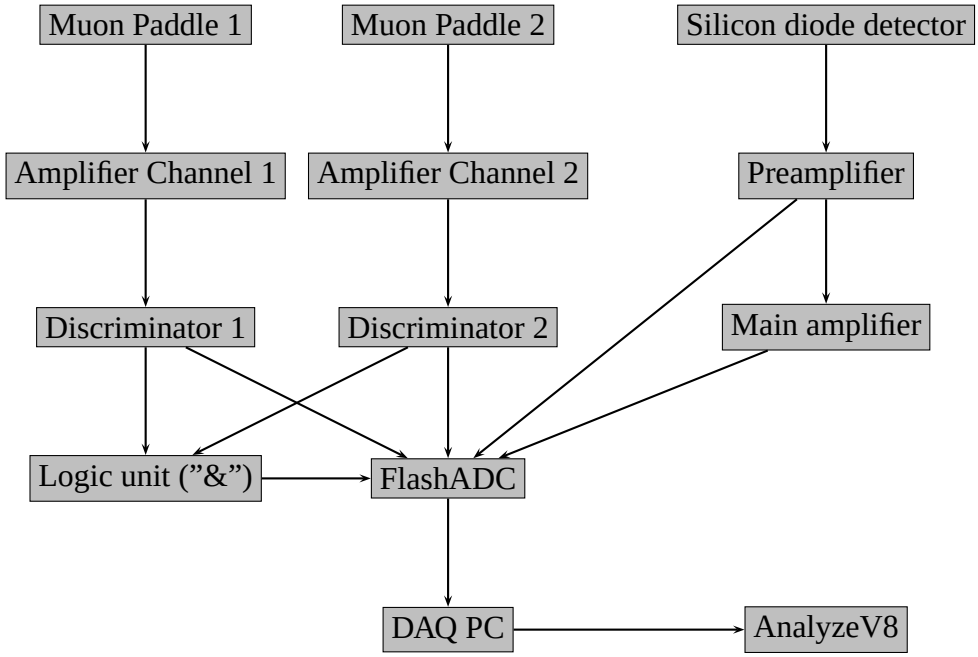

Figure 4.8.: Schematic of the data acquisition system of the Muon experiment.

4.2.4. Safety

The HV vacuum test setup was located in a publicly accessible laboratory in Münster, which necessitated ensuring that it would be impossible for visitors, students, and coworkers to accidentally suffer injury from the high voltage. Therefore the HV-related section of the setup was enclosed in a grounded high-voltage cage, including both muon paddles, the entire isolator flange, the flange electrode, and the HV-capacitors. Also, a PVC cap was fashioned by the in-house workshop to cover the isolator, primarily to allow the muon paddles to be moved closer to the actual electrodes for an increased count rate. This had the side effect of completely covering all vacuum parts which were attached to the high voltage supply, providing additional safety. A second HV-cage was constructed to prevent access to the HV components from beneath the setup. In addition, an interlock was added to the front panel of the cage, which is removable in order to allow access to the experiment, as well as a grounding rod to ensure the setup is grounded when open. These interlocks ensure that the front panel is closed and the connection between the HV-electrode and the ground point, provided by a grounding rod, is broken before the HV supply can be turned on as well as shutting down the HV if one of these conditions is no longer met.

While the electromagnet produces a peak field of $800 - 1000\,\mathrm{G}$ in its center during sustained operation, the field strength at the edges of the vacuum setup itself is under $50\,\mathrm{G}$. For this reason, it was not required to mark a $50\,\mathrm{G}$ line on the floor. However, caution must be used when working with metallic tools near the active electromagnet inside the perimeter of the setup due to its strong field.

4.2.5. Sustained operation

During sustained operation, the current passing through the magnet coil is limited to 120 A by the maximum waste heat capacity of the water cooling system.

Even with the PVC cap covering the large isolator, either the room should be darkened or the HV cage covered to prevent light from entering the vacuum chamber and causing noise, as the isolator tube to which the HV electrode is attached is not fully opaque. Both the detector high voltage as well as the electrode voltage must be off when venting or pumping the chamber. Also, the detector voltage must be turned off before powering off the preamplifier, and must not be turned on before the preamp is on as otherwise the preamplifier suffers damage. As the preamplifier utilizes Peltier cooling, optimal noise reduction is not reached immediately upon power on. Typical and maximum values for the various components are shown in Tab. 4.1.

Component	Typical value	Maximum value
Silicon PIN diode voltage	80 V	100 V
Muon paddle PMT voltage	1400 V	1400 V
Main magnet current	120 A	150 A (Short usage only)
Acceleration voltage	24 kV	24 kV

Table 4.1.: Typical and maximum values for the various active components of the vacuum setup.

4.2.6. Flash ADC settings

The Flash ADC settings utilized during the measurements are defined in a configuration file, as reproduced in listing 4.1. The most important settings are the sampling frequency of 100 MHz, the stop delay of 40,000 samples ($\equiv 400\,\mu$s), and the total sampling length of 656.36 μs. For the first channel, which records the preamplifier timing signal, high resolution sampling was enabled, thereby increasing the sensitivity of this channel by a factor of two. In addition, the trigger settings can be seen, with the unit triggering on a total level change of 500 pulse height units, summed over four samples corresponding to an average increase per sample of 125 pulse height units. The trigger signals actually had a increae of ≈825 pulse height units over 4 samples (40 ns).

Listing 4.1: SIS3320 FlashADC settings file for the muon measurements

```
1
2  /* Settings for Struck SIS3320 Flash ADC */
3
4  No_of_Modules 1
5
6  Base_Addr 0x40000000
7
8  /* common settings */
9  clock_frequency          100   /* clock frequency in MHz; allowed values for
10                                    SIS3320 module: 200 MHz, 100 MHz, 50 MHz */
11
12 page_size                4     /* samples per event:
13                                    0 - 16M , 1 - 4M , 2  - 1M , 3  - 256K ,
14                                    4 - 64K , 5 - 16K, 6  - 4K , 7  - 1K ,
15                                    8 - 512 , 9 - 256, 10 - 128, 11 - 64 */
16
17 stop_delay               40000  /* trigger pulse delay in units of
18                                    1/(clock frequency) */
19 enable_internal_trig     1      /* 1 - internal trigger, 0 - external trigger
20                                    via LEMO input number 2 */
21 trigger_peaking_time     4
```

```
trigger_sum_g           4
trigger_pulse_length    4     /* length of generated trigger pulse in units
                                 of 1/(clock frequency) */

/* signal integration */
integrate_signals       0     /* integrate signals directly after readout to
                                 limit the amount of data to be transfered */
substract_offset        1     /* substract offset before integrating; in this
                                 case absolute values |value - offset| are
                                 integrated */

/* individual channel settings */
Module 1
        /* Channel readout activated (1 - on, 0 - off) */
        Channel_active  1       1       1       1       1       0       0       0

        /* Channel gain (0 - full scale mode, 1 - half scale mode) */
        Channel_gain    1       0       0       0       0       0       0       0

        /* Channel DAC setting */
        Channel_DAC     0xa000 0x8000 0x8000 0x8000 0x8000 0x8000 0x8000 0x8000

        /* Threshold range: +-65535 (0 means: channel does not trigger) */
        Thresholds      0       0       0       0       500     0       0       0

        /* Threshold type: 0 = GT; 1 = LT */
        Thr_type        0       0       0       0       1       0       0       0

        /* FADC zero signal level (0-4095) */
        Zero_offset     2390    795     822     818     810     799     802     806
```

4.3. Future muon experiments

The initial goal of the muon measurements was determining the energy distribution of low-energy electrons ejected by muons, with an assumed secondary electron yield on the order of 1 e^- per muon. While these measurements did not succeed at Mainz due to the unexpectedly low electron yield, other measurements done at Mainz have showed that it is possible to determine the energy of an ejected electron by measuring its flighttime, over a range of $E_e < 50\,\text{eV}$, with higher-energy electrons having no discernible time separation (see [Val09] for details). Using these figures, a future experiment could be run at Mainz and the flighttime could be extracted from the coincidence data. This would require a much lower background and at least the ten-fold measurement time vs what was available during our measurements. The energy range would be divided into $30 - 50\,\text{eV}$ steps, covering the entire unknown energy range.

Additionally, if more than two muon paddles were available, say 4N paddles, N paddles could be placed at the top left, further N at the top right, as well as bottom left and bottom right of the electrode. Then recording could be triggered whenever any topleft paddle had a coincidence event with any bottom right paddle, etc, in order to record many incident angles at once. As the Flash ADC units are limited to eight channels, this would require some means of combining the muon paddle signals to reduce the number of channels needed. One possibility would be varying the pulse height of the digital trigger signal produced by the discriminators, for example the first paddle's trigger signal having a height of 200 mV, the second 400 mV, the third 800 mV, and so on, and connecting these signals in parallel in order to create a pseudo-binary representation of which paddles triggered in the stored waveforms.

CHAPTER 5

RESULTS OF THE MÜNSTER MUON EXPERIMENT

The following chapter describes the methodology applied and the results obtained while analyzing and interpreting the data recorded during the Muon measurements in Münster using the setup described in chapter 4, to ultimately arrive at the low-energy secondary electron yield for muons passing through stainless steel.

5.1. Determination of the secondary electron yield

The primary goal of the experiment is the determination of the average number of low-energy secondary electrons ejected by an incoming muon, characterized by the electron yield $Y_{\mu-\mathrm{SE}}(\beta(S))$ for a given muon incidence angle $\beta(S)$ relative to the electrode normal in Run S, with the muon paddle positions kept constant during each individual run. This results in the data for each run being associated with a specific muon paddle geometry, as well as a set of voltage settings. The determination of this yield is dependent on three factors: (1) the number of accepted muon coincidence events $N_\mu(S)$ which remain after cuts are applied to the initial muon coincidence count $N_{\mu^*}(S)$, (2) the number of secondary electrons ejected during this run $N_{\mathrm{e}^-}(S)$ as determined from the detected secondary electron count $N_{\mathrm{e}^{-*}}(S)$, (3) the full transport efficiency of the experimental setup, i.e. the probability that a muon coincidence event can lead to electrons which can reach the detector $\varepsilon_{\mathrm{Setup}}(S)$. The applied cuts are explained in detail in section 5.2.4.

$$Y_{\mu-\mathrm{SE}}(\beta) = \frac{N_{\mathrm{e}^-}(S)}{N_\mu(S)} \cdot \frac{1}{\varepsilon_{\mathrm{Setup}}(S)} \tag{5.1}$$

$\varepsilon_{\mathrm{Setup}}(S)$ may be further subdivided into two factors, first the distribution of muon hits on the electrode $D_\mu(S)$, which depends on the paddle locations during the run, and secondly the probability that an electron which is emitted from a given point on the electrode reaches the detector T_{Setup}, this latter factor being independent of the paddle configuration and therefore constant for all runs.

$$\varepsilon_{\mathrm{Setup}}(S) = D_\mu(S) \cdot T_{\mathrm{Setup}} \tag{5.2}$$

5.1.1. Calculation of electron transmission function T_{Setup}

The Geant4 simulation of the KATRIN main spectrometer (See section 2.3) was modified to simulate the transmission function of the vacuum setup utilized in the Münster measurements. The electromagnetic design of the experimental setup is depicted in Fig. 4.3. The modified simulation includes a new event generator which creates electrons with a homogeneous spatial and isotropic angular distribution above the electrode. These electrons were tracked and their energy deposition in the detector was recorded, along with the track origins. These results were used to generate the transmission function of the experimental setup as well as the energy distribution of the detected electrons.

Due to the fact that the actual experimental setup was not perfectly noise free, and therefore some events would not be identifiable, the backscattering statistics of the simulation are used to correct the count rate (see the example run analysis in section 5.2.4).

Also, while it is possible to define the scintillator paddle geometry directly within the Geant4 simulation and use this to randomly generate primary muons according to a selected cosmic muon angular spectra, separating the transmission function of the vacuum chamber from the incident

muon distribution function allowed us to recalculate $D_\mu(S)$ for each detector configuration independently of T_{Setup}, which saved a considerable amount of CPU-time as well as allowed a much more accurate simulation of $D_\mu(S)$.[1]

As the energy distribution of the secondary electrons was not known, flat energy distributions were used to generate electrons with starting energies between 0 and 2.5 keV and 0 and 250 eV. An additional transmission function with high-energy electrons was determined in order to verify the behavior of high-energy secondaries. Since a square detector was used, we did not expect the transmission function to be radially symmetric, but this was the case: For large radii, the electrons were either magnetically reflected or collided with the electrode during their cyclotron motion before the irregular shape of the detector became relevant. Therefore we can use a radially dependent function $T_{\text{Setup}}(R)$ to characterize the transmission function. The resulting transmission functions are shown in Fig. 5.1, and the simulated total energy spectrum in Fig. 5.2.

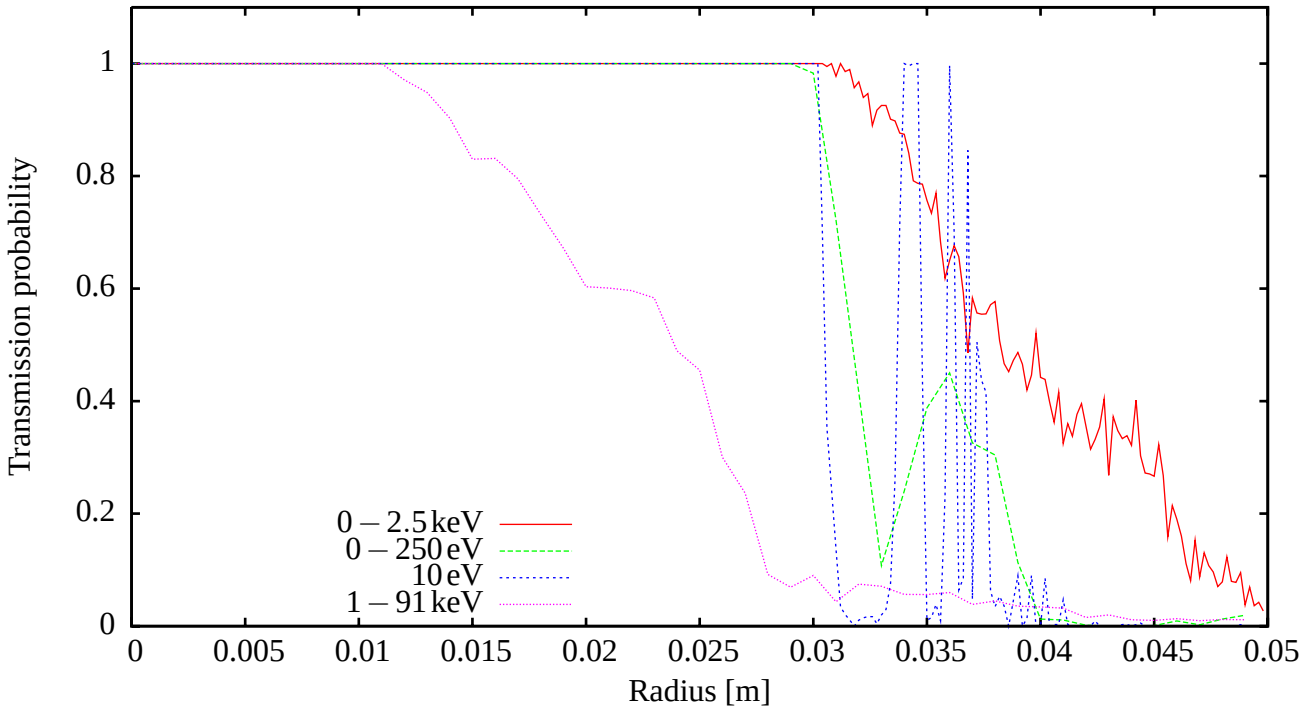

Figure 5.1.: Simulated transmission functions for electrons with a flat starting energy distribution between 0 – 2.5 keV, 0 – 250 eV, and 1 – 91 keV. Due to the large range of starting energies, the transmission cutoff is very soft for electrons between 0 – 2.5 keV; when the energy range is reduced, the transmission function becomes sharper. Also, the cutoffs due to the cyclotron motion are visible in the 10 eV electron transmission; here, the starting angle's influence is almost zero, and solely the starting radius decides whether the electrons will reach the detector or either collide with the ring electrode or fly past the detector. The high energy transmission function demonstrates how the transmission efficiency decreases with increasing electron energy.

[1] Simulating 10^8 coincidences for the calculation of $D_\mu(S)$ takes some few hours on a typical office PC, while the simulation of a transmission function using 50k events takes several days running 50 parallel jobs on a computer cluster.

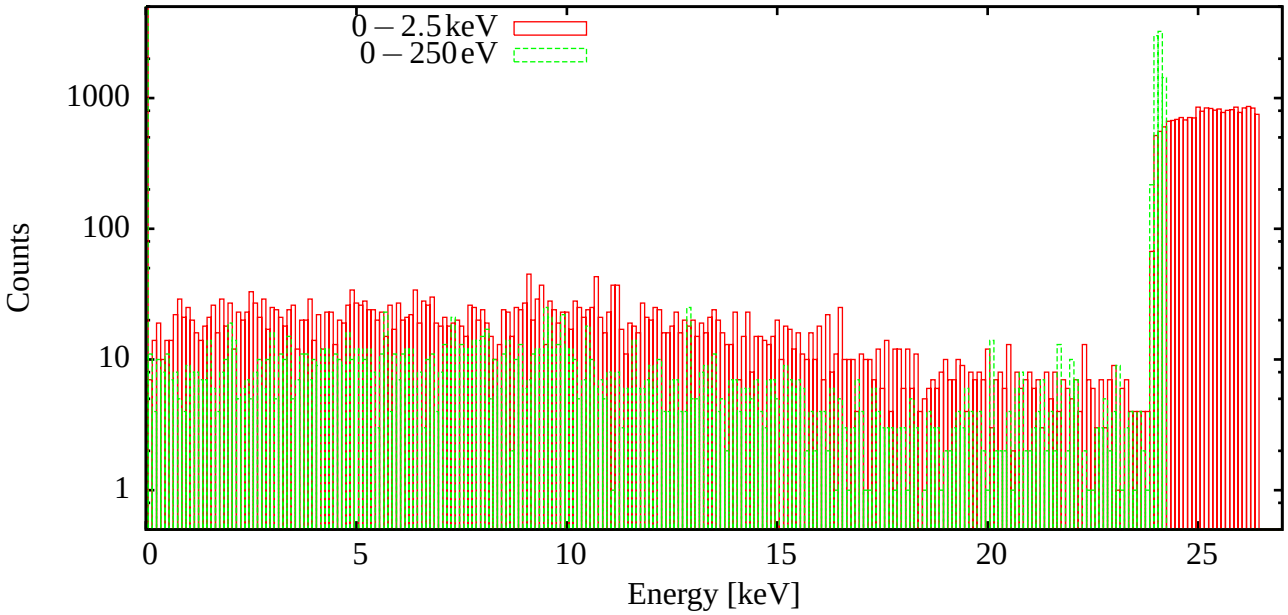

Figure 5.2.: Simulated energy distribution of transmitted electrons with a starting energy between $0 - 2.5\,\mathrm{keV}$, as well as between $0 - 250\,\mathrm{eV}$. While no broadening was applied to simulate the detector response, the full energy peak is broadened by the applied energy range. Additionally, backscattered events are visible as a fairly uniform background.

5.1.2. Calculation of the incident muon intersection distribution on the electrode $D_\mu(S)$

The second factor which was required to determine the transport efficiency $\varepsilon_{\mathrm{Setup}}(S)$ was the distribution function of muon hits on the electrode. A program was written which generates both the radial and two-dimensional hit distribution of muons, using a given muon paddle configuration. The muon paddles were approximated with single planes instead of a true box. Additionally, no electromagnetic interactions were simulated. Therefore, the simulated muons cannot be deflected, their direction remains constant.

A description of the incident muon angular spectrum was required in order to produce an accurate incident location distribution. Several distributions were implemented: (1) an isotropic distribution for the simplest case; (2) the commonly used $\cos^2$ distribution which is an accurate approximation for angles close to vertical; (3) the $\cos^*$ (see section 1.4.3 for a detailed description) distribution which yields an accurate distribution for all angles.

The simulated muons, with starting locations randomly scattered over the first muon paddle, were assigned a random direction according to the selected angular spectrum, and their intersection points with the planes defined by the muon paddles as well as their intersection points with the target plane were calculated. Using these points, all events which did not intersect both paddles were rejected, and subsequently the intersection points on the target and the incident angle of the remaining events were recorded. Fig. 5.3 shows two resulting distributions for two different paddle configurations.

Using this data, with R_i referring to the electrode intersection radius of the simulated incident muon

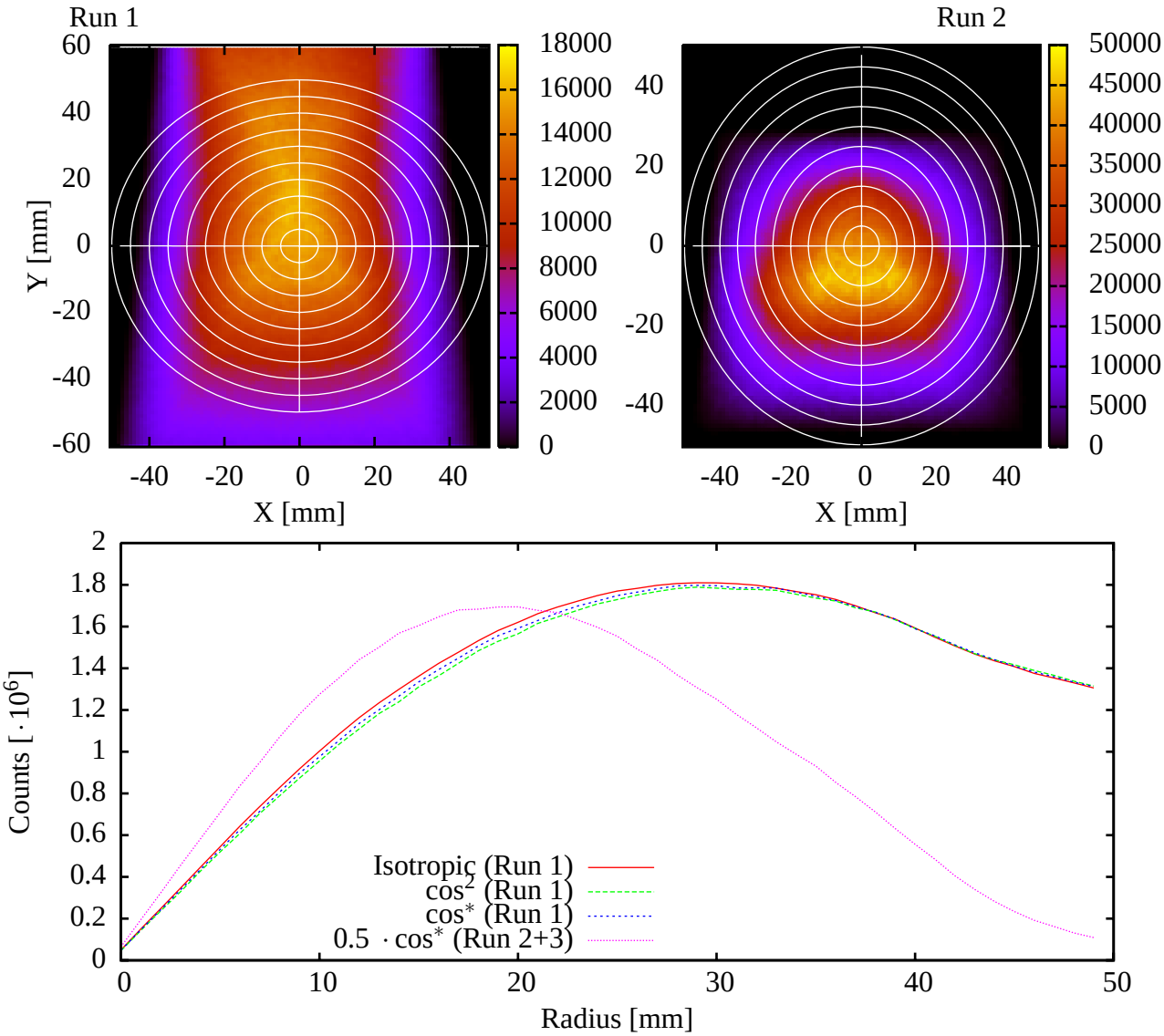

Figure 5.3.: Results of the muon distribution calculations of Run 1 and Run 2+3. **Top left**: This distribution results from the Run 1 paddle geometry. **Top right**: This distribution is the result of the Run 2+3 geometry, where the paddles were located significantly further apart. Note the significantly higher maximum density of hits in the top right distribution, as well as the much smaller total area where intersections are possible. Both simulation runs were done using the same number of muon coincidences in the muon paddles and using the $\cos^*$ muon angle distribution. The differences between the two distributions are caused entirely by the paddle geometry. Rings of different radii are shown in white to illustrate the generation of the radial transmission function; the total number of hits in each ring is used to generate one value of the binned radial hit distribution (Note: the actual binning using a Δr value of 1 mm between rings, not 5 mm as shown). **Bottom**: The resulting radial distributions are shown for the 2D distributions; in addition, the resulting radial distributions when using other angular muon distributions are shown for Run 1.

coincidence number i, and using a total count of $N = 10^8$ coincidences, the binned radial muon incident count distribution $D_\mu(S,R)$ was calculated, with a binwidth Δr of 1 mm:

$$D_\mu(S,R) = \sum_{n=0}^{N} T(R,R_i) \tag{5.3}$$

with

$$T(R,R_i) = \begin{cases} 1, & \text{if } R_i \in [R, R+\Delta r[; \\ 0, & \text{otherwise.} \end{cases} \tag{5.4}$$

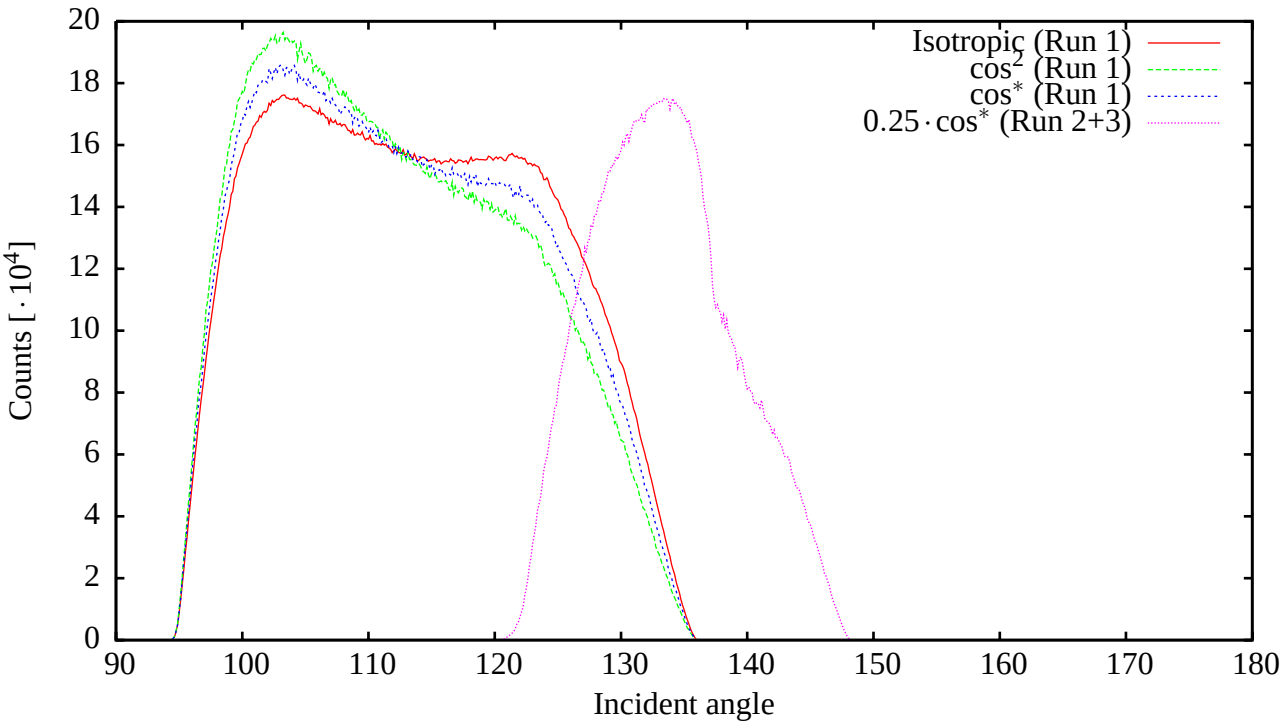

Figure 5.4.: Angular incident probability distribution of detected muon events for three primary muon distributions, using the paddle geometry of Run 1. While the $\cos^*$ distribution was used for the calculations, the other distributions are shown in order to demonstrate the influence of the input angular spectrum. The angles are relative to the electrode normal. Again, the distribution for Runs 2+3, where the paddles were located significantly further apart, is shown as a comparison.

In order to correctly calculate the angular distribution of the incoming muons that may lead to an electron-muon coincidence, each simulated coincidence event must be weighted with the probability that an electron ejected at the intersection radius R_i will arrive at the detector. For this probability, the previously calculated $T_{\text{Setup}}(R)$ was used. The number of muons arriving at a given angle was calculated as follows, with β_i being the incidence angle of the simulated muon coincidence i relative to the electrode normal, and N being the total number of simulated muon coincidences:

$$N(\beta) = \sum_{n=0}^{N} T(\beta,\beta_i) \cdot T_{Chamber}(R_i) \tag{5.5}$$

$$T(\beta,\beta_i) = \begin{cases} 1, & \text{if } \beta_i \in [\beta, \beta+\Delta\beta[; \\ 0, & \text{otherwise.} \end{cases} \tag{5.6}$$

This allows the determination of the correlation between the secondary electron yield and the average incident muon angle. The average incident angle is determined by calculating the average of equation 5.5 as follows:

$$\beta(S) = \arccos\left(\frac{\sum_{\beta=0^\circ}^{\pi/2}\cos(\beta)\cdot N(\beta)}{\sum_{\beta=0^\circ}^{\pi/2} N(\beta)}\right) \tag{5.7}$$

which results in an average angle of $112.5^\circ \pm 1^\circ$ for run 1, with the angular incident distribution shown in Fig. 5.4. The simulation was run with 10^8 events, resulting in a negligible statistical error. However, the uncertainty in the muon paddle positions leads to a small systematical error of $\pm 1^\circ$.

5.1.3. Full transmission efficiency

As the transmission function of the idealized setup is radially symmetrical, the two dimensional muon incident location distributions can be converted into radial distributions. Then $\varepsilon_{\text{Setup}}$ can be calculated by multiplying these distributions with the radial setup transmission function, T_{Setup}, and normalizing with the number of simulated muon incident events N, in order to arrive at the total transmission probability. In the case of binned functions, the following results:

$$\varepsilon_{\text{Setup}} = \frac{\sum_{r=0}^{R_{Max}} D_\mu(S,r)\cdot T_{\text{Setup}}(r)}{N} \tag{5.8}$$

5.2. Determination of $N_{e^-}(S)$ and $N_\mu(S)$

While the previous factors which contribute to $Y_{\mu-\text{SE}}(\beta)$ were determined by simulating the experimental setup, the remaining factors are determined by analyzing the recorded data.

5.2.1. Common parameters of all runs

During the initial test measurements, the maximum usable voltage was limited by the HV supply, the limiting factor being the HV capacitors employed during the final measurements to smooth the voltage ripple of the electrode. Therefore, in all measurements, the electrode voltage was set to the maximum voltage allowed, i.e. $-24\,\text{kV}$. Another difference to the test measurements conducted while commissioning the vacuum setup was the utilization of a spectroscopy amplifier to amplify the signals before recording the waveforms. In addition, the timing signal produced by the preamplifier was recorded in case we decided to analyze it, but it turned out to be too small to reliably locate all events within the voltage resolution of the Flash ADC. Finally, the digitized signals of both muon paddles were recorded along with the coincidence signal, in order to be able to reject events occurring while the paddles were producing noise and possibly producing false

trigger events. The signals were sampled for 656 μs, while the transmission delay of the setup is some few microseconds; this large timewindow allows us to generate the spectrum of the background noise present during each run on an event-by-event basis without requiring interrupting the measurements. This allows the correlation between background level and event indexes, thereby facilitating the removal of all events taking place during electron discharges.

The magnet was run with a current of 120 A, resulting in a maximum field strength of 0.08 T in its center, this being the location of the detector. The detector voltage was kept at 80 V for all runs.

5.2.2. Event identification

The recorded data was analyzed with the previously described AnalyzeV8 software (see sections 3.3ff.). A data analysis scheme was conceived for use with all waveforms recorded during these runs, with the AnalyzeV8 settings remaining constant. However, the cuts applied to the list of found peaks varied in order to adapt to the predominant noise level in each run. Additionally, intervals of events were fully removed where the noiseband obscured the single electron peak. The removed event intervals are listed in the individual run discussions (see appendix A).

The data analysis process is illustrated with the data taken during the first run. Shown in Fig. 5.5 is a sample event with three of the five recorded data channels, as well as the smoothed main amplifier signal, which is shown enlarged. This smoothing of the main amplifier waveforms was done with a running average using $N = 25$ samples; subsequently, the peak search algorithm was run over the resulting waveforms. As in excess of 99% of each recorded waveform was background noise, we could take the average of the full waveform and utilize this as the baseline passed to the peak search algorithm. This was verified by generating the distribution of the waveform height and comparing this with the average height for numerous sample events. The located events were written to an output file and described by parameters such as peak height, time offset, absolute time, width, area, etc. of this peak. (See section 3.3.7 for details on the peaksearch algorithm.)

5.2.3. Energy Calibration

During noise optimization and the first two runs, a pulser was included in the setup and connected to the pulser input of the preamplifier. The pulser's peak was used to calibrate the energy spectra and subsequently removed from the data during further analysis. In order to determine the energy equivalent of this peak, the maximum height ($U_0 = 11.8 \pm 0.2$ mV) of the pulser signal was measured using an oscilloscope. This value was used to calculate the energy deposition required in the detector to create a preamplifier signal with the same height. The action of the charge-integrating preamplifier can be described as the integration of the charge created in the detector on the feedback capacitance $c = 0.5$ pF of the preamplifier:

$$C = \frac{Q}{U} \tag{5.9}$$

Using the known values of C and U_0, the number of electrons (N_{e^-}) needed for an equivalent charge deposition Q in the preamplifier can be determined.

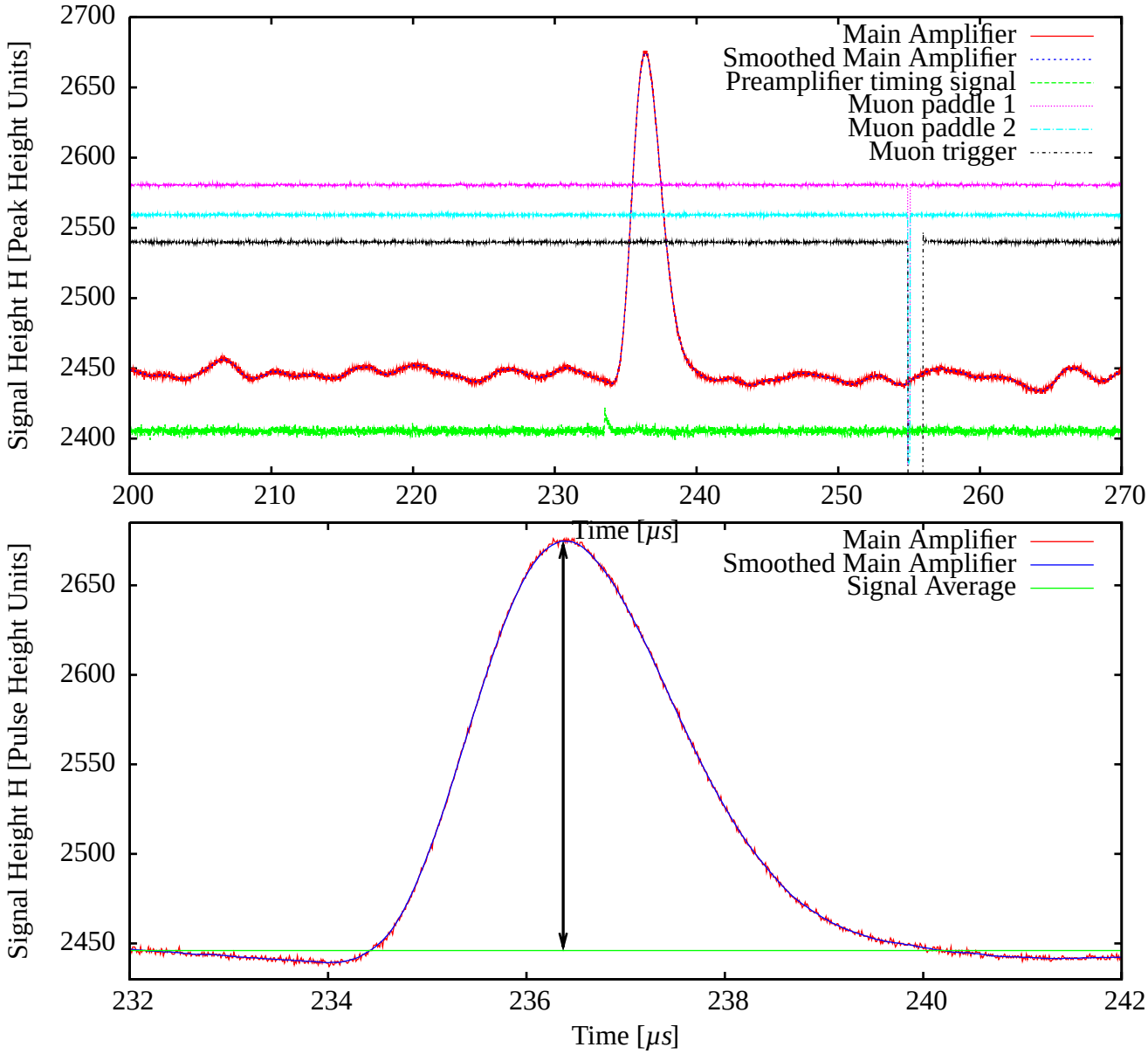

Figure 5.5.: Top: Raw signal waveforms recorded by the DAQ system for a sample event, as well as the smoothed main amplifier signal. Signal height of the muon paddle waveforms as well as the trigger has been reduced, and all signals contain artificial vertical offsets. Visible is a pulser peak along with the corresponding timing peak of the preamplifier; the peak height of single electrons is about a fifth of the pulser peak height, making the preamplifier peak indistinguishable at this resolution.**Bottom**: Closeup of the pulser event, illustrating how the running average smooths the recorded waveform, removing high-frequency noise.

$$Q = C \cdot U = N_{e^-} \cdot e \tag{5.10}$$

In a silicon PIN diode detector, incoming particles initiate a cascade of electron-hole pairs. From the energy W_{Si} required to create one pair (taken from [Maz08]), the equivalent energy deposition required for the creation of N_{e^-} electrons and holes may be calculated:

$$Q = N_{e^-} \cdot e = \frac{E_{dep}}{W_{Si}} \cdot e \tag{5.11}$$

$$E_{dep} = \frac{Q}{e} \cdot W_{Si} \tag{5.12}$$

$$W_{Si}(300K) = 3.65\,\text{eV} \tag{5.13}$$

Combining these two equations, we can determine the energy equivalent of the pulser signal:

$$E_{\text{Pulser}} = \frac{C \cdot U}{e} \cdot W_{Si} \tag{5.14}$$

The resulting energy equivalent of the pulser signal is $134.4 \pm 2.6\,\text{keV}$. The pulser peak is centered on $x = 222$ in the energy spectrum, which is equivalent to a peak height of 222 pulse height units in the recorded waveform. As the average of each recorded waveform was subtracted from the peak height while identifying peaks, with this average being defined as equivalent to 0 keV, this value was used as a second calibration point. Therefore, the full conversion from signal height to energy is:

$$E_{Signal} = H_{Signal} \cdot \frac{134.4\,\text{keV}}{222} \tag{5.15}$$

5.2.4. Run analysis

In this section we will demonstrate how the energy and timing cuts were chosen for each run in order to remove the noise as well as uncorrelated events while retaining a high secondary electron event count, in order to determine both the final electron count $N_{e^-}(S)$, as well as the final event count $N_\mu(S)$. Again, the data recorded during the first run is used to demonstrate this. The most important figures of the other runs follow in appendix A.

In this first run, one muon paddle was placed on either side of the electrode, one at top right and one at bottom left, thus ensuring that the majority of coincidence muons pass through the electrode surface. The simulated hit distribution was shown previously, in Fig. 5.3. The paddle configuration is shown in Fig. 5.6.

In order to analyze the background noise level over the course of the run, the time series of events is used, as is seen in Fig. 5.7. The pulser band is visible near 140 keV, as well as a very thin band of single electron events near 25 keV. In the case of Run 1, the background noise level remains constant throughout the run, at an acceptable level, i.e. significantly below the single electron band at 24 keV. Therefore it is not neccesary to remove time intervals because of high noise levels, as in other runs; these are then marked as such in appendix A.

In order to determine a reasonable noise cutoff, the list of found peaks was binned in order to generate the energy spectra shown in Fig. 5.8. A noise cutoff was chosen where the large random noise peak is fully removed. In the case of the first run, we removed all peaks with a height of less than 22 pulse height units, this being equivalent to 13.3 keV.

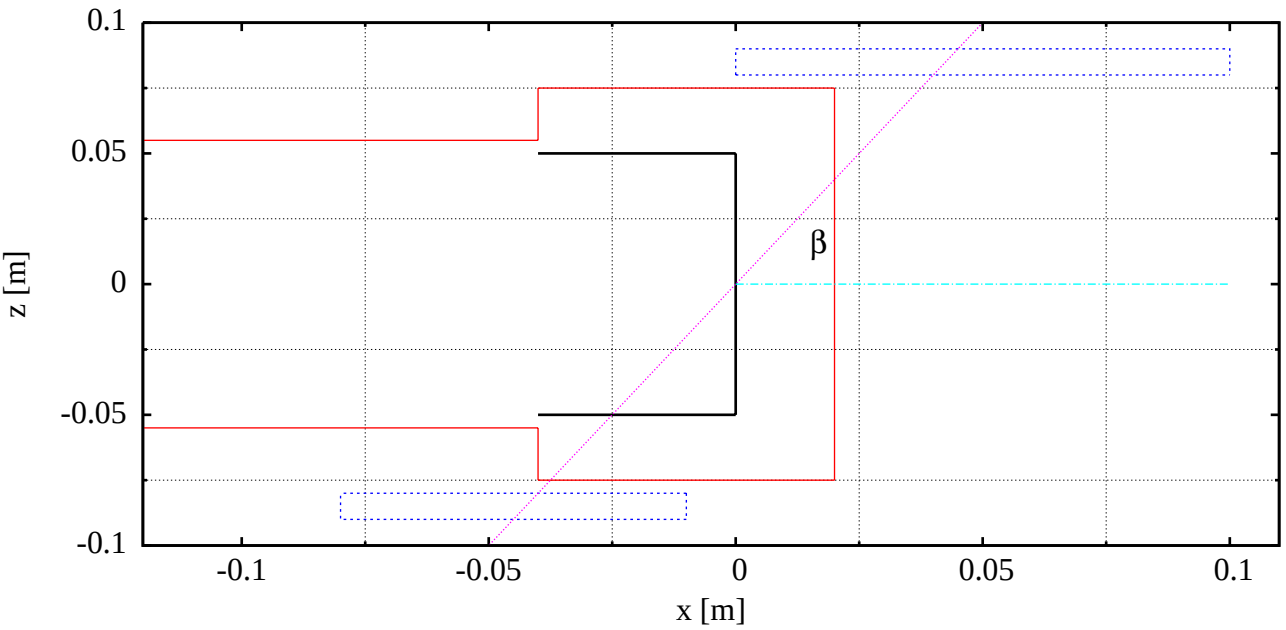

Figure 5.6.: The paddle configuration as used in Run 1. The metallic inner surface of the vacuum chamber is shown in black, the outer surface in red, and the muon paddles in blue. The bottom paddle was arranged lengthwise resulting in the shorter length, and offset by one centimeter. An example muon is shown passing through both muon paddles and the electrode, at an angle β to the electrode normal.

Using this noise cutoff (13.3 keV), the entire noisepeak is eliminated while retaining the full 24 keV single electron peak. However, in doing this we are also removing some events between the noise peak and the single electron peak which most likely are backscattered events. Also noticeable in the energy distribution are the higher-order electron peaks caused by multiple electrons simultaneously arriving at the detector, as well as the pulser peak. In Fig. 5.9, the electron event times are shown. Clearly visible is a small band of events which coincide with the trigger, the trigger occurring at 255.36 μs. There is also a wider vertical band near event 9500, this being caused by a few scattered events with a large number of secondary electrons identified as resulting from discharges. The plot also shows that the secondary electrons near the trigger are spread out well and do not occur in bunches. To better understand the time distribution of the secondary electrons, we binned this data, as is shown in Fig. 5.9. We then defined a band with a 1 μs width as the coincidence interval, and generated the energy spectrum during this interval. This is the second energy spectrum shown in Fig. 5.8.

By comparing these two energy spectra (shown in Fig. 5.8), the first being the full 257 μs of data and the second only 1 μs, we could determine for which energies the coincidence events dominated. All areas where the green 1 μs energy spectrum is similar to the full spectrum correspond to energies where the electron event rate is dominated by coincidences, likewise the areas with a significantly higher rate of electrons in the full spectrum are energy ranges where there is no high proportion of coincidence events. Using this, a cutoff was set on the maximum event energy, removing the highest energies, which were dominated by background events. A value of $6.5 \cdot 24$ keV was chosen, as events above this energy are most likely caused by cosmic rays interacting with the detector, rather than multiple secondary electrons. This is based on the fact that secondary electrons with high energies are not be transmitted very well due to their large initial cyclotron radius and high energy which ensure they do not reach the detector, as can be seen in the transmission

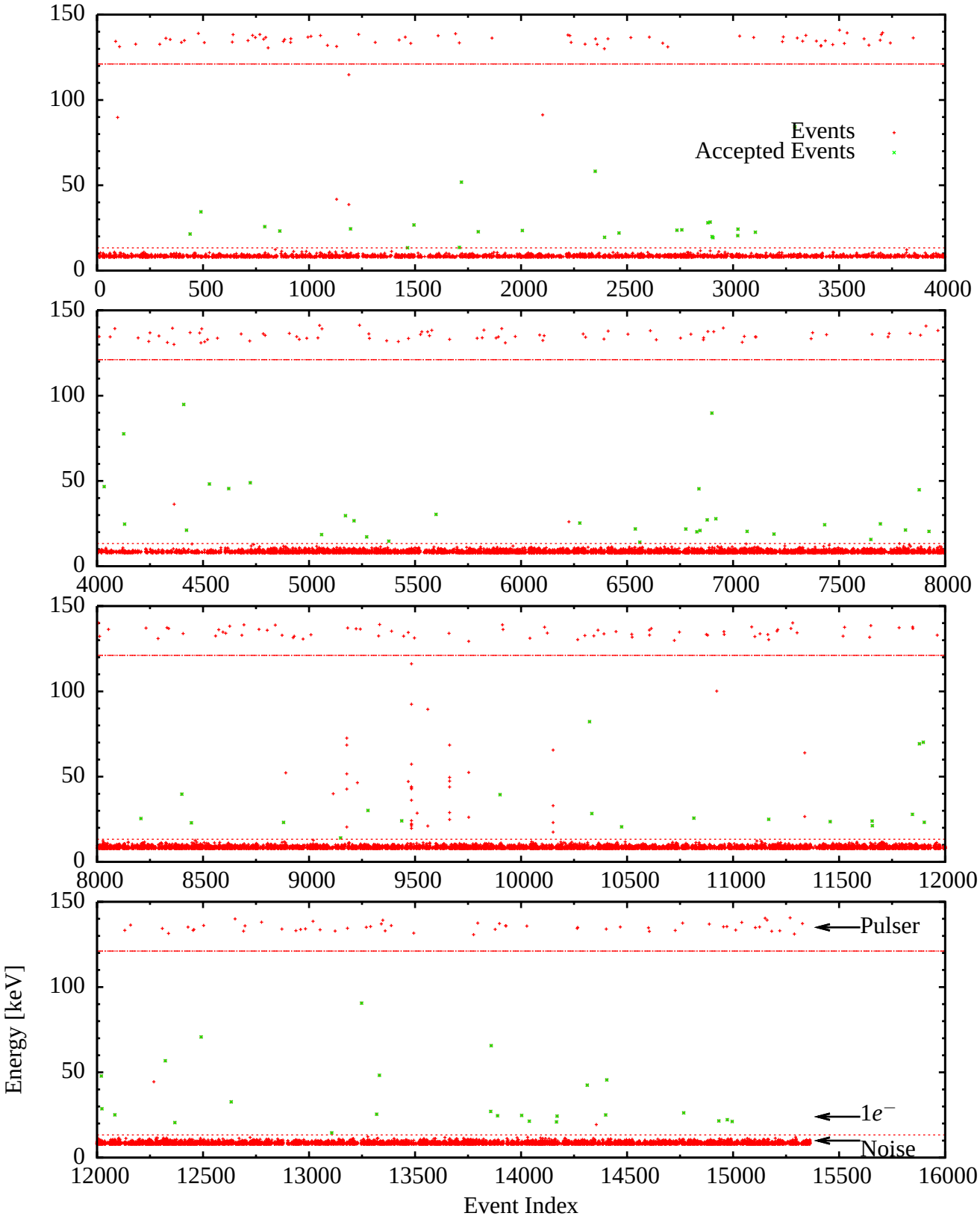

Figure 5.7.: Event energy vs. event index, Run 1. The noise level remained constant throughout this run, while pulser events occasionally coincided with the recorded interval. The events remaining after all cuts have been applied are overlaid in green. Near event 9500 several events with discharges are visible, with many registered electron events, these were removed.

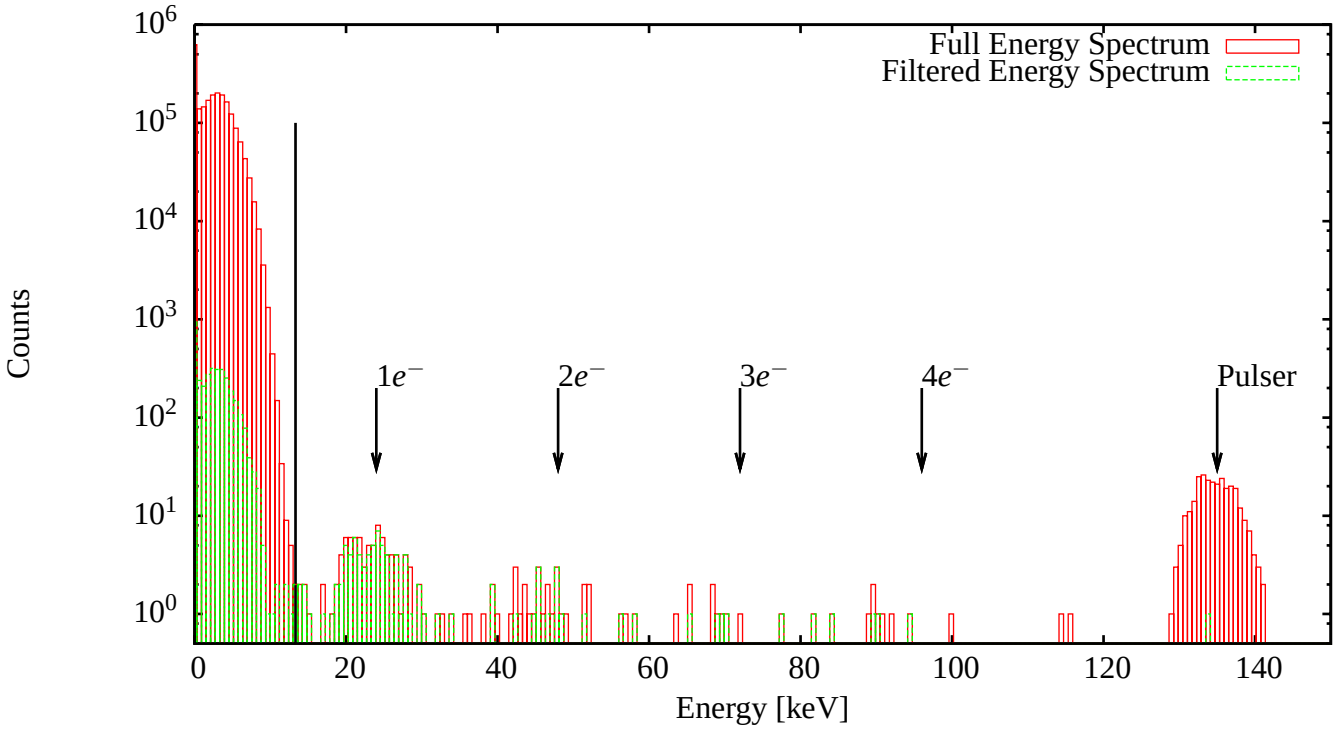

Figure 5.8.: The total energy spectrum of all events taken during the Run 1, as well as the filtered spectrum of events which occured in a window of a microsecond around the trigger pulse. The fact that the single and double electron peaks of both spectra overlap very well is a strong indication that these events are correlated with the incident muons, and not just randomly discharged electrons.

function shown in Fig. 5.1. Also, the probabilities of a single high-energy secondary electron or a large number of simultaneous low-energy secondaries being ejected are very low.

As we used a noise cutoff of $E_{\text{Cutoff}} = 14\,\text{keV}$, it is safe to assume that a few single-electron events which were backscattered and only deposited part of their energy were removed. Therefore it was necessary to determine how this factor would modify the true count rate. Hence a correctional factor was used when determining the total event count which is only applied to the detected $0-24\,\text{keV}$ electron count rate N_{Single}. The backscattering probability of electrons striking silicon, ε_{bsc}, is 17.1% according to the original Geant4 transmission simulations[2], which agrees with the values of 16% for 25 keV electrons with a 0° and 18% for electrons with a 30° incident angle according to calculations using results from [Tab71, Kan78]. Therefore, the Geant4 value is used for backscattering corrections resulting in the corrected single electron count rate N_{1-e^-}.

As the statistics of the runs are not high enough for advanced backscattering corrections using the area of a fit in the single-electron peak, the backscattering correction was approximated in the following manner: it was assumed that the energy deposition of the backscattered electrons follows a uniform distribution after the broadening due to the detector resolution is applied.

$$\varepsilon_{\text{bsc}} = \frac{d\varepsilon_{\text{bsc}}}{dE} \cdot E_0 \tag{5.16}$$

[2] For $0-2500\,\text{eV}$ electrons

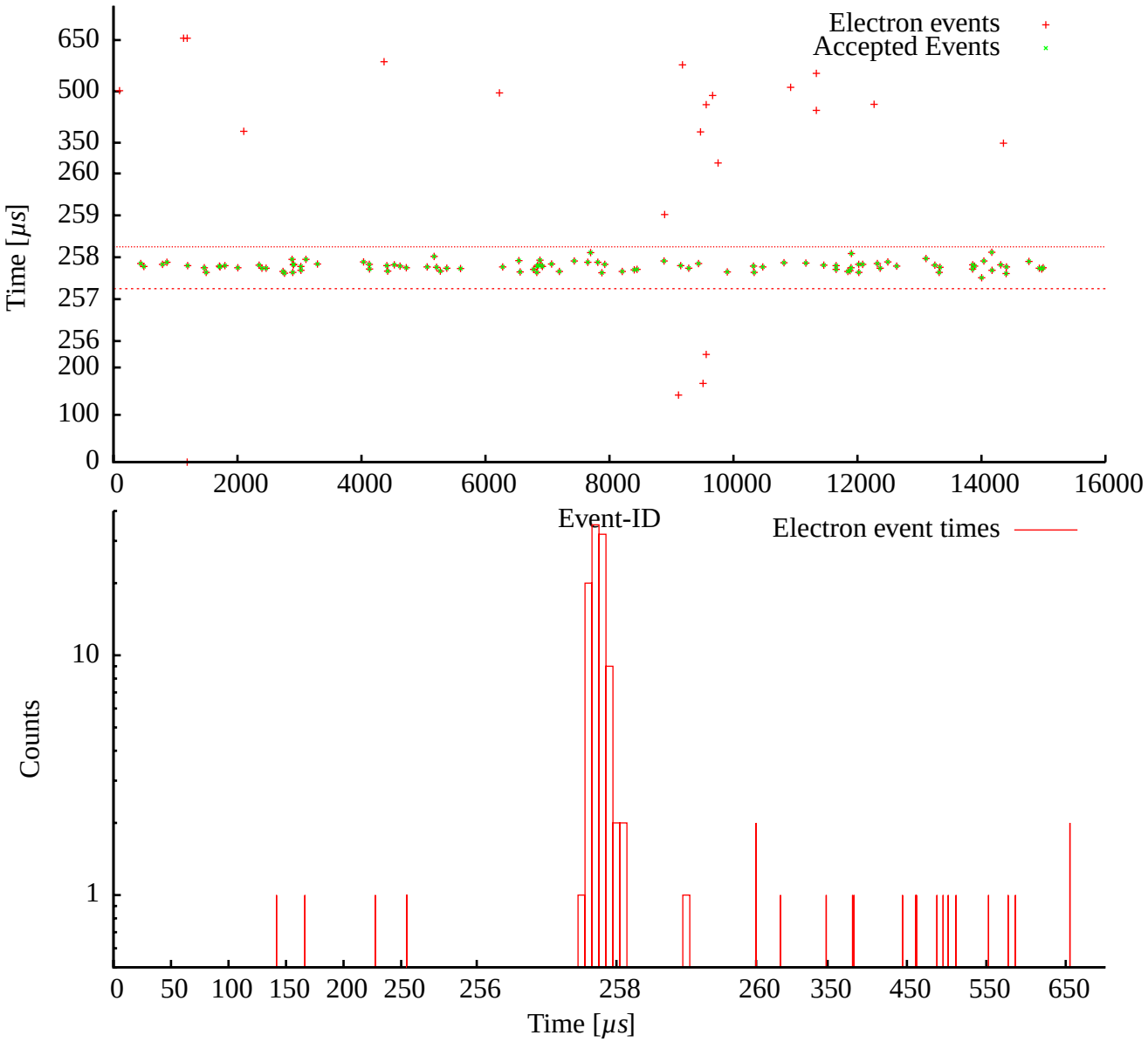

Figure 5.9.: Top: Electron event times vs. event ID. The electron discharge or high noise band previously visible around event 9500 has been removed, as well as the pulser events. The coincidence window is shown. The recorded waveforms start 255μs before the trigger condition is fulfilled. In this case no events have been removed from within the coincidence band. All secondary electron events are shown in red, and the events which were not removed when applying cuts are shown in green. **Bottom**: The same electron arrival times, now binned with a bin width of $0.1\,\mu$s. The coincidence electrons form a very sharp peak, while the very low background rate is visible as random events during the full timespawn.

Therefore, the number of backscattered electrons in an energy interval $[E_{\text{min}}, E_{\text{max}}]$ can be determined from the true number of single electron events N_{true} using the following equation:

$$N_{\text{bsc}}(E_{\text{min}}, E_{\text{max}}) = N_{\text{true}} \cdot \frac{d\varepsilon_{\text{bsc}}}{dE} \cdot (E_{\text{max}} - E_{\text{min}}) \tag{5.17}$$

Using the number of electrons in the interval between the lower noise threshold E_{cutoff} and the

upper edge of the $1-e^-$ peak ($E_{\max} = 30\,\text{keV}$), which contains $N_{1-\text{e}^-}$ events, we can determine the original number of single electron events N_{true} in the $E_{1-\text{e}^-} = 24\,\text{keV}$ peak.

$$N_{1-\text{e}^-} = N_{\text{true}} \cdot (1 - \varepsilon_{\text{bsc}}) + N_{\text{bsc}}(E_{\text{cutoff}}, E_{1-\text{e}^-}) \tag{5.18}$$

$$N_{\text{true}} = \frac{N_{1-\text{e}^-}}{1 - \frac{d\varepsilon_{\text{bsc}}}{dE} \cdot E_{\text{cutoff}}} \tag{5.19}$$

This does not account for two-electron events which both scattered and only deposited energy equivalent to a single-electron event. These events are not included because of the low probability of such an occurrence ($< 3\%$), with the additional low probability of the total energy deposited to be less than that of a single electron event (an $\approx 25\%$ chance), adding to this the even smaller likelihood of two-electron events.

The calculation of the number of electrons in the higher-order peaks $N_{\geq 2-\text{e}^-}$ is straightforward: every event with an energy deposition of E_{i} above a minimum multiple event energy $E_{min} = 30\,\text{keV}$ is multipled by the energy deposition, and the results are totaled. The total is then normalized by dividing by $E_{1-\text{e}^-} = 24\,\text{keV}$ in order to arrive at the electron count, thus ensuring that events in the $2e^-$ peak count as two electrons, events in $3e^-$ as three, etc:

$$N_{\geq 2-\text{e}^-} = \frac{\sum_{i=0}^{N} E_{\text{i}}}{E_{1-\text{e}^-}} \tag{5.20}$$

As long as the electron peaks are described by a symmetrical distribution, this approach is valid.

This results in a total secondary electron count of:

$$N_{\text{e}^-} = N_{1-\text{e}^-} + N_{\geq 2-\text{e}^-} \tag{5.21}$$

N_{μ} is determined by taking the original number of recorded events N_{μ^*}, and removing the number of events which were cut due to high background noise levels N_{noise} as well as the events removed due to electron discharge events $N_{\text{discharge}}$.

$$N_{\mu} = N_{\mu-Events} - N_{\text{noise}} - N_{\text{discharge}} \tag{5.22}$$

5.3. Results

In this section the results of all the measurement runs are presented, as well as the conclusions which we derived from these. More detailed information on Runs 2 to 9 is available in appendix A.

	Run 1	Run 2+3	Run 4+5	Run 6+7	Run 8	Run 9
Average Angle β_{Avg} ($\pm 1^\circ$)	112.5°	133.2°	66.5°	44.3°	23.9°	124.8°
First paddle X offset (mm)	50 ± 0.5	110 ± 0.5	-50 ± 0.5	-110 ± 0.5	30 ± 0.5	80 ± 0.5
First paddle orientation	L	L	L	L	V	L
Second paddle X offset (mm)	-45 ± 0.5	-85 ± 0.5	50 ± 0.5	100 ± 0.5	100 ± 0.5	-80 ± 0.5
Second paddle orientation	C	C	L	L	V	L
N_μ	15365	33179	59458	34513	125666	70026
N_{μ^*}	15365	33119	59458	34513	125666	70018
Events with secondaries	101	233	467	292	228	761
N_{e^-}	147±10.0%	332±6.6%	717±4.6%	401±5.9%	356±6.6%	1111±3.6%
$\varepsilon_{\text{Setup}}(\pm 1\%)$	42.7%	82.9%	40.1%	87.8%	24.3%	74.8%
$Y_{\mu-\text{SE}}$	2.28%	1.21%	3.02%	1.33%	1.16%	1.74%
$Y_{\mu-\text{SE}-\text{Abs}}$	0.87%	0.83%	1.20%	0.95%	1.06%	0.99%

Table 5.1.: Results of the Münster Muon Experiment. The paddles were either placed **L**engthwise with the 100-mm-side parallel to the flightpath, **C**rosswise with the 70-mm-side parallel, or, in the case of Run 8 both paddles were placed **V**ertically, parallel to the electrode's surface (see Fig. 5.10 for example placements). For all other runs, the first paddle was located above the electrode and the second paddle below. The errors for N_{e^-} propagates to $Y_{\mu-\text{SE}}$ and $Y_{\mu-\text{SE}-\text{Abs}}$.

We assume a total systematic error in the individual emission rates of $\pm 0.5\%$, which includes the uncertanties in the transmission function due to the charge distribution of the isolator tube and slight offsets in the ring electrode and detector placements, the modulation of the incoming muon's angular spectrum due to shielding by the building, and the uncertainties in the muon hit distribution due to the ± 0.5mm error inherent in the muon paddle positioning. An additional error in the resulting average rate due to factors which would affect all runs equally, such as the surface consistancy of the electrode, cannot be explicitly determined.

The results show that the secondary electron rate is dependent on the incidence angle of the muon, as was initially suspected. The electron rate decreases as the angle approaches the electrode normal, as is the case for the angular dependence of secondary electrons ejected by electrons (see [Reimer]). Also, the secondary electron rate is independent of whether the muons enter the surface, or are exiting from the surface, as can be seen by comparing Run 1 with Runs 4 + 5, or Runs 2 + 3 with Runs 6 + 7; this behavior is also similar to that of low-energy electron-induced secondaries. Run 9 was conducted with paddles positions between those used in Runs 4 + 5, and Runs 6 + 7.

Assuming that all electrons created within a layer with a given depth can reach the surface of the electrode we have to correct for the different path lengths of the muons in this layer, caused by

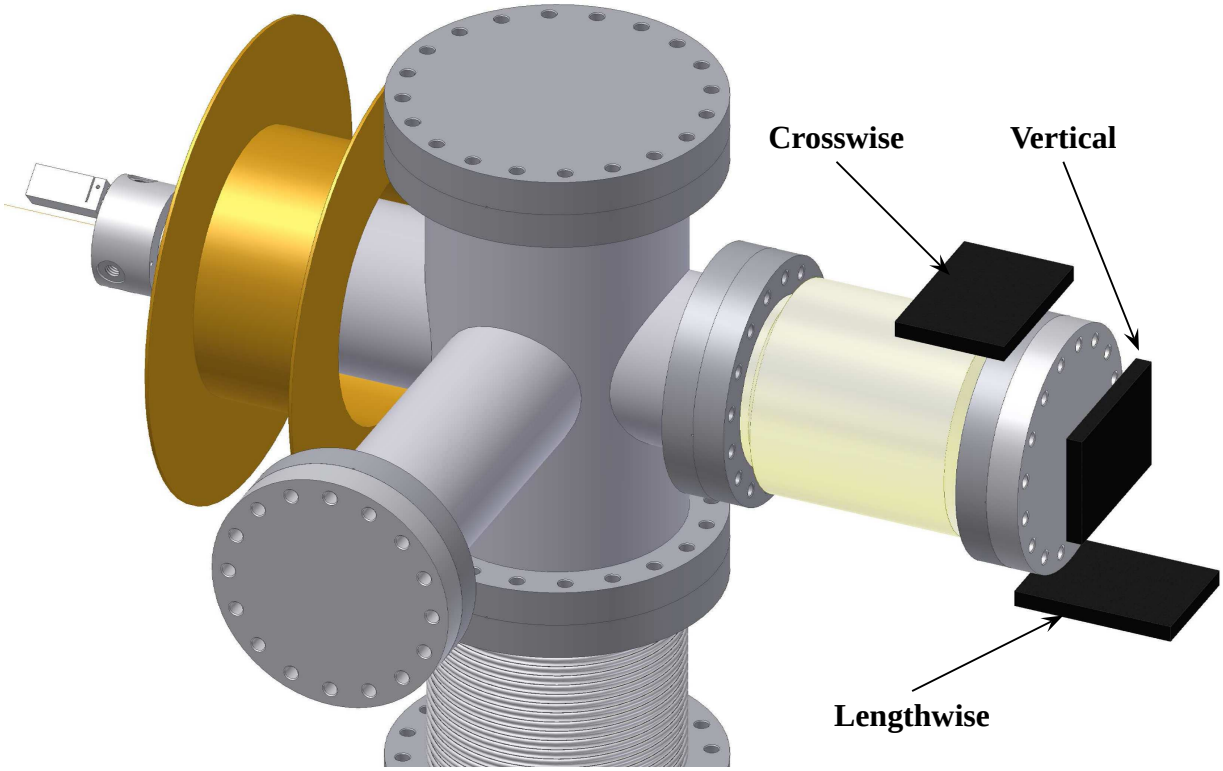

Figure 5.10.: The three different types of muon paddle orientations which were used during the different runs are shown.

their varying incident angles. The travel length in this surface layer can be calculated as follows, normalized to 1 for $\beta = 0$:

$$L(\beta) = \frac{1}{\cos(\beta)} \tag{5.23}$$

with β being the angle between the electrode normal and the average incident muon angle.

In order to test this thesis, L was calculated for each run, and was used to weigh $Y_{\mu-\mathrm{SE}}$, which resulted in the emission rate for orthogonal incidence $Y_{\mu-\mathrm{SE}-\mathrm{Abs}}$.

$$Y_{\mu-\mathrm{SE}-\mathrm{Abs}} = \frac{Y_{\mu-\mathrm{SE}}(\beta)}{L(\beta)} \tag{5.24}$$

This results in a secondary electron rate which remains constant for all our datapoints. Therefore we conclude that the secondary electron rate is constant in all directions, and the measured rate only depends on the number of electrons which reach the surface and are ejected. The angular

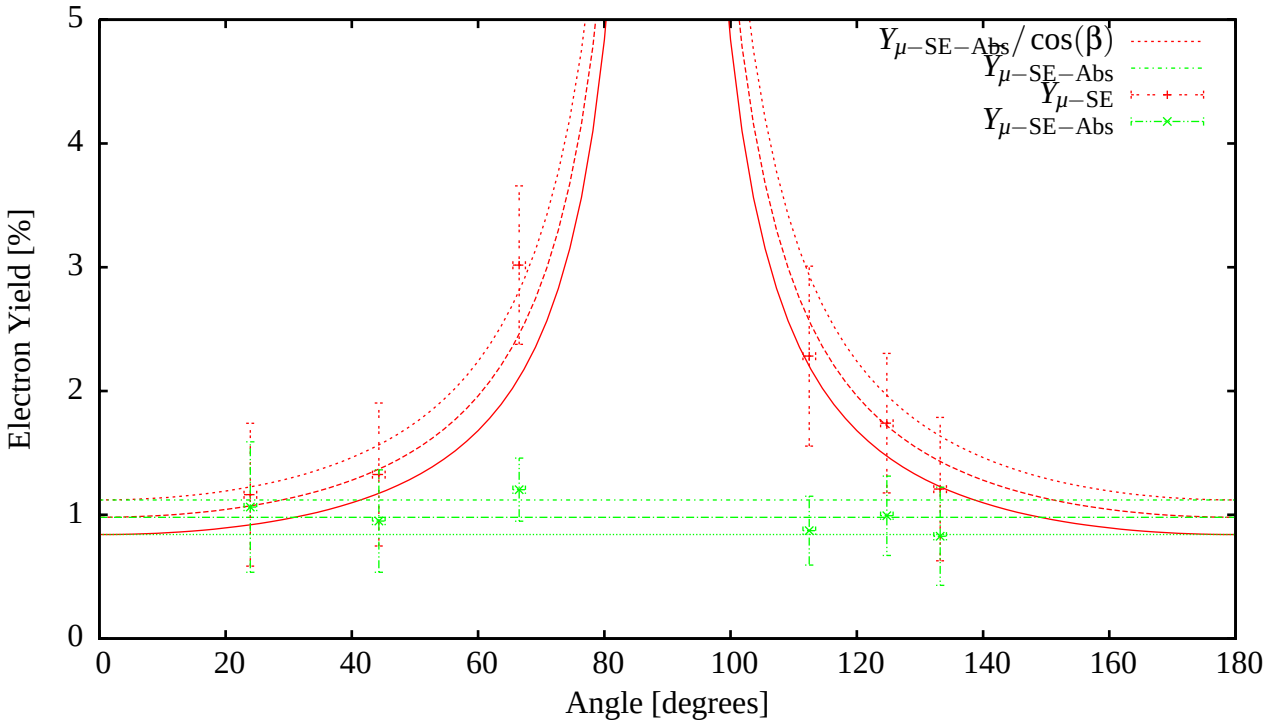

Figure 5.11.: Angular dependence of $Y_{\mu-\mathrm{SE}}$. Both the raw datapoints as well as the normalized datapoints are shown, along as $Y_{\mu-\mathrm{SE}}(\beta)$ using $\overline{Y}_{\mu-\mathrm{SE}-\mathrm{Abs}} = 0.98 \pm .14\%$.

dependence of the low-energy secondary electron yield is:

$$Y_{\mu-\mathrm{SE}}(\beta) = \frac{\overline{Y}_{\mu-\mathrm{SE}-\mathrm{Abs}}}{\cos(\beta)} \tag{5.25}$$

$$N_{\mathrm{SE}}(\beta) = N_{\mu} \cdot \frac{\overline{Y}_{\mu-\mathrm{SE}-\mathrm{Abs}}}{\cos(\beta)} \tag{5.26}$$

with $\overline{Y}_{\mu-\mathrm{SE}-\mathrm{Abs}}$ referring to the emission probability for a muon with an incident angle of $\beta = 0°$. Using the recorded data results in $\overline{Y}_{\mu-\mathrm{SE}-\mathrm{Abs}} = 0.98 \pm .14\%$.

The results of the initial test run, namely a secondary electron emission rate of less than $2 \pm 5\%$, while marred by high noise levels, are consistent with these results. In addition, using the final $Y_{\mu-\mathrm{SE}}$ value to estimate the muon-electron coincidence rate expected with the setup used in Mainz, verifies that the lack of coincidences was the result of a lower than expected emission factor $Y_{\mu-\mathrm{SE}}$.

We conclude that the secondary electrons which were detected have an initial energy which is significantly smaller than the acceleration energy, due to the existence of discrete single-, two-, three-, etc. electron peaks in the detected energy spectrum. In order to determine the secondary energy more precisely, the energy difference between the single- and two-electron peak is compared with the same difference in a background measurement. This energy difference is equivalent to the average starting energy of a single secondary electron. During normal discharge events such as those detected in the background run the initial electron energy is negligible, therefore any difference is solely caused by the higher initial energy of muon induced secondaries.

The last run, Run 9, was run for about 5 weeks, yielding the highest statistics. This allows us to determine the number of electrons in the single- and two- e^- peaks with high accuracy and the number in the $3-e^-$ peak with low accuracy, as well as the locations of these peaks in the energy spectrum. A background measurement was run directly after stopping the data taking of Run 9, therefore this background run has the exact same settings and most importantly the acceleration voltage is identical to Run 9. After locating the peaks in this background spectrum, the energy differences were also determined; these were compared to the differences determined from the Run 9 data. The differences in peak locations were 22.71 ± 0.37 keV and 23.05 ± 0.86 keV for the background run, and 22.21 ± 0.75 keV as well as 24.4 ± 2.1 keV for Run 9. This verifies the low-energy nature of the secondary electrons detected, with the energy differences overlapping within their errors, the secondary electrons possess an energy of under a few hundred eV.

According to [Reimer], the secondaries ejected by the passage of electrons through metals exhibit a peak in the energy spectrum at 16 eV, it is very likely that the muon induced secondaries also peak here.

The secondary electron yield measured during Run 9 was $Y_{\mu-\mathrm{SE}} = 1.80\%$. If the probability of secondary electron creation is constant along the flight path of the muons, the number of events with two or more secondary electrons should follow the Poisson statistical distribution; this would lead to a two-electron peak which is 1.8% of the size of the single-electron peak. However, the data recorded during Run 9 shows that the higher-order peaks are much more prevalent; when analyzing this, a $23 \pm 8\%$ probability was determined for the creation of a secondary electron, which subsequently exits the electrode and then enters the vacuum. Due to the much larger probability of higher-order events, we conclude that the actual ejection of electrons takes place via a two-step process: an initial process takes place with a low probability ($\mathcal{O}(P) = 10\%$), continuously creating the electrons which are ultimately detected in this experiment, these latter electrons having the larger probability of exiting the electrode.

This means that the actual number of low-energy background electrons directly originating from cosmic muons in the KATRIN Experiment's main spectrometer is about 50 times lower than previously thought. As a consequence, the role of other background factors such as the gamma background due to radioactive decay and high-energy electrons becomes a much more dominant factor in the total background rate.

CHAPTER 6

CONCLUSIONS AND OUTLOOK

We have determined the expected count rate of background electrons which are induced by the passage of cosmic muons through the main spectrometer of the KATRIN Experiment, via a GEANT4 based simulation (SIKatrin). For these simulations, it was necessary to determine the angular dependent low-energy secondary electron yield $\overline{Y}_{\mu-\mathrm{SE}-\mathrm{Abs}}$. This was done in a dedicated experiment conducted over the course of this thesis which followed initial measurements conducted at the spectrometer of the Mainz Neutrino Mass Experiment. For the analysis of the recorded data, a program was written; this was used both to analyze the data recorded during the Muon experiments as well as the data recorded during other experiments conducted with the same DAQ system (see [Val09, Str09]).

The determined secondary electron yield, $\overline{Y}_{\mu-\mathrm{SE}-\mathrm{Abs}} = 0.98 \pm .14\%$ for $\beta = 0^\circ$, is 100-times smaller than expected. This low yield explains the lack of events with secondaries in the data

recorded in Mainz. Additionally, the angular dependence of this yield was determined, namely $Y_{\mu-\mathrm{SE}-\mathrm{Abs}}(\beta) = \overline{Y}_{\mu-\mathrm{SE}-\mathrm{Abs}} \cdot \frac{1}{\cos\beta}$, as well as a basic understanding of the ejection process. This process is a two-step process with a low chance of the initial process taking place close enough to the surface of the material to allow some of the large number of secondary electrons created during the second step of the process to exit the material.

However, we had chosen to forgo a determination of the energy spectrum of these secondaries in order to ensure a precise measurement of the total low energy count rate. This energy dependence is an important input quality required to increase the accuracy of future simulations. Interesting results might be obtained by conducting a new series of measurements at Mainz, or extending the setup in Münster to allow such measurements. Using this energy spectrum, fully electromagnetically tracked simulations could be conducted which would determine the shielding factor of the wire electrode, the background count rate which exits the spectrometer, etc. The fully-tracked simulations could also determine whether "hotspots" or other interesting features exist in the origin distribution of secondary electrons.

An additional interesting question is whether the angular dependence of the two-step secondary electron production process continues for angles close to 90°, or whether the behavior of the two-step process changes for these steep angles due to the nature of the primary process. Comparing a run with high statistics of low-incident-angle muons with one solely comprised of muons with steep angles should help clarify this question. The vacuum teststand constructed for these muon measurements has already proven to be a versatile setup for various small experiments, and will continue to be used in the future.

Using these results, simulations were conducted using $\approx 10^{11}$ primary particles. We determined the background count rate of the low-energy secondary electrons for two scenarios: A, the secondary electrons having less than 200 eV initial energy, and B, the secondaries having less than 25 eV energy. These result in upper limits for the total background rates of 174 ± 9 Hz and 59 ± 30 Hz, respectively, as well as a shielding factor for the inner electrode system of 12 ± 1.2 and 33 ± 16, respectively. In the future, the errors induced by the employed estimated reduction factors, which are currently based on the geometry, may be reduced by running simulations with microscopic tracking. Details on the estimates used as well as the various backgrounds of the electrode components may be found in section 2.4.

In order to increase the precision of the geometry while maintaining accurate tracking, several electromagnetic field maps could be created, each with a pair of adjacent combs using the highly detailed comb model and the other combs using the simpler comb model, thereby limiting the impact of the additional surfaces on CPU and memory usage. Then, when tracking electrons, the field map used could be varied depending on the position of the electron, always ensuring the combs nearest the electron are using the high-precision models. This would allow the SIKatrin simulation to load a geometry file which uses the newer comb model for all combs.

APPENDIX A

MUON RUN RESULTS

A.0.1. Run 1

For Run 1 figures please refer to section 5.2.4.

A.1. Run 2 and 3

For the next run, we increased the horizontal separation of the two muon paddles, thus selecting larger angles. While the larger angle leads to a slightly diminished countrate, the increased distance between these paddles was the primary factor in the reduction. The initial run using this

configuration had to be restarted as we ran out of storage space on the DAQ PC. We also had to reject a number of events taken during Run3; while we were able to pinpoint the time of the noise increase, we were unable to correlate this with any activities in the laboratory. The noiselevel was also slightly higher after this noiseband. During this run the pulser was removed from the setup.

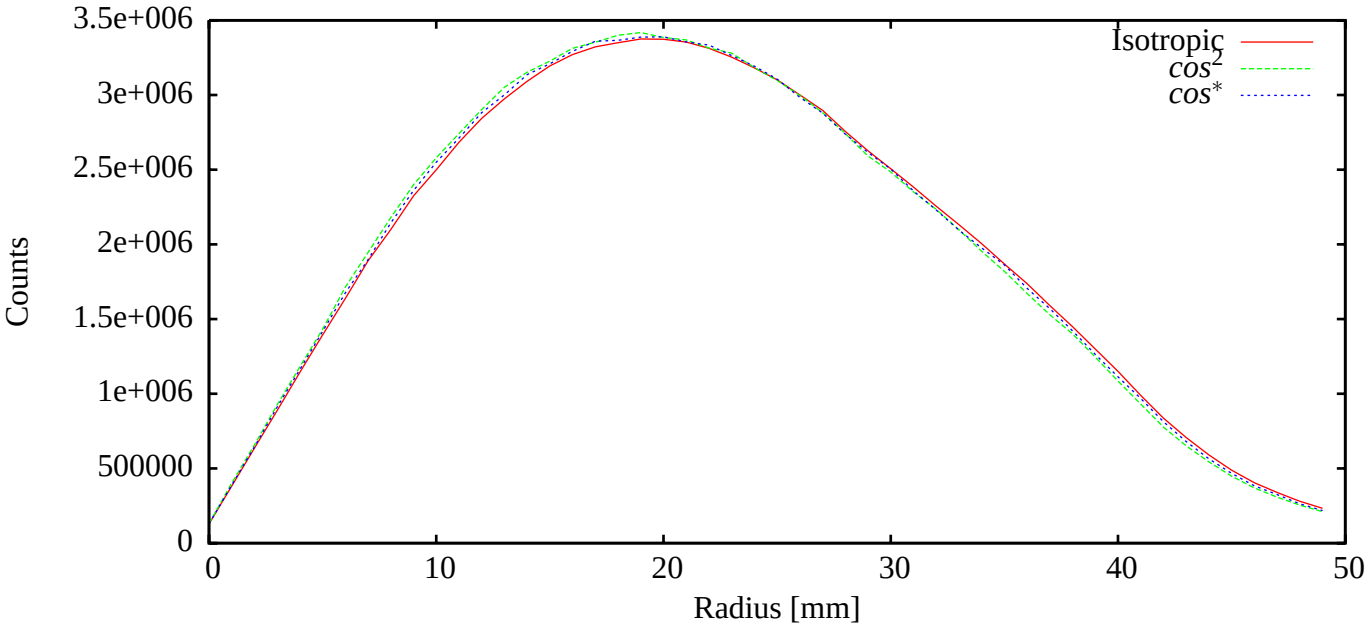

Figure A.1.: Radial incident probability distribution of detected muon events for three various primary muon distributions.

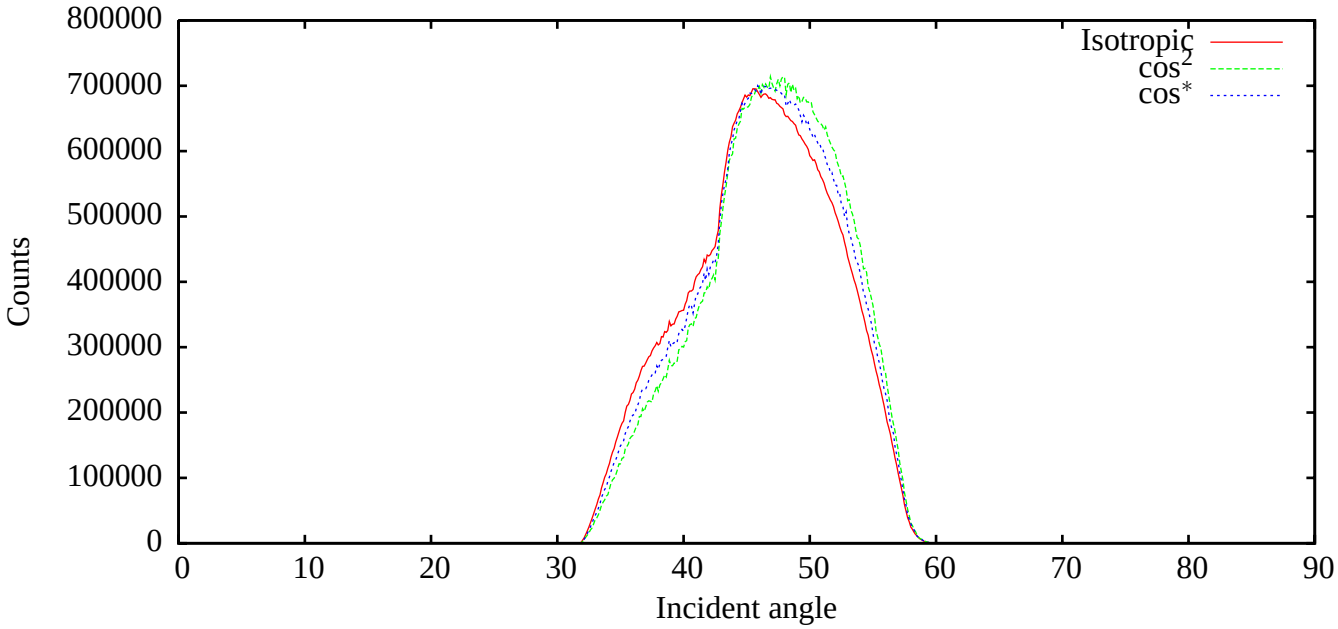

Figure A.2.: Angular incident probability distribution of detected muon events for three various primary muon distributions during Runs 2+3.

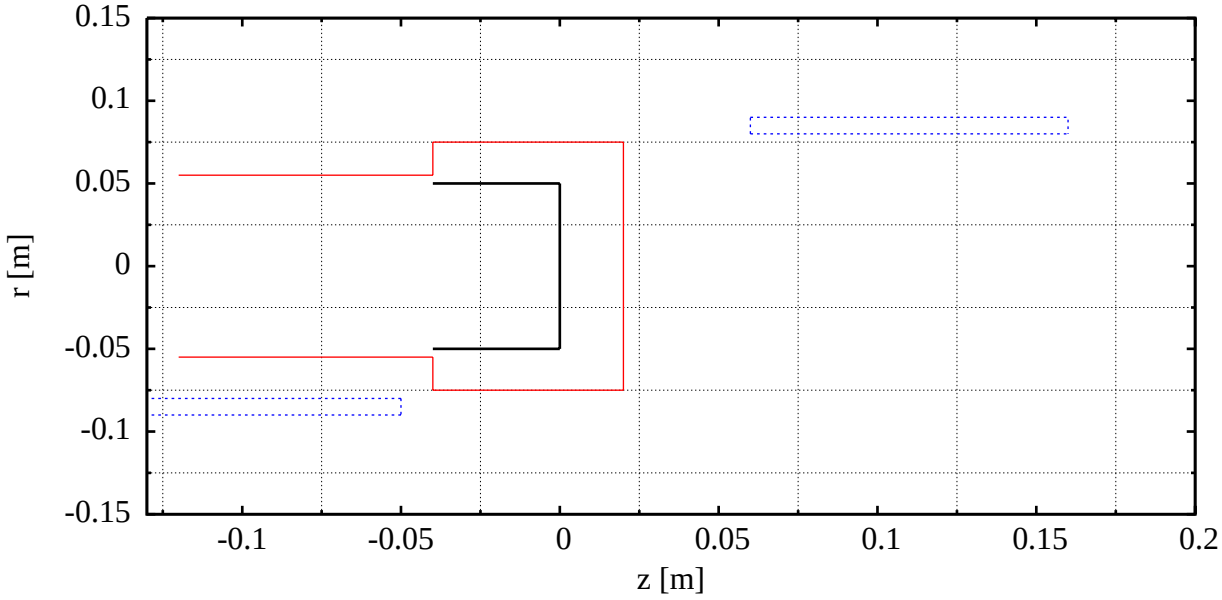

Figure A.3.: The paddle configuration as used in Runs 2+3. The bottom paddle was arranged lengthwise.

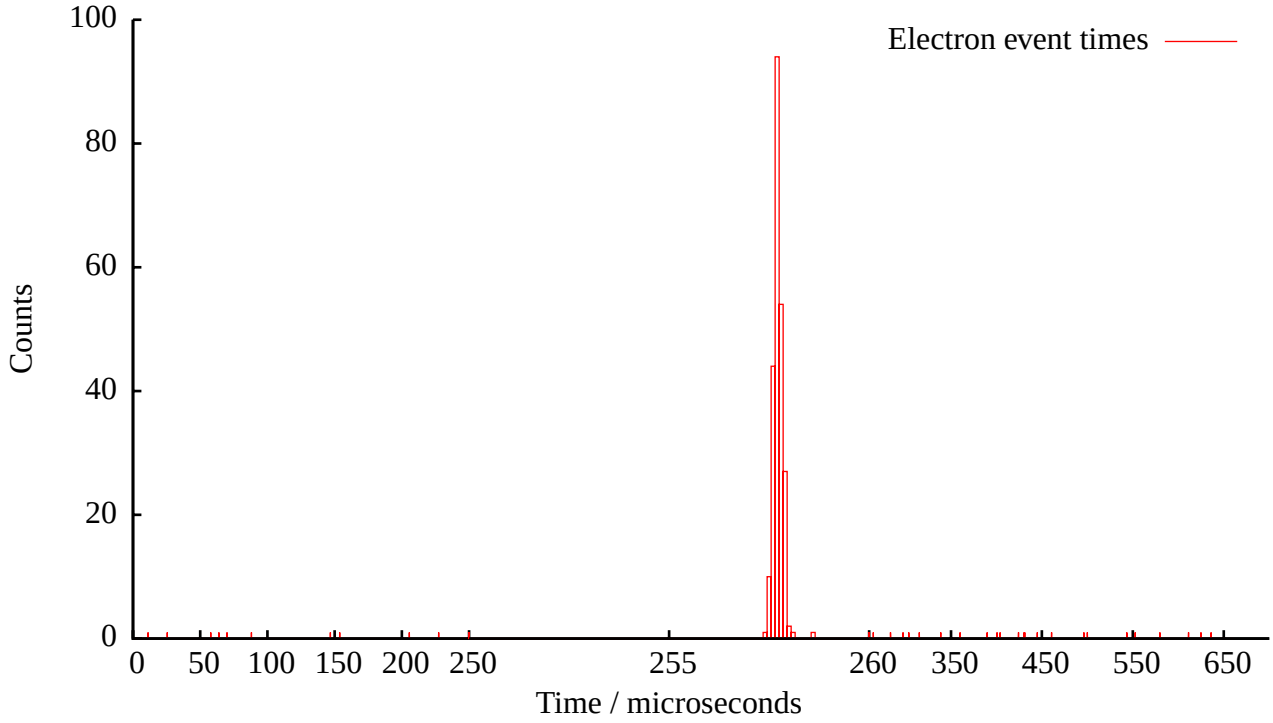

Figure A.4.: Binned electron arrival times of Run2+3. The bin-width is 0.1 microseconds.

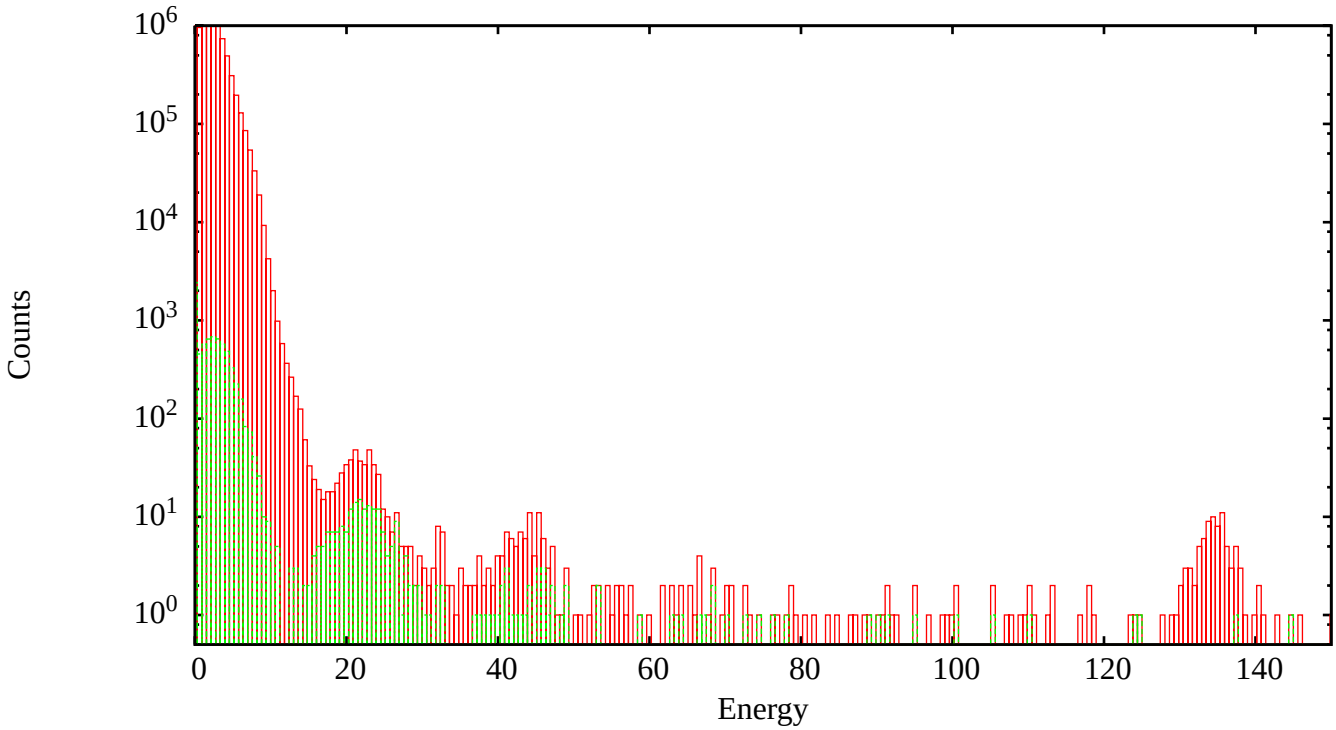

Figure A.5.: The total energy spectrum of all events taken during the second and third run, as well as the filtered spectrum of events which occured in a window of a microsecond around the trigger pulse. The pulser peak can be readily identified around 135keV, as well as the single electron peak.

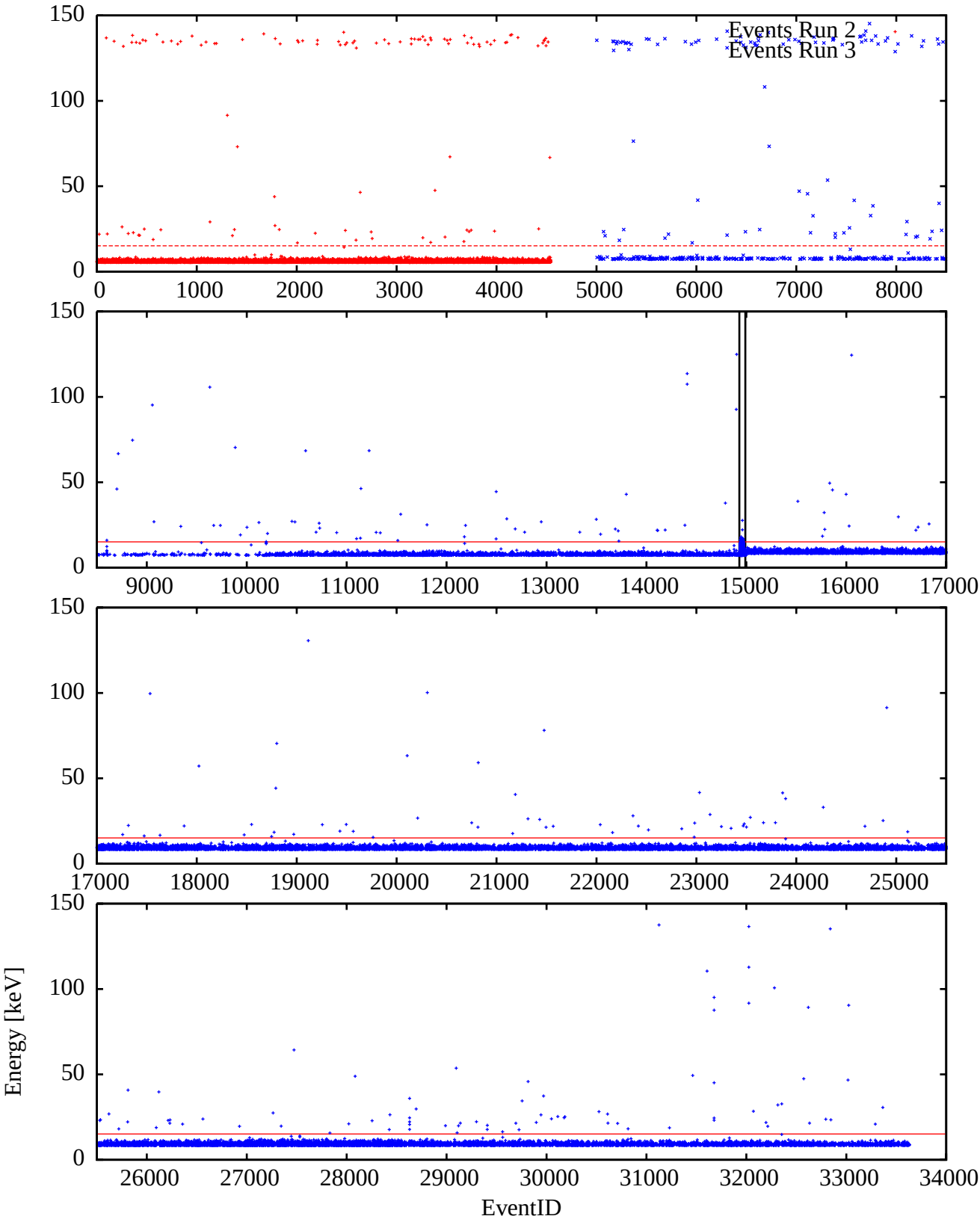

Figure A.6.: The events of both run two and three are shown, in order to show the changing noise level. Also shown is the noise cutoff as well as the rejected events near event 15000, due to a noise spike.

A.2. Run 4 and 5

In Runs 4+5 the top and bottom paddles were located on the opposite sides of the electrode compared to Run 1.

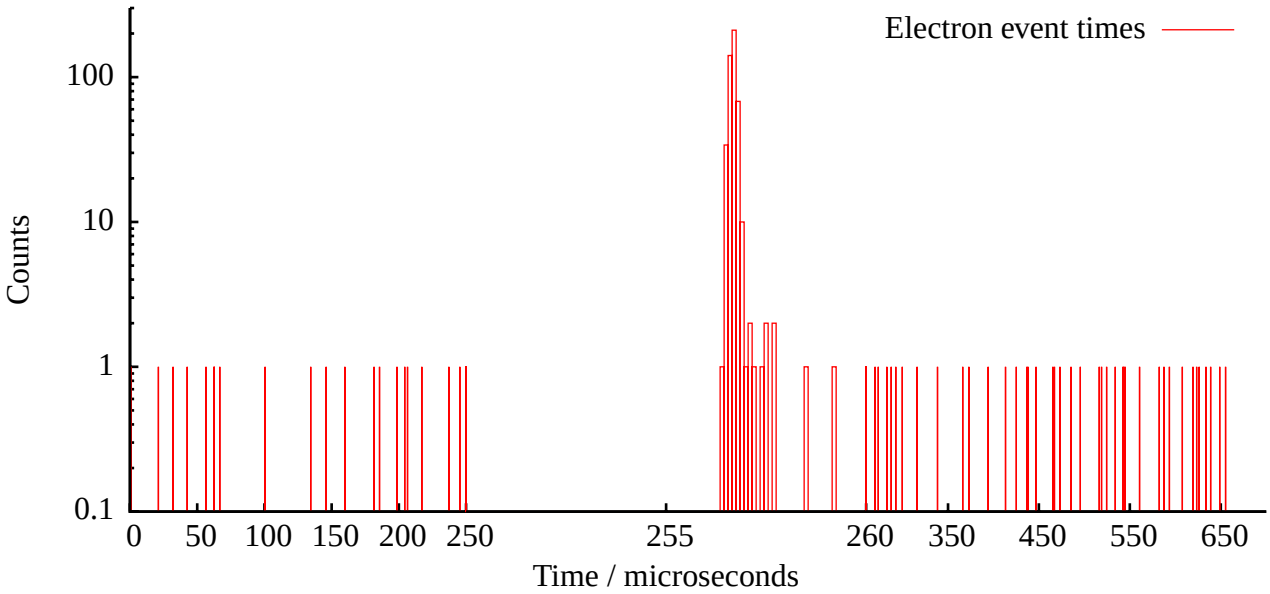

Figure A.7.: Binned electron arrival times of Runs 4+5. The bin-width is 0.1 microseconds. A uniform background is visible along with the coincidence peak.

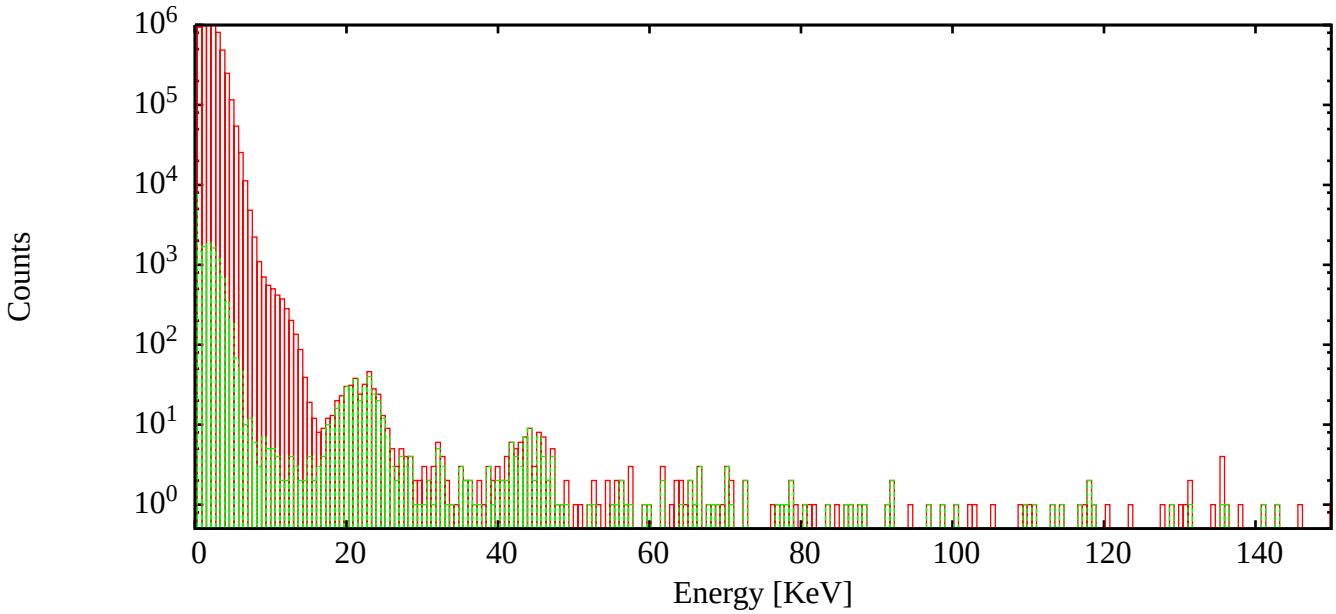

Figure A.8.: Shown is the total energy spectrum of all events taken during the fourth and fifth run, as well as the filtered spectrum of events which occured in a window of a microsecond around the trigger pulse. Both the single electron peak as well as higher order peaks are visible.

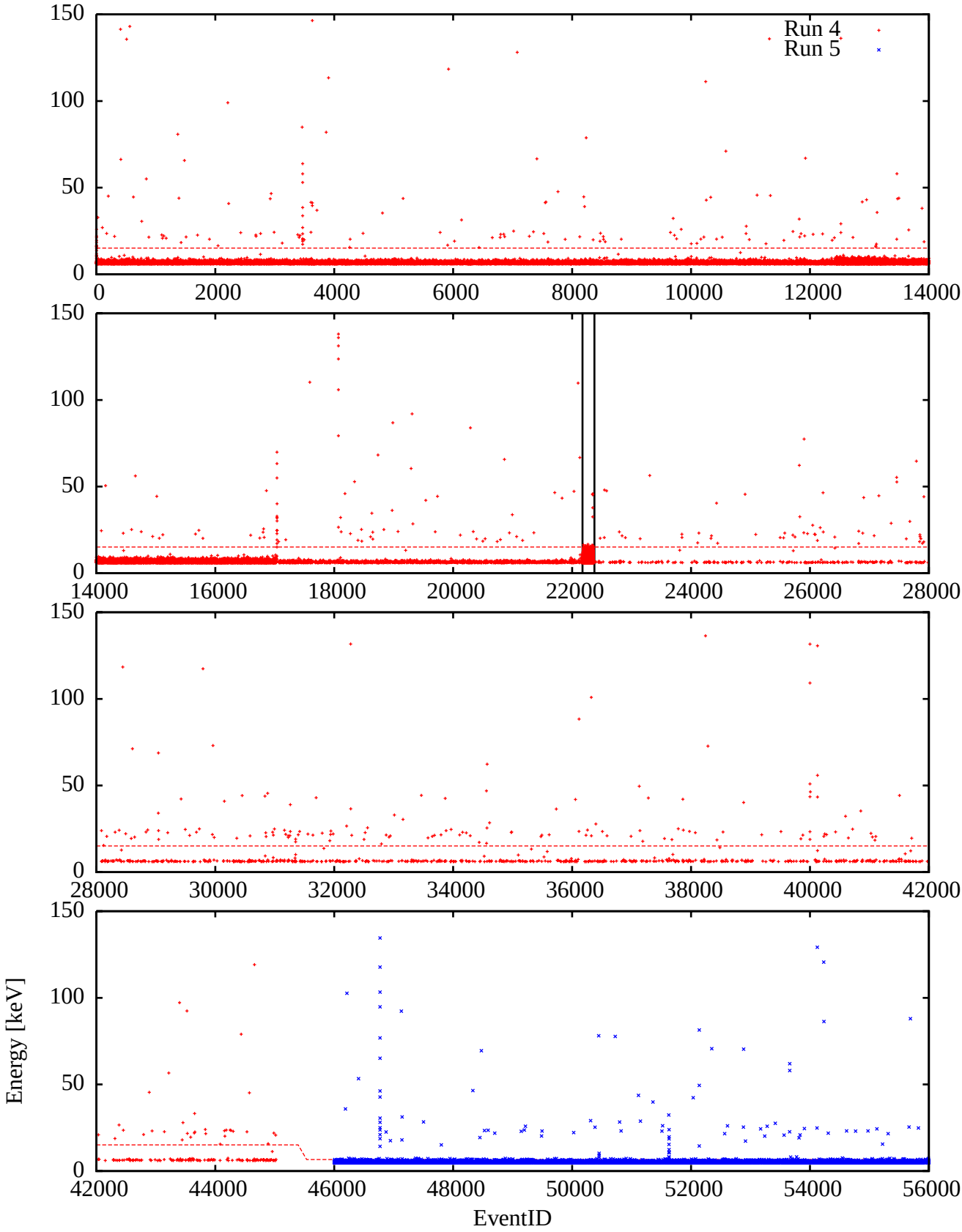

Figure A.9.: Event energy vs event index, Runs 4+5. Several discharge events are visible which were subsequently removed, along with a high-noise band near event 22000.

A.3. Run 6 and 7

Runs 6+7 used a similar paddle geometry to Runs4+5, with the same increased spacing as Runs 2+3.

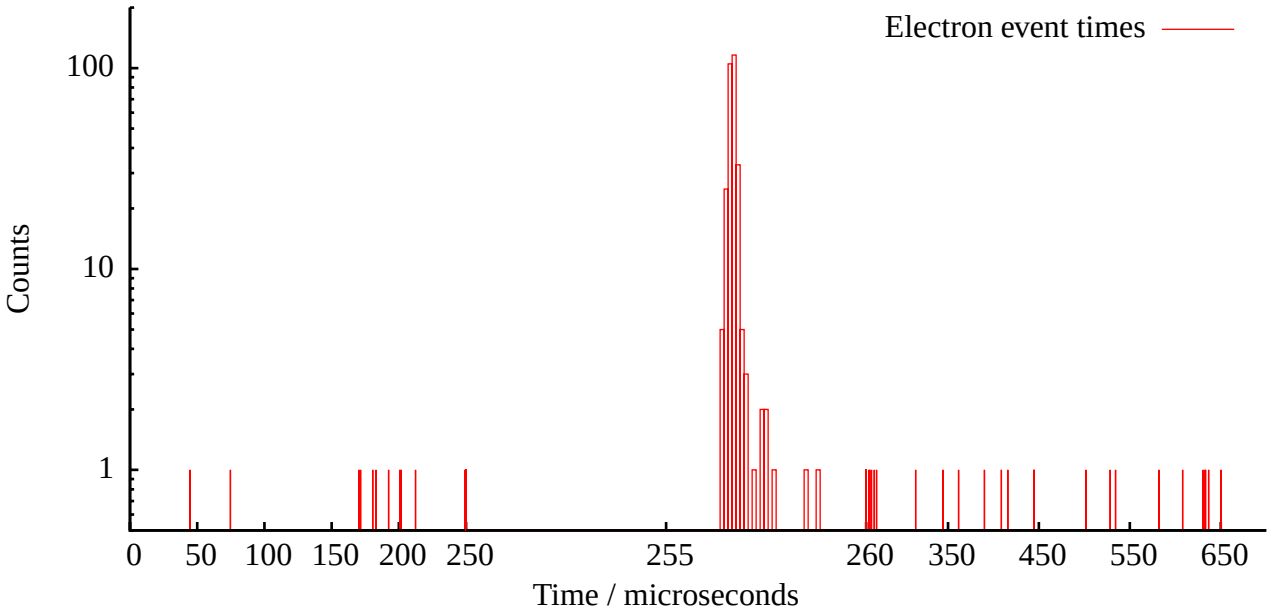

Figure A.10.: Binned electron arrival times of Runs 6+7. The bin-width is 0.1 microseconds.

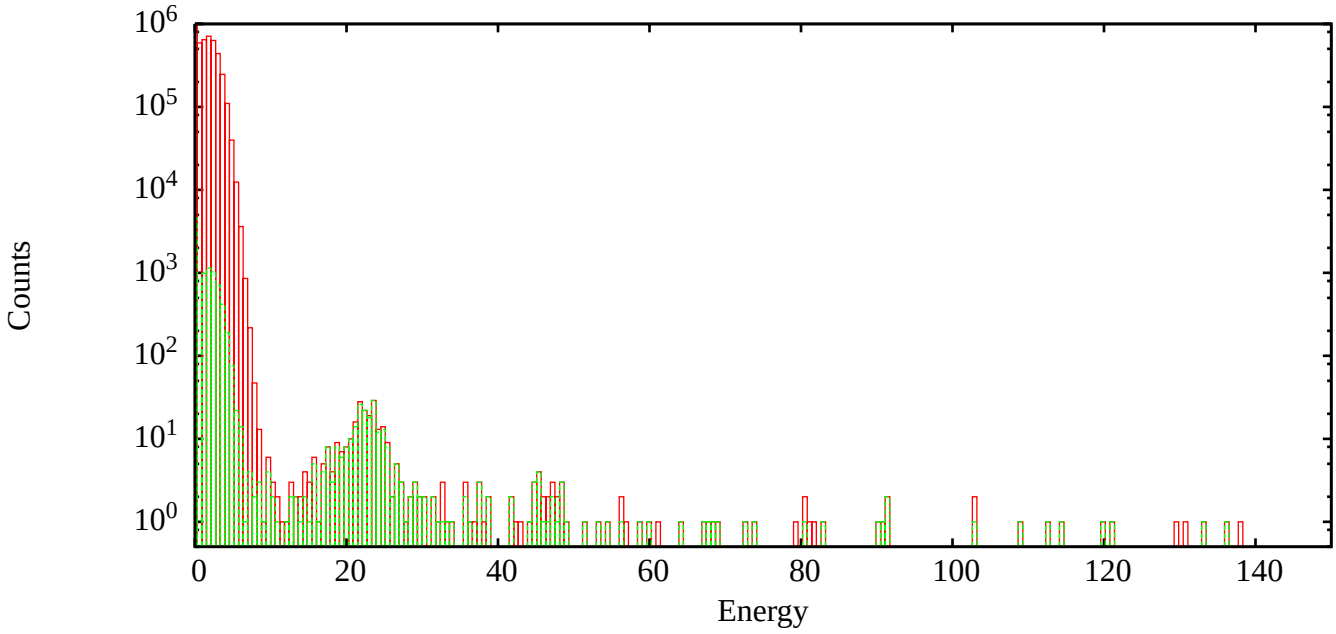

Figure A.11.: Shown is the total energy spectrum of all events taken during Runs 6+7, as well as the filtered spectrum of events which occured in a window of a microsecond around the trigger pulse.

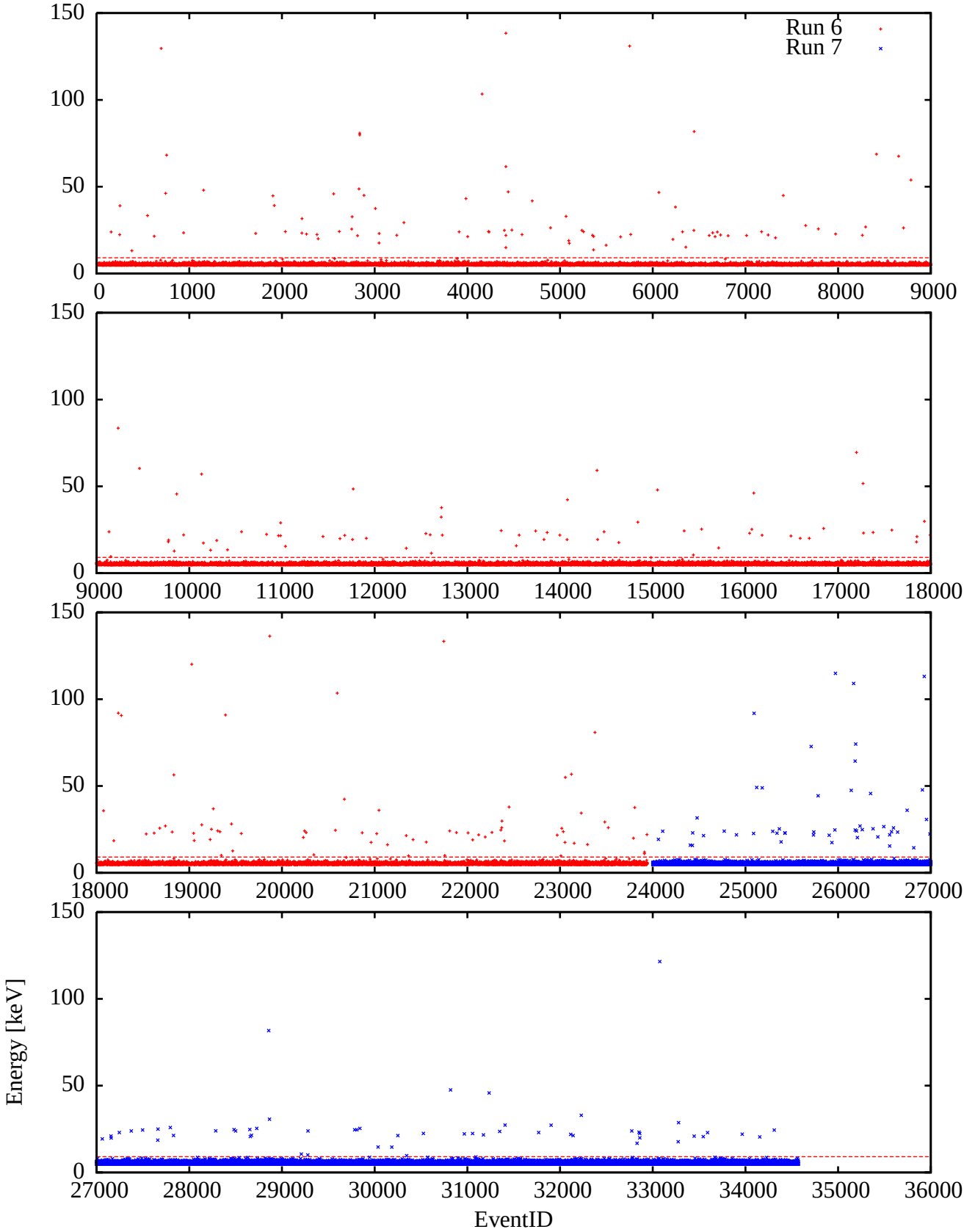

Figure A.12.: Event energy vs event index, Run 6+7

A.4. Run 8

In run 8, we used a similar paddle configuration to the setup in the preliminary Münster measurements, as well as the measurements in Mainz, with both paddles orientated vertically behind the electrode. As we now expected a secondary rate of a few percent, we opted for a larger distance between the two paddles in order to reduce the number of events which would trigger without the muon even striking the electrode; this would reduce the background. Even so, the total event count was much larger than for all the over runs, with over 100K events being recorded, and at the same time the intersection probability was the lowest. This resulted in a significant amount of background events.

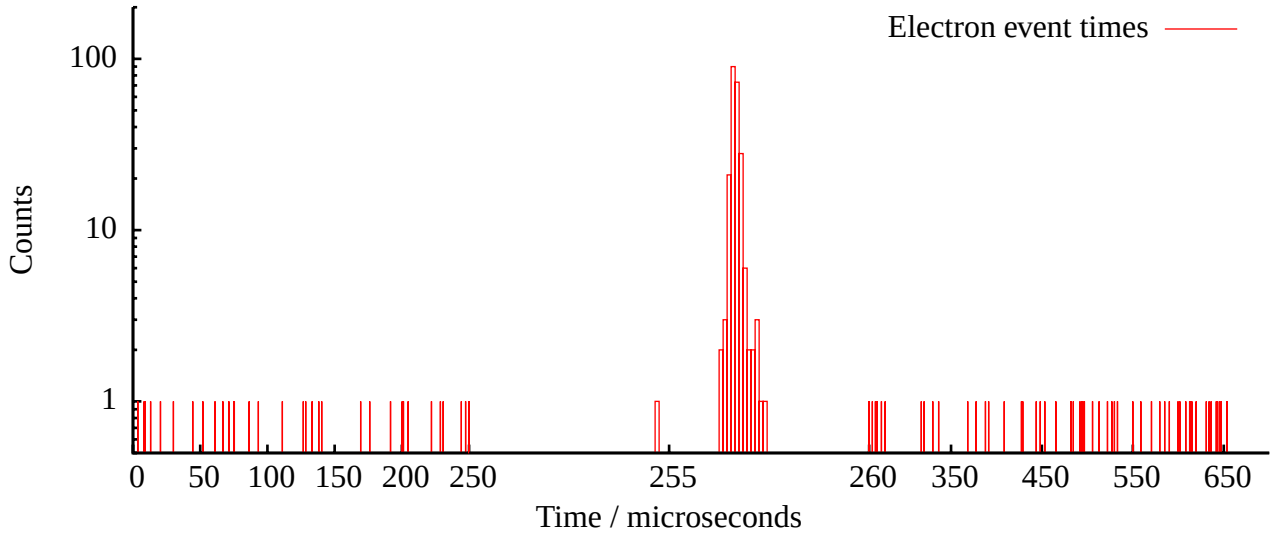

Figure A.13.: Binned electron arrival times of Run 8. Binwidth of 0.1 microseconds.

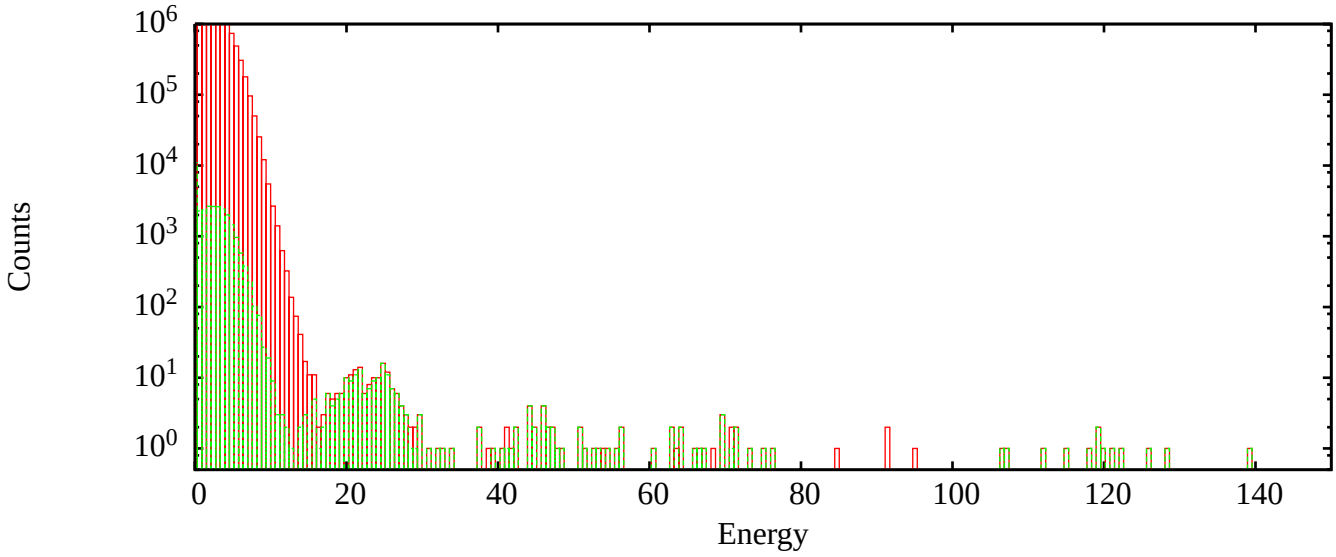

Figure A.14.: Shown is the total energy spectrum of all events taken during Run 8, as well as the filtered spectrum of events which occured in a window of a microsecond around the trigger pulse.

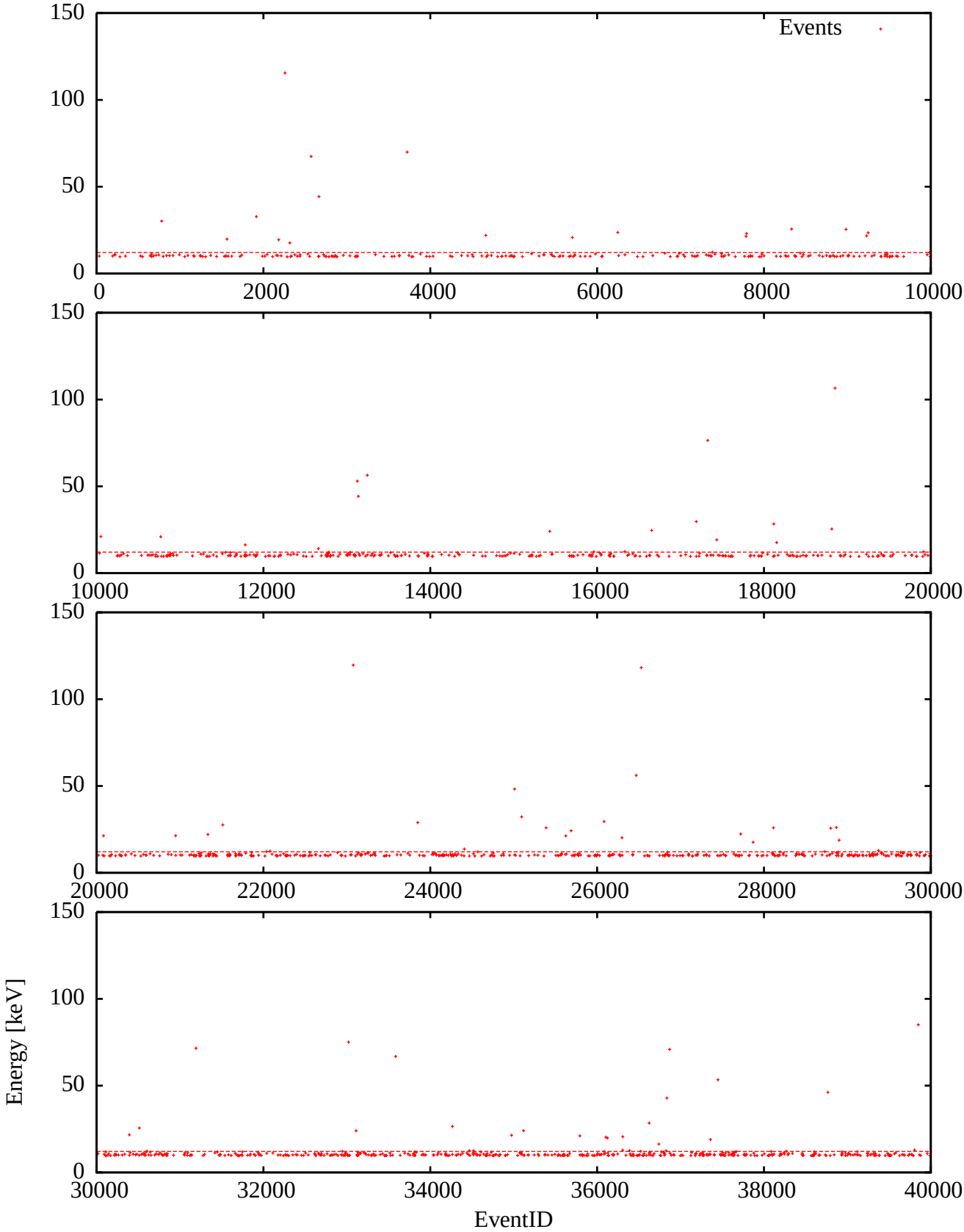

Figure A.15.: Event energy vs event index, Run 8

A.5. Run 9

Since the next experiment planned for the vacuum chamber was delayed, a further angle was setup, in this case an angle was chosen inbetween runs 4+5 and 6+7. This measurement was kept running over the christmas holiday period, with a total measurement time of ≈5 weeks.

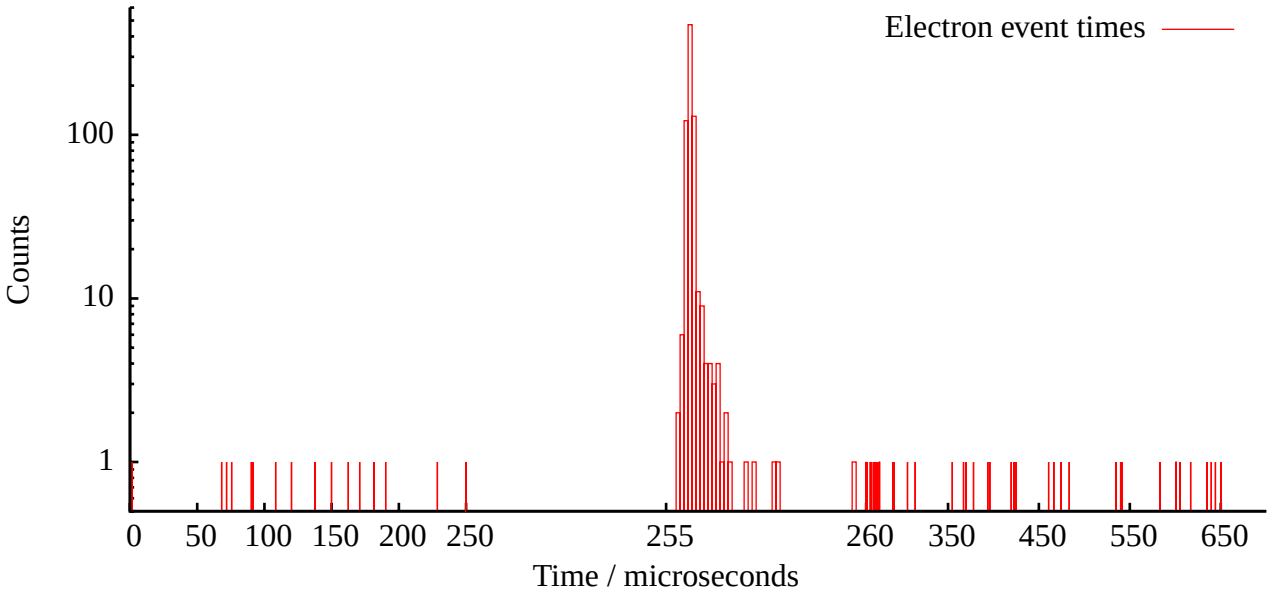

Figure A.16.: Binned electron arrival times of Run 9. The bin-width is 0.1 microseconds.

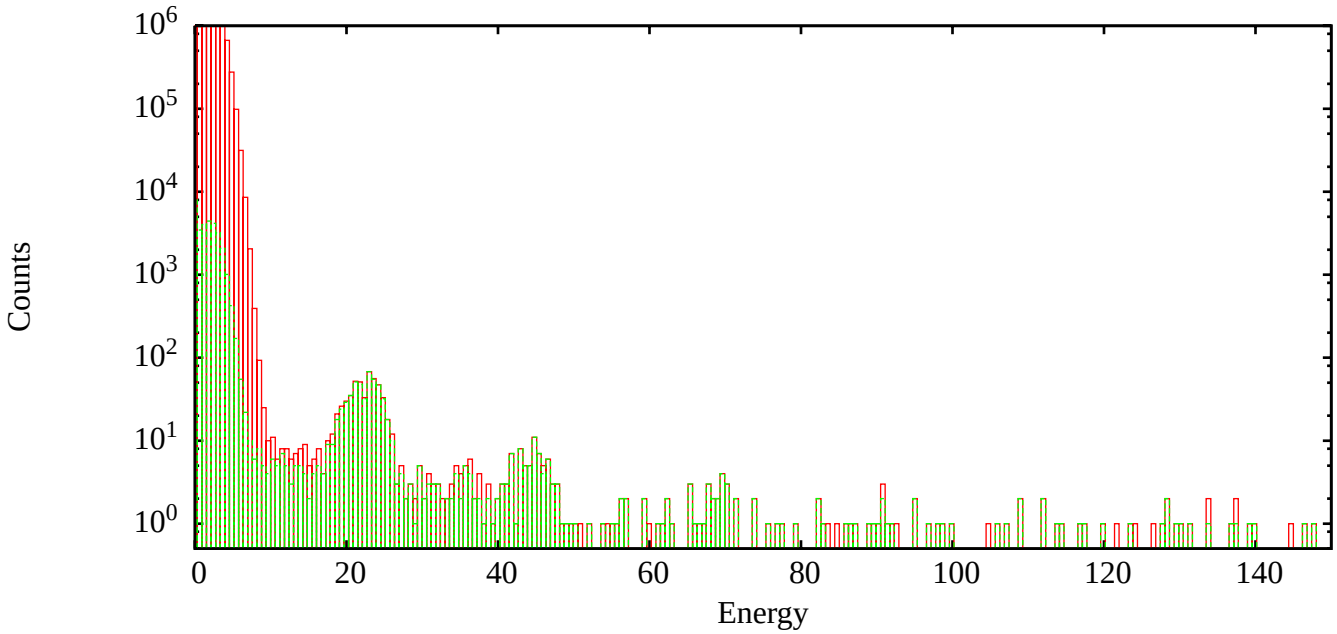

Figure A.17.: Shown is the total energy spectrum of all events taken during Run 9, as well as the filtered spectrum of events which occured in a window of a microsecond around the trigger pulse. Higher order peaks are visible due to the higher event rate.

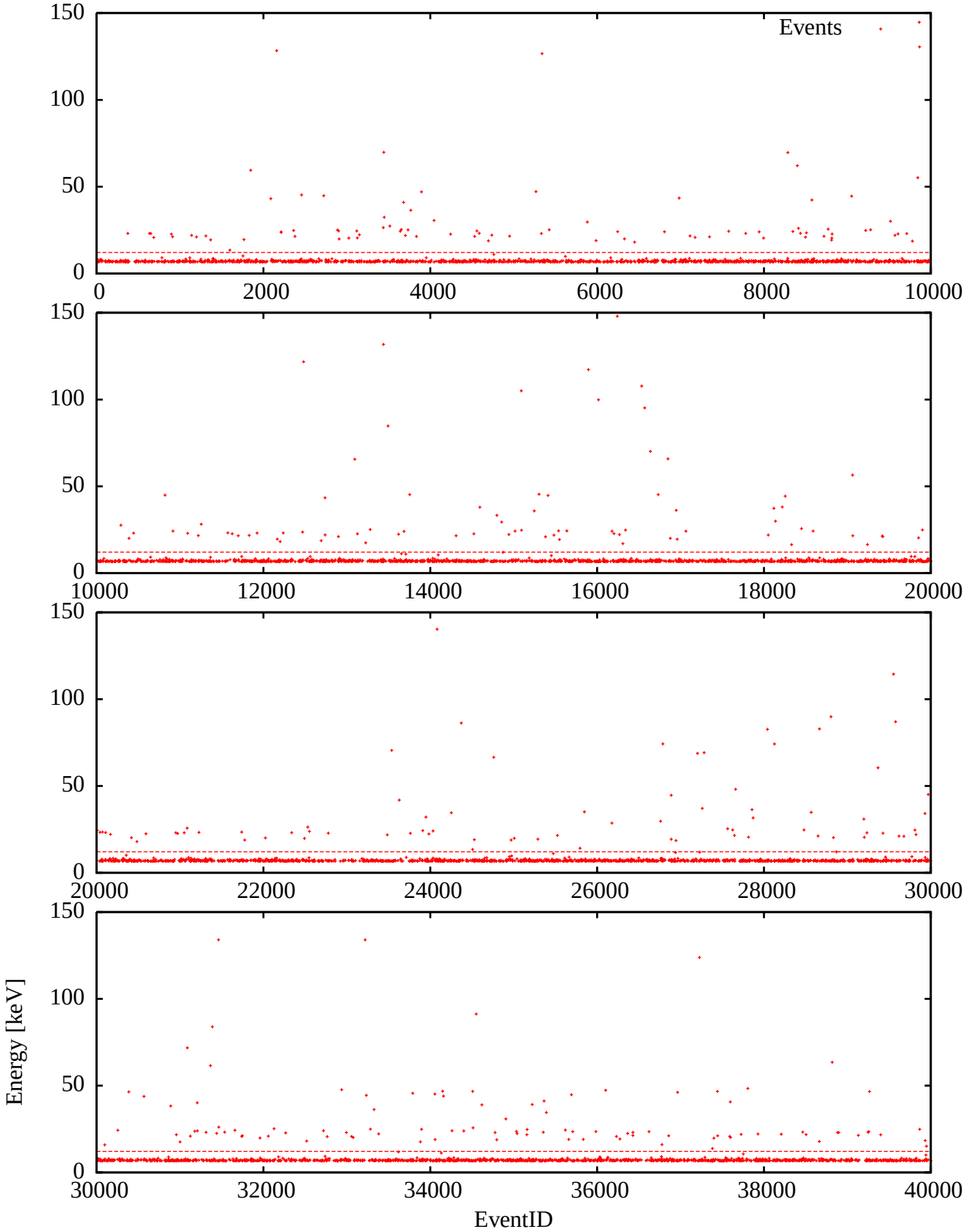

Figure A.18.: Event energy vs event index, Run 9

Appendix B

Sample Analysis Script

The shell script used to analyze Run 1 is reproduced below.

Listing B.1: Analysis script to analyze Run 1

```
echo "analyzing data (Run1) ...."
if [ $2 = "1" ]; then
        /data/henrik/AnalyzeV8/AnalyzeV8 ../RawData/Run1/HenrikNewSetup_Run_120Amps_80Volts_24KV 5
        mv EventTimes.txt ../RawData/Run1/
fi

echo "Making time spectrum..."
#       Kill the noise for the time spectrum
~/Tools/FilterByValue/Filter ../RawData/Run1/EventTimes.txt EventTimes.LowNoise.txt 7 13 0
#       Kill the noise for the time spectrum
~/Tools/FilterByValue/Filter ../RawData/Run1/EventTimes.txt EventTimes.NoNoise.txt 7 22 0

#       Kill the pulser in 2 steps
~/Tools/FilterByValue/Filter EventTimes.NoNoise.txt EventTimes.NoNoise.Upper.txt 7 230 0
~/Tools/FilterByValue/Filter EventTimes.NoNoise.txt EventTimes.NoNoise.Lower.txt 7 200 1
mv EventTimes.NoNoise.Upper.txt EventTimes.NoNoise.txt
cat EventTimes.NoNoise.Lower.txt >> EventTimes.NoNoise.txt
rm EventTimes.NoNoise.Lower.txt


#       Kill the very high energy events
~/Tools/FilterByValue/Filter EventTimes.NoNoise.txt EventTimes.NoNoiseb.txt 7 245.4705882352941176 1
mv EventTimes.NoNoiseb.txt EventTimes.NoNoise.txt

#Remove events with more than 4 electrons
~/Tools/RemoveEvents/RemoveEvents EventTimes.NoNoise.txt EventTimes.NoMultiple.txt 1 4 > NumNoisyEventsIgnored.dat
mv EventTimes.NoMultiple.txt EventTimes.NoNoise.txt

#       Now make time spectrum
~/Tools/BinScatter/Binner EventTimes.NoNoise.txt MainAmp.time.nopulser.txt 9 5 0 66000 10


echo "Making local energy spectrum..."
#       now filter on time cutoffs
~/Tools/FilterByValue/Filter ../RawData/Run1/EventTimes.txt EventTimes.temp.txt 5 25725 0
~/Tools/FilterByValue/Filter EventTimes.temp.txt EventTimes.window.txt 5 25825 1
~/Tools/BinScatter/Binner EventTimes.window.txt MainAmp.EnergyWindow.txt 9 7 0 4000 1
rm EventTimes.temp.txt



echo "Making energy spectrum"
#       Also make the total energy spectrum.
~/Tools/BinScatter/Binner ../RawData/Run1/EventTimes.txt MainAmp.txt 9 7 0 4000 1

if [ $1 = "1" ]; then
        ~/Tools/MuonCoverage/MuonCoverage PaddleLocations.dat 1 MuonCoverage_1_ ~/Tools/AllLowEnergyHits.trans.dat
        ~/Tools/MuonCoverage/MuonCoverage PaddleLocations.dat 2 MuonCoverage_2_ ~/Tools/AllLowEnergyHits.trans.dat
        ~/Tools/MuonCoverage/MuonCoverage PaddleLocations.dat 3 MuonCoverage_3_ ~/Tools/AllLowEnergyHits.trans.dat

        ~/Tools/SumSpectra/Summer  MuonCoverage_1__Radial.dat MuonCoverage_1__Radial.Summed.dat 0
        ~/Tools/SumSpectra/Summer  MuonCoverage_2__Radial.dat MuonCoverage_2__Radial.Summed.dat 0
        ~/Tools/SumSpectra/Summer  MuonCoverage_3__Radial.dat MuonCoverage_3__Radial.Summed.dat 0
fi



~/Tools/FilterByValue/Filter EventTimes.NoNoise.txt EventTimes.temp.txt 5 25725 0
~/Tools/FilterByValue/Filter EventTimes.temp.txt EventTimes.Window.NoNoise.txt 5 25825 1

~/Tools/BinScatter/Binner EventTimes.Window.NoNoise.txt EventsWithEvents.txt 9 1 0 200000 1
echo "Number of events with secondaries." > NumberSecondaryEvents.txt
cat EventsWithEvents.txt | grep -v " 0" | wc -l >> NumberSecondaryEvents.txt
rm EventsWithEvents.txt;

~/Tools/FilterByValue/Filter EventTimes.Window.NoNoise.txt EventTimes.SingleElectrons.dat 7 57.3 1
~/Tools/FilterByValue/Filter EventTimes.Window.NoNoise.txt EventTimes.MultiElectrons.dat 7 57.3 0

echo "Number of single electron peaks located" >> NumberSecondaryEvents.txt
cat EventTimes.SingleElectrons.dat | grep -v "#" | wc -l >> NumberSecondaryEvents.txt

echo "Number of multiple electron peaks located" >> NumberSecondaryEvents.txt
cat EventTimes.MultiElectrons.dat  | grep -v "#" | wc -l >> NumberSecondaryEvents.txt

echo "Total energy in multiple electron peaks, before energy calibration is applied (Requires * (134.4 / 214) / 24)" >>
     NumberSecondaryEvents.txt
~/Tools/CalcEnergy/CalcEnergy EventTimes.MultiElectrons.dat 7 >> NumberSecondaryEvents.txt




mkdir ~/Documents/Diplom/Muons/Run1/
cp EventTimes*.*.txt ~/Documents/Diplom/Muons/Run1/
cp MainAmp*.txt ~/Documents/Diplom/Muons/Run1/
cp MakeMuonGraphs.sh ~/Documents/Diplom/Muons/Run1/
cp MuonCoverage* ~/Documents/Diplom/Muons/Run1/
```

LIST OF FIGURES

LIST OF TABLES

BIBLIOGRAPHY

[Ago03] S. Agostinelli et. al., *G4a simulation toolkit*, Nuclear Instruments and Methods in Physics Research Section A: Accelerators, Spectrometers, Detectors and Associated Equipment, Volume 506, Issue 3, 1 July 2003, Pages 250-303

[All06] J. Allison et.al., *Geant4 developments and applications*, IEEE Transactions on Nuclear Science, Volume: 53, Issue: 1, Part 2 (Feb. 2006)

[Ang04] J. Angrik *et al.*, KATRIN Design Report 2004, FZK Scientific Report 7090, `http://www-ik.fzk.de/katrin`

[Bea80] G. Beamson *et al.*, J. Phys. E: Sci. Instrum. **13** (1980) 64 - 66

[Ben09] S. Benning, diploma thesis in preparation, Westfälische Wilhelms-Universität Münster, 2009

[Bog06] L. N. Bogdanova, M. G. Gavrilov, V. N. Kornoukhov, A. S. Starostin, *Cosmic muon flux at shallow depths underground*, Institute for Theoretical and Experimental Physics, Moscow, Russia
`http://arxiv.org/abs/nucl-ex/0601019`

[Bru97] R. Brun, F. Rademakers: *ROOT - An Object Oriented Data Analysis Framework.* In: Proceedings AIHENP 1996 Workshop, Lausanne 1996, Nucl. Inst. & Meth. in Phys. Res. A **389** 1997 81

[Cor09] T. J. Corona, Master's Thesis: *Tools for Electromagnetic Field Simulation in the KATRIN Experiment*, Massachusetts Institute of Technology, 2009

[Dav94] R. Davis, Prog. Part. Nucl. Phys. **32** (1994) 13; Proc. 13th Intern. Conf. on Neutrino Physics and Astrophysics, Boston, USA, 1988, p. 518, Eds. J. Schneps et al., World Scientific, 1989

[Dav96] R. Davis, Nucl. Phys. **B** (Proc. Suppl.) **48** (1996) 284

[Eng06] Ralph Engel: Ultrahigh-Energy Cosmic Rays, Vortrag, Nijmegen, 2006,
`http://nijmegen06.astro.ru.nl/lectures.shtml`

[Exstrom] Exstrom Laboratories LLC, *Digital Signal Processing*, http://www.exstrom.com/journal/sigproc/

[Fer34] E. Fermi, Z. Phys. **88** (1934) 161 - 177

[Geb07] A. Gebel, *Entwicklung und Aufbau eines Prototypmoduls für die Drahtelektrode des KATRIN Hauptspektrometers*, diploma thesis, Westfälische Wilhelms-Universität Münster, 2007

[Gol01] A. Goldschmidt for the IceCube Collaboration, *The IceCube Detector* , Proceedings of the 27th International Cosmic Ray Conference, Hamburg, Germany, 7-15 August 2001 (HE 2.5 19:36), 1237-1240

[Glü05a] F. Glück et. al., *The neutron decay retardation spectrometer aSPECT: Electromagnetic design and systematic effects*, Eur. Phys. J. **A 23** (2005) 135

[Glü06a] F. Glück, *New electric field calculation program for wire electrodes with support structure*, presentation at the 10th KATRIN collaboration meeting, Bad Liebenzell, March 2006
KATRIN BSCW, 95 General Meetings and Review Panels, 1 Collaboration Meetings, 10. Collaboration Meeting, Parallel Session - A2, 95-TRP-4031-A2-FGlueck.ppt;
F. Glück, private communication, March 2006

[Glü09a] F. Glück, to be published

[Hei09] H. Hein, Diploma Thesis, Institut für Kernphysik, Universität Münster, (vorauss. 2009)

[Hil10] B. Hillen, dissertation in preparation, Inst. f. Kernphysik, Universität Münster (vorauss. 2010)

[Hug08] K.Hugenberg, *Design of the electrode system for the KATRIN main spectrometer*, diploma thesis, Westfälische Wilhelms-Universität Münster, 2008

[Kan78] K. Kanaya and S. Ono, J. Phys. D 11 (1978) 1495

[Kli00] S. I. Klimushin, E. V. Bugaev and I. A. Sokalski, *Parametrization of atmospheric muon angular flux underwater*, PhysRevD.64.014016

[Kno99] G. Knoll: *Radiation Detection and Measurement.* Third Edition. In Johon Wiley & Sons, Inc. (1999)

[Kra05] Ch. Kraus, B. Bornschein, L. Bornschein, J. Bonn, B. Flatt, A. Kovalik, B. Ostrick, E.W. Otten, J.P. Schall, Th. Thümmler, Ch. Weinheimer, *Final results from phase II of the Mainz neutrino mass search in tritium* β *decay* Eur. Phys. J. C **40** (2005) 447

[Kre99] J. Kremer et. al., *Measurements of Ground Level Muons at Two Geomagnetic Locations*, PHYSICAL REVIEW LETTERS, V83, N21 (1999) Page: 4241

[Lob85] V. M. Lobashev *et al.*, Nucl. Instr. Meth. **A240** (1985) 305

[Lob03] V. M.Lobaschev, *The search for the neutrino mass by direct method in the tritium beta-decay and perspectives of study it in the project KATRIN*,Nucl. Phys. A **719** C153-C160 (2003)

[Lor02] T. J. Loredo, D. Q. Lamb, *Bayesian analysis of neutrinos observed from supernova SN 1987A*, PHYSICAL REVIEW D, VOLUME 65, 063002, Feb. 02

[Maz08] M.N. Mazziotta, Nucl. Instr. Meth.. A584 (2008) 436

[Pau30] Wolfgang Pauli, *Offener Brief an die Gruppe der Radioaktiven bei der Gauvereins-Tagung zu Tübingen* (dated 4. Dez. 1930), reprinted in:
R. Kronig and V. Weisskopf (Eds.), Wolfgang Pauli, Collected Scientific Papers, Vol. 2, Interscience, New York (1964) 1316 - 1317

[Pi92a] A. Picard *et al.*, Nucl. Instr. Meth. **B63** (1992) 345

[Ras10] M. Rasulbaev, dissertation in preparation, Inst. f. Kernphysik, Universität Bonn (vorauss. 2010)

[Reimer] L. Reimer, *Scanning Electron Microscopy: Physics of Image Formation and Microanalysis*, Second Edition, Springer Verlag, ISBN 3-540-63976-4

[Rei59] R. Reines and C. L. Cowan, Phys. Rev. **113** (1959) 273

[Sch04] F. Schwamm, dissertation, *Untergrunduntersuchungen für das KATRIN-Experiment*, Fakultät für Physik der Universität Karlsruhe (TH), 2004

[Str09] S. Streubel, *Aufbau eines PET-Demonstrations-Experimentes und Anwendung von dessen FADC-basiertem Datenaufnahmesystem für Photoelektronenspektroskopie*, Institut für Kernphysik, Universität Münster, (2009)

[Tab71] T.Tabata, R.Ito and S.Okabe, NIM 94 (1971) 509

[Thü02] T. Thümmler, Diploma Thesis, Inst. f. Physik, Universität Mainz, 2002

[Val09] K. Valerius, dissertation: *Spectrometer-related background processes and their suppression in the KATRIN experiment*, Inst. f. Kernphysik, Universität Münster (vorauss. 2009)

[Vöc07] S. Vöcking, Diploma Thesis: *Implementierung der Multipole Boundary Element Methode für das KATRIN-Experiment*, Institut für Kernphysik, Universität Münster, (2008)

[Yao06] W.-M. Yao et al., *Cosmic Rays*, Journal of Physics G 33, 1 (2006) available on the PDG WWW pages
`http://pdg.lbl.gov/`

[Zac09] M. Zacher, *Electromagnetic design and field emission tests for the wire electrode of the KATRIN main spectrometer*, Institut für Kernphysik, Universität Münster, (2009)

[Zbo10] M. Zboril, dissertation in preparation, Inst. f. Kernphysik, Universität Münster (vorauss. 2010)

Acknowledgement

I would like to thank my advisor, Prof. Weinheimer, for giving me the chance to work in a great environment and supporting my work, as well as for his always taking the time to help, no matter how busy he was. I would also like to thank Dr. M. Beck and Dr. V. Hannen for their support of my work, and their valuable input. Additionally, my appreciation goes to the members of the Weinheimer AG for their assistance as well as for making working on the different projects very enjoyable.

This thesis would not have been possible without the help and support of the members of the Mainz crew: Dr. Marcus Beck, Kathrin Valerius, and Sebastian Streubel, or the support from the members of the AG Quantum of the Johannes Gutenberg University of Mainz, especially Dr. J. Bonn and Bea Ostrick, during the preparation and conduction of the measurements done in Mainz.

I would also like to thank our engineer H.W. Ortjohann who made the design and construction of the vacuum setup as well as the Mainz experiments possible, helping with many technical details, and when needed constructing portions himself. He did not just show me how to get things done, but also how to get things done properly. H. Baumeister also provided valuable assistance during the construction of the vacuum test stand. The IKP workshop fabricated parts of this experiment.

Of course none of this would have happened without my parents, who supported me throughout my time at university, as well as the support of my friends, especially Philipp and Radi who I attended many lectures with during my time in university.

Lastly, I thank my co-referee, Prof. Wessels, for many enjoyable volleyball matches, as well as for taking the time to referee this thesis.